Lukas Schafzahl, BSc

Characterization of Lithium- and Sodium Alkyl Carbonates as SEI Components for the Design of Novel Electrolytes

MASTER'S THESIS

to achieve the university degree of

Diplom-Ingenieur

Master's degree programme: Technical Chemistry

submitted to

Graz University of Technology

Supervisor

Univ.-Prof. Dr. rer. nat. Martin Wilkening
Institute for Chemistry and Technology of Materials

Dipl.-Ing. Dr. sc. ETH Stefan Freunberger
Institute for Chemistry and Technology of Materials

Graz, January 2015

Deutsche Fassung:

Beschluss der Curricula-Kommission für Bachelor-, Master- und Diplomstudien vom 10.11.2008

Genehmigung des Senates am 1.12.2008

EIDESSTATTLICHE ERKLÄRUNG

Ich erkläre an Eides statt, dass ich die vorliegende Arbeit selbstständig verfasst, andere als die angegebenen Quellen/Hilfsmittel nicht benutzt, und die den benutzten Quellen wörtlich und inhaltlich entnommene Stellen als solche kenntlich gemacht habe.

…… ……..

Datum Unterschrift

Englische Fassung:

AFFIDAVIT

I declare that I have authored this thesis independently, that I have not used other than the declared sources/resources, and that I have explicitly marked all material which has been quoted either literally or by content from the used sources.

…… ……..

Date Signature

Abstract

The superior energy storage of nonaqueous alkaline ion batteries stems to a good part from the increased cell voltage as compared to aqueous batteries. The used organic electrolytes exhibit a much wider window of electrochemical stability than aqueous ones. Yet this is not sufficient for all electrode materials. Particularly the now typically used graphite anode relies on the formation of a passivation layer, called the solid electrolyte interface (SEI), that forms during initial cycles as a result of electrolyte decomposition and prevents the electrolyte from continuous reaction. It needs to block electron transport whilst allowing passage of ions.

To increase the energy density beyond the state of the art important directions are high capacity anodes (relying on alloying or conversion reactions) and high voltage cathodes that both operate outside the stability window of any known electrolyte and require passivation to work. The composition and function of the SEI on graphite is only understood sketchy despite more than three decades of investigations. There is therefore no solid foundation to design passivation layers for the emerging electrode materials that impose even more severe challenges than graphite. These are amongst others large volume changes of the anode materials and highly oxidizing cathode potentials.

Lithium alkyl carbonates are lead compounds in the SEI on graphite, transition metal oxides, alloying and conversion electrodes. This work aims to identify possible new SEI compounds, derived from those identified in standard electrolytes, that show improvements in desired properties for these emerging electrode materials. These are (i) resilience towards surface strains to avoid cracking upon expansion/contraction of electrode materials (ii) improved Li+ conductivity, (iii) oxidation stability. To this end, a small library of short chained and „fictive“ long chained lithium alkyl carbonates and their sodium analogues was synthesized and investigated with respect to thermal stability, molecular arrangement and ionic conductivities.

Thermal decomposition proceeds at 150-300 °C yielding the inorganic alkali metal carbonate as the main product. The structure of alkyl dicarbonates is disordered, whereas short and long chained alkyl monocarbonates assume crystalline and bilayered lamellar phases, respectively. Lithium ion conductivity generally decreases from the first to the last. In contrast, sodium ion mobility is independent of molecular arrangement and structure in monoalkyl carbonates.

Moreover, electrolytes that decompose to such or similar alkyl carbonates were prepared and subjected to preliminary testing. Cathodic and anodic stabilities are comparable to an EC/DMC mixture. Dihexyl carbonate was identified as a potential additive for high voltage cathodes as it efficiently passivated a glassy carbon surface up to 5.2 V.

Kurzfassung

Die verbesserte Energiespeicherung in nichtwässrigen Alkalibatterien resultiert aus der höheren Zellspannung verglichen mit wässrigen Systemen. Die dabei verwendeten organischen Elektrolyten weisen ein deutlich größeres elektrochemisches Stabilitätsfenster auf, das jedoch nicht ausreicht, um thermodynamische Stabilität auf allen Elektrodenmaterialien zu garantieren. Speziell die häufig verwendeten Graphitelektroden erfordern die Bildung einer Passivierungsschicht, die solid electrolyte interface (SEI) genannt wird. Sie entsteht durch die Zersetzung des Elektrolyten in den ersten Zyklen und verhindert weitere Reaktionen, indem sie als ionischer Leiter aber elektrischer Isolator wirkt.

Wichtige Entwicklungen zur Erhöhung der Energiedichte sind Legierungs- und Konversionsanoden mit hoher Kapazität und Hochspannungskathoden. Beide arbeiten jedoch außerhalb des Stabilitätsfensters bekannter Elektrolyten und erfordern daher eine Passivschicht. Das Verständnis der Zusammensetzung und Funktionsweise der SEI auf Graphit ist aber auch nach drei Jahrzehnten der Forschung noch lückenhaft. Dadurch existiert keine solide Grundlage für die Entwicklung von Passivschichten für zukünftige Elektrodenmaterialien, die unter anderem durch Volumenänderungen von Anodematerialien oder stark oxidierenden Kathodenpotentialen noch höhere Anforderungen an den Elektrolyten stellen.

Lithium-Alkylcarbonate sind Hauptbestandteile der SEI auf Graphit-, Übergangsmetalloxid- und Legierungs- und Konversionselektroden. In dieser Arbeit wurde versucht, neue mögliche SEI Bestandteile zu identifizieren. Diese leiten sich von den Abbauprodukten in Standardelektrolyten ab und sollen gewünschte Eigenschaften wie (I) die Widerstandsfähigkeit gegen Spannungen in der Oberfläche und dem Aufbrechen durch Volumenänderungen, (II) Li^+ Leifähigkeit und (III) die Oxidationsstabilität verbessern. Dazu wurde eine kleine Bibliothek dieser kurzkettigen Lithium-Alkylcarbonate, sowie deren langkettige und Natrium haltige Analoga synthetisiert und hinsichtlich ihrer Temperaturstabilität, molekularen Anordnung und ionischen Leitfähigkeiten untersucht.

Die thermische Zersetzung dieser Moleküle zu anorganischen Carbonaten findet zwischen 150 und 300 °C statt. Alkyldicarbonate bilden ungeordnete Strukturen, während kurzkettige Alkylmonocarbonate kristalline- und langkettige Alkylmonocarbonate lamellare Doppelschichtstrukturen einnehmen. Die Lithium-Ionenleitfähigkeit sinkt von der ersten bis zur letzten dieser Anordnungen. Die Mobilität von Natrium-Ionen in Alkylmonocarbonaten ist hingegen unabhängig von deren Kettenlänge und Anordnung.

Außerdem wurden Elektrolyte hergestellt, deren Zersetzung solche oder ähnliche Alkylcarbonate ergibt. Laut ersten Tests ist deren kathodische und anodische Stabilität vergleichbar mit der einer EC/DMC-Mischung. Dihexylcarbonat passivierte eine Elektrode aus glasartigem Kohlenstoff bis zu einer Spannung von 5.2 V und stellt damit ein potentielles Additiv für Hochspannungskathoden dar.

Acknowledgement

First of all I want to thank Dr. Stefan Freunberger for his guidance during the last months. He always found time to answer a million questions and to encourage me when the results looked bleak. I also want to express my gratitude to Prof. Martin Wilkening for allowing me to write my thesis in his group.

I am very grateful to all my colleagues for creating a pleasant working atmosphere, introducing me to and helping me with the many devices that were new to me. Additionally, I want to thank Dr. Heike Ehmann and Dr. Manfred Kriechbaum for X-ray analysis and interpretation, Dr. Petra Kaschnitz for NMR-spectroscopy, Ing. Josephine Hobisch for thermal analysis, Dr. Yuhui Chen for performing IR-measurements on my samples, Dr. Yussef Hassoun for preparing the Sn/C electrode materials and Christina Albering and Birgit Ehmann for providing me with countless small things. I also want to acknowledge the support of Prof. Christian Slugovc and his group, who let me perform synthetic work in their lab. Without all of you my work would not have been possible.

Furthermore, I want to thank all my friends that made my studies a time I will gladly remember. Parties, dinners, hiking trips, board game, pen and paper and movie evenings provided the necessary distractions to my work. I also want to express my deep gratitude to my parents Gisela and Hans, who always supported me in the last 25 years. You have always had an open ear and encouraged me to pursue and achieve my goals.

My special thanks go to Christine, Max and Sandra, who always made me feel welcome and always had a sympathetic ear. Last, and most importantly, I want to thank Bettina who possesses the strange ability to make me smile no matter the circumstances. I cherish the time spent with you.

Table of content

1 INTRODUCTION 8

2 THEORETICAL PART 10

2.1 Electrodes 10
2.1.1 Negative electrode materials 10
2.1.2 Positive electrode materials 11

2.2 Electrolytes 12

2.3 Solid electrolyte interface 14
2.3.1 Formation 14
2.3.2 Structure 15
2.3.3 Li-ion conduction 15
2.3.4 Interfaces on positive electrodes 16

2.4 Novel approaches 16
2.4.1 High voltage cathodes 17
2.4.2 Alloying and conversion anodes 18

3 RESULTS AND DISCUSSION 20

3.1 Characterization of SEI components 20
3.1.1 Purity and contaminations 20
3.1.2 Thermal stability and decomposition 24
3.1.2.1 Thermal stability 24
3.1.2.2 Emitted ions 24
3.1.2.3 Decomposition products 25
3.1.3 Molecular Arrangement 28
3.1.4 Conductivities 33

3.2 Preliminary electrolyte testing 39
3.2.1 Electrochemical Stability 39
3.2.2 SEI formation 41
3.2.3 Galvanostatic cycling 44

4 CONCLUSION AND OUTLOOK 47

5 EXPERIMENTAL PART 48

5.1 Synthesis 48
5.1.1 Chemicals 48
5.1.2 Analytical methods 48
5.1.3 Synthesis of SEI components 49

5.1.3.1 General procedure for the synthesis of lithium and sodium alkyl carbonates 49
5.1.3.2 LS 3: 1,2-Butandiol 49
5.1.3.3 LS 7: 1,2-Hexanediol 50
5.1.3.4 LS 4: 1,2-Dodecanediol 50
5.1.3.5 Synthesis of lithium alkyl dicarbonates 51
5.1.3.6 Synthesis of sodium alkyl dicarbonates 51
5.1.4 Synthesis of electrolytes 52
5.1.4.1 Cyclic carbonates 52
5.1.4.2 Linear Carbonates 54

5.2 Characterization of SEI components 56
5.2.1 Differential Scanning Calorimetry/Thermogravimetry with Mass Spectrometry 56
5.2.2 Small Angle X-Ray Scattering 56
5.2.3 Powder X-Ray Diffraction 57
5.2.4 Electrochmical impedance spectroscopy 57

5.3 Preliminary electrolyte testing 58
5.3.1 Linear sweep- and cyclic voltammetry 58
5.3.2 Galvanostatic Cycling with Potential Limitation 58
5.3.2.1 Preparation of graphite electrodes 58
5.3.2.2 Preparation of Sn-C electrodes 58
5.3.2.3 Cell assembly and measurement 59

6 APPENDIX 60

6.1 Literature 60

6.2 List of Figures 66

6.3 List of Tables 68

6.4 Abbreviations 69

1 Introduction

In the last 25 years, Li-ion batteries have made an enormous progress from first commercialization to a mature technology that powers virtually all portable electronics. Further progress is spurred by the realization of hybrid and all-electrical vehicles offering a large driving range at reasonable speeds. More importantly, our societies are facing the challenges of climate change and limited fossil fuel resources that demand a transition to more sustainable energy sources. The intermittent nature of wind and solar power, however, requires advanced stationary energy storage systems, with Li-ion batteries being one option.

Li-ion batteries reversibly convert electrical energy to chemical energy by shuttling lithium ions from a transition metal positive electrode (cathode) to a graphite negative electrode (anode) and *vice versa*. In contrast to other battery technologies, however, the widely used, carbonate based electrolyte is thermodynamically unstable due to extremely low potentials at the anode. Fortunately, the decomposition products form a protective film, termed solid electrolyte interface (SEI) that prevents further reduction. Hence, a resilient SEI permeable to lithium ions but impeding electron transfer is vital for the long-term performance of a cell. Analysis of the SEI, however, is complicated by its thinness, sensitivity and dependence on cell history, resulting in differing or conflicting results regarding its composition. Thus, the relation between composition, structure and properties of the SEI is still not entirely understood. Nevertheless there has been considerable progress in the last years regarding the families of compounds occurring and their formation mechanism.[1]

On the other hand recent work was focusing on understanding the SEI's role in the cell impedance. It is yet under debate whether the contributions of the Li^+ desolvation energy or ion transport in the SEI layer are dominating.[2,3] While the former is a mostly determined by the electrolyte the latter is known to add substantially to cell impedance due to sluggish Li^+ transport in the SEI.[4] Despite its vital role in the cell there has hardly been work on fundamental understanding Li-ion transport in the SEI. Only very recently theoretical work shed some light on this by investigating a typical constituents, LEDC.[3,4]

The advent of new classes of high-capacity anodes based on alloying or conversion and high voltage cathodes brings about new challenges for passivation against continuous electrolyte decomposition. These include large volume changes at the anodes and highly oxidizing potentials at the cathodes. The common way to find electrolytes for those materials is to try out different classes of organic electrolytes, for example carbonate-, sulfonate- or ether-based electrolytes.

Here we want to go the reverse way and look whether we can, starting from the classes of SEI components known, design new possible SEI components with the desired properties. These are (i) resilience towards surface strains to avoid cracking upon expansion/contraction of electrode materials (ii) improved li-ion conductivity and (iii) oxidation stability. Once there is a handle on desirable SEI components in turn electrolytes shall be designed to yield the identified SEI components.

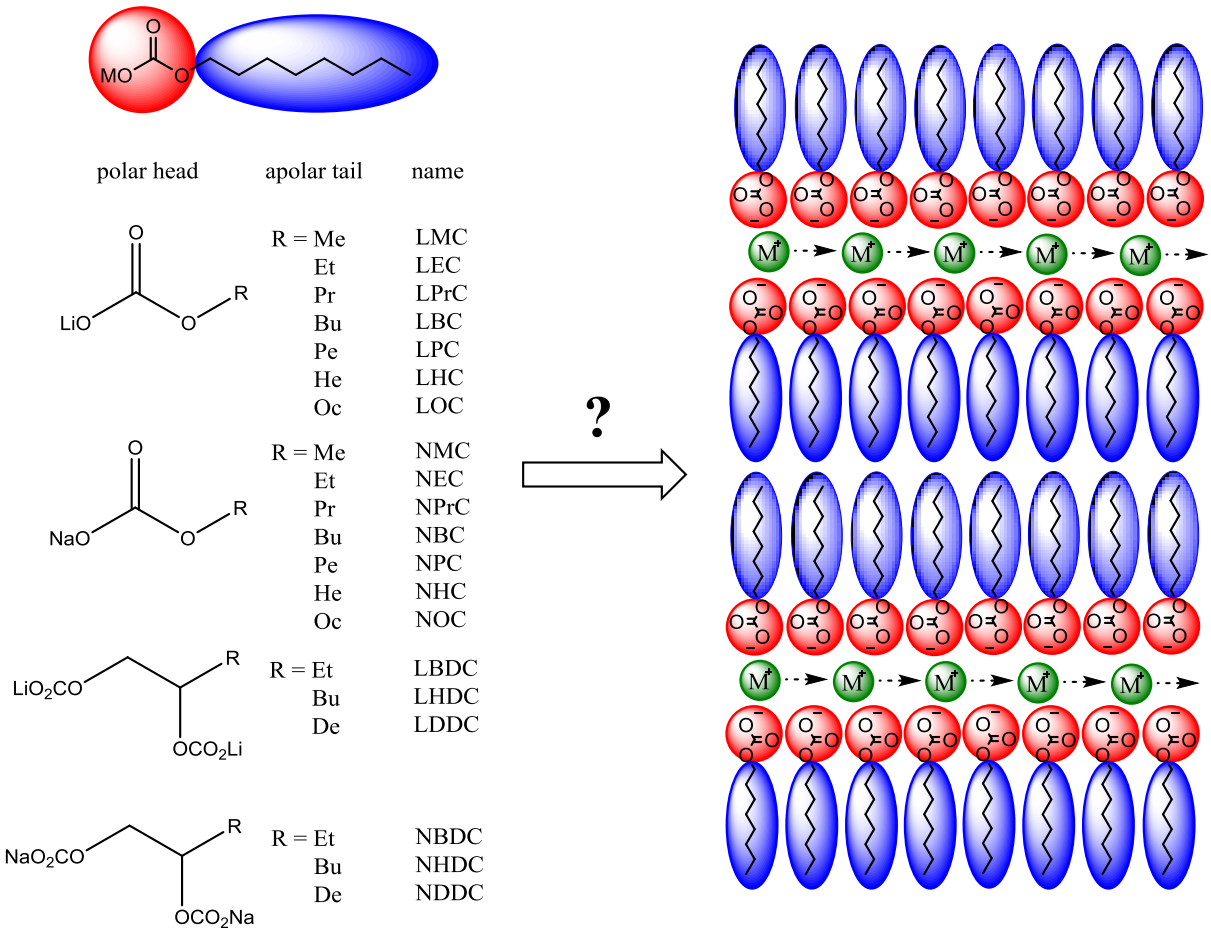

Fig. 1: Overview of the synthesized SEI components (left) that might form lamellar structures allowing 2D ionic diffusion.

A small library of carbonate based SEI components was synthesized and analyzed with respect to structure, thermal properties and ionic conductivity. The library included the lithium alkyl carbonates and dicarbonates that were found in the SEI on currently employed carbonaceous and transition metal electrodes as well as on novel alloying, conversion and high voltage electrodes. Additionally, the library contained “fictive” carbonates with longer alkyl chains and their sodium analogues (Fig. 2). Thus, we could not only differentiate the contributions of alkyl chain length and counter ion, but also determine whether the “fictive” long-chained carbonates had more favorable relevant properties.

In particular we hoped to show that amphiphilic long-chained carbonates crystallize in a layered structure, as was demonstrated by Kato for a copolymer with a resistive, apolar and a polar polyethylene glycol phase.[5] The polymer formed a layered structure, exhibiting high 2D lithium ion conductivities of 1.3 x 10^{-3} S/cm at 35 °C. Surprisingly, the conductivity even surpassed a polymer containing polyethylene glycol exclusively. Thus, layered structures can improve lithium ion mobility and ultimately reduce interfacial resistance.

Furthermore, electrolytes yielding such or similar SEI components upon breakdown were synthesized and subjected to preliminary studies concerning their oxidative and reductive stability and cycling behavior in graphite and Sn-C composite half-cells.

2 Theoretical Part

Since their commercialization in the early nineties, lithium ion batteries have conquered the market for portable electronics, owing to their fortuitous combination of long shelf and cycle life, high specific energy (~150 Wh/kg) and energy density (~400 Wh/L).[6] Moreover, coulombic and energy efficiencies are rather high, amounting to 99.9 and 95-98 %, respectively. These ubiquitous features were achieved by carefully matching the functional components of a cell, the positive and negative electrode and the electrolyte, which are described in the following sections.

2.1 Electrodes

State of the art Li-ion batteries comprise two hosts that are able to reversibly accommodate lithium ions. The negative electrode, conventionally referred to as anode, typically consists of graphitic carbon. During charge, lithium ions are intercalated in between the graphene layers while electrons are inserted into the electronically conductive graphitic matrix to preserve electroneutrality. When the cell is discharged, the ions are removed from the anode (de-intercalation) and the anode is re-oxidized (eq. 1).

$$x\mathrm{Li}^+ + x\mathrm{e}^- + x\mathrm{C}_6 \underset{\text{discharge}}{\overset{\text{charge}}{\rightleftharpoons}} x\mathrm{LiC}_6 \qquad (1)$$

The lithium ions are then shuttled to the positive electrode, or cathode, and intercalated into a transition metal oxide (eq. 2).

$$\mathrm{LiMO}_2 \underset{\text{discharge}}{\overset{\text{charge}}{\rightleftharpoons}} \mathrm{Li}_{1-x}\mathrm{MO}_2 + x\mathrm{Li}^+ + x\mathrm{e}^- \qquad (2)$$

Thus, the combined cell reaction is

$$x\mathrm{C}_6 + \mathrm{LiMO}_2 \underset{\text{discharge}}{\overset{\text{charge}}{\rightleftharpoons}} x\mathrm{LiC}_6 + \mathrm{Li}_{1-x}\mathrm{MO}_2 \qquad (3)$$

Note that during the whole cycle, lithium remains in the oxidation state +1 precluding dangerous lithium plating. Redox reactions occur exclusively in the host material while the ions act as charge carrier between the electrodes, coining the term “rocking chair battery”.

2.1.1 Negative electrode materials

Before the advent of lithium-ion or rocking chair batteries, intensive research was invested in rechargeable batteries with a metallic lithium anode. The interest was sparked by the fact that lithium metal combines the lowest density of all metals (0.534 g/cm^3) with the most negative standard potential (-3.0 V versus standard hydrogen electrode). The latter results in the maximum cell potential combined with any given cathode, while the former promises extremely high specific capacities of 3860 mAh/g.[7] Furthermore, it was shown that lithium was stable in certain organic electrolytes, which was attributed to the formation of a protective layer. As this layer consisted of insoluble reduction products of the electrolyte, it was called SEI.

Reversible lithium metal cells, however, exhibited several serious issues. Upon continued cycling, the SEI is periodically broken and reformed, eventually consuming metal and electrolyte.[8] Furthermore, even during moderately fast charge, needlelike lithium crystals grow on the cathode. These dendrites

pose a serious safety hazard as they are prone to pierce the separator and short circuit the cell with catastrophic consequences.[6] Thus, safety concerns and poor cycle life prevented successful commercialization of lithium metal batteries and paved the way for carbonaceous intercalation anodes.

In such anodes, both natural and synthetic graphite is frequently employed, with the graphene layers stacked in ABABAB (hexagonal) and ABCABC (rhombohedral) order with a spacing of 3.35 Å. Naturally, these materials are not entirely free of defects, however graphitic aggregates are extensive. In contrast, soft and hard carbon is increasingly disordered, with the graphene stacks rotated instead of parallel (turbostatic disorder).[6] The lower degree of order in these materials is reflected by a larger interlayer distance.

Intercalation into graphitic materials occurs at voltages < 0.2 V vs. Li/Li^+ (unless stated otherwise, all voltages given refer to Li/Li^+), when lithium ions migrate through the prismatic surfaces of graphite.[9] The attractive Van-der-Waals forces between two graphene layers thereby prevail over coulombic repulsion between lithium ions. Thus, alternating filled and empty layers are preferred to a random ion distribution. In fact, several voltage plateaus are observed during charge of a graphitic anode. These "stages" each correspond to a combination of x empty layers between two full ones, with x gradually decreasing from 4 to 0.

Fully charged graphite anodes theoretically contain 1 lithium ion per 6 carbon atoms, located centrally between two graphene hexagons. The theoretical capacity of lithiated graphite is 372 mAh/g with practical values around 300 mAh/g,[10] as compared to 3860 mAh/g for lithium metal. However, interlayer distances expand by only 10.3 % upon charge, enabling reversible cycling at high capacity retention.[11] Additionally, the low voltage of lithiated graphite allows for comparably high cell voltages and high energy densities.

In comparison, hard carbon materials offer additional lithium storage sites, resulting in superior specific capacities of over 1000 mAh/g. Unfortunately, hard carbon materials suffer from higher voltage (~1.0 V) and a voltage hysteresis. Discharge proceeds at higher voltages, thus the energy gained from discharge is smaller than the energy spent during charge. This energy inefficiency limits broad application of hard carbon materials.

2.1.2 Positive electrode materials

The most common positive electrode materials comprise a transition metal and can be distinguished by their structure, which is layered, spinel or olivine.

The layered oxide $LiCoO_2$ (LCO) was embodied in the first Li-ion cells commercialized by Sony in 1991 and has remained extensively used ever since. LCO forms a rock salt lattice, the cobalt- and lithium atoms coordinated octahedrally by oxygen (Fig. 2a).[12] Lithium diffusion in the 2-dimensional layers is fast, complementing the metallic electron conductivity of 10^{-3} S/cm.[13] Thus, favorable electrochemical properties add to the high operating voltage of the Co^{+3}/Co^{+4} ion pair (4.0 V) that is reduced upon lithium intercalation. The theoretical specific capacity of LCO is 274 mAh/g.[14] Unfortunately, $Li_{1-x}CoO_2$ is structurally and chemically instable at $x > 0.5$, leading to layer slippage to form an inactive phase and a slow loss of oxygen and cobalt at deep charge.[15] Despite the available specific capacity being thus limited to 140-150 mAh/g, LCO displays an energy density rarely achieved by other commercial cathode materials and is predominantly employed when energy density and volume are critical. However, oxygen formed during abuse conditions can accumulate and eventually cause thermal run-

away and electrolyte inflammation.[16] Additionally, cobalt constitutes only 30 ppm of the earth's crust and thus is expensive.

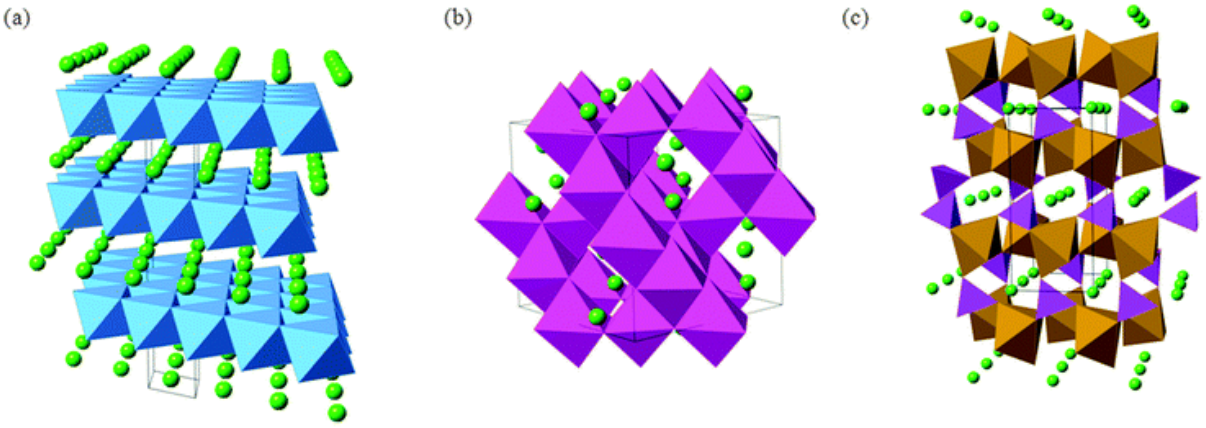

Fig. 2: Main structural classes of positive electrode materials: (a) Layered oxide structure of $LiMO_2$ (M=Co, Ni, Mn), (b) cubic $LiMn_2O_4$ spinel and (c) olivine $LiMPO_4$ (M=Fe, Co, Ni). Lithium ions are shown in green, octahedral CoO_6 in blue, MnO_6 in purple, FeO polyhedral in brown and PO_4 tetrahedra in lavender. Figure taken from ref. [17].

Consequently, economical and security reasons led to the development of alternative layered oxides based on the more inexpensive materials nickel and manganese. Among many examples, the ternary material $LiNi_{0.33}Mn_{0.33}Co_{0.33}O_2$ (NMC) is one of the most successful. Albeit NMC inherits the structural instability upon deep discharge, the specific capacity is slightly higher and introduction of manganese stabilizes the structure resulting in improved cycle stability.[14]

$LiMn_2O_4$ (LMO) was introduced as an inexpensive and environmentally benign alternative to LCO. It crystallizes in a spinel structure, with the manganese ions occupying the octahedral sites formed by oxygen (Fig. 2b). In practice, the working potential is around 4.1 V, partially compensating the specific capacity of 120 mAh/g. Unfortunately, the initial capacity fades quickly which was attributed to several factors including Jahn-Teller-distortion of Mn^{+3}, loss of crystallinity and instability towards acids,[18] the latter being considered the most severe. In an electrolyte containing $LiPF_6$, HF is formed from traces of moisture and leeches Mn^{2+} ions from the cathode.[19] However, dopants such as excess lithium and aluminum or surface coatings alleviate these detrimental effects and significantly improve the performance of LMO.[20]

The third class of cathode materials crystallizes in olivine structure. In its most prominent example, $LiFePO_4$ (LFP), the oxygen atoms form an almost perfect hexagonal dense packing. Phosphorus atoms occupy the tetrahedral and iron and lithium the octahedral sites, respectively, allowing 1-dimensional lithium diffusion.[21] Initially, low lithium and electron conductivity were major drawbacks of LFP, limiting reversible capacities to <100 mAh/g. However, nanosized particles, shortened lithium diffusion lengths and various conductive coatings improved electronic conductivity and allowed specific capacities of 165 mAh/g.[22] Due to the low operating potential of 3.5 V the energy density is still inferior to LCO, but excellent capacity retention, inherent safety and low cost suggest the employment of LFP when energy density is secondary. Despite its initial problem of low conductivity, nanosizing and conductive coatings made LFP now material of choice for high power applications.

2.2 Electrolytes

Electrolytes in Li-ion batteries strive to simultaneously satisfy several criteria. First, the electrolyte must display thermodynamic or at least kinetic stability towards other cell components, in particular

the electrodes. The former is described by the energy gap between the lowest unoccupied molecular orbital (LUMO) and the highest occupied molecular orbital (HOMO). Only if the redox potentials of cathode and anode are within this band gap, also referred to as “stability window”, electrolyte decomposition is prevented (Fig. 3).

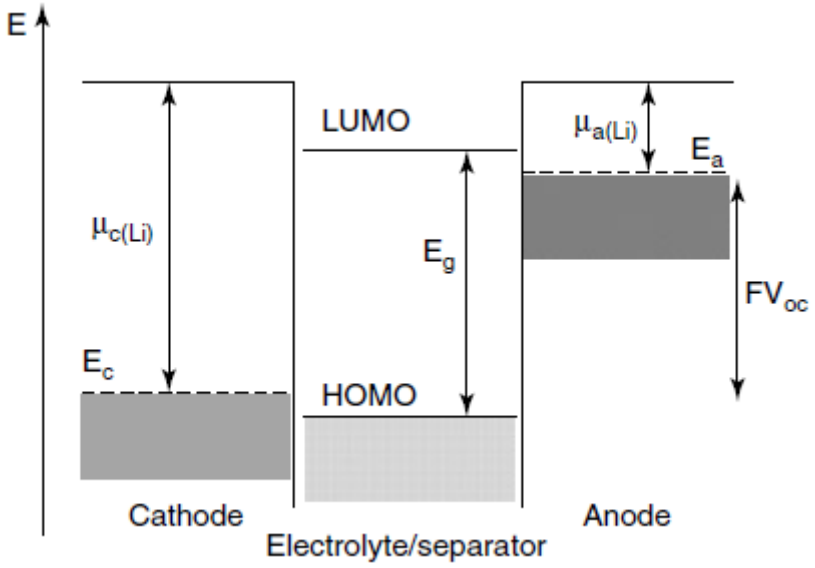

Fig. 3: Schematic energy diagram of a lithium ion battery at open circuit. Redox potentials of anode (E_a) and cathode (E_c) are within the stability window of the electrolyte (E_g).

Obviously, the large operating potentials of in Li-ion batteries preclude the employment of aqueous electrolytes. Instead, cyclic and linear organic carbonates such as ethylene carbonate (EC), diethyl carbonate (DEC), dimethyl carbonate (DMC) and ethyl methyl carbonate (EMC) compose the electrolyte skeleton. Those carbonates have an E_{HOMO} of 4.3 eV, thus providing sufficient oxidative stability for the above mentioned 4V-class materials.[23] Conversely, E_{LUMO} is only 1.0 eV compared to ~0.2 eV of lithiated carbon; hence the electrolytes are reduced on the negative electron surface. The SEI formed in this process largely prevents further decomposition and therefore ensures kinetic stability.

Second, high ion conductivity is crucial and therefore a lithium salt, predominantly $LiPF_6$, is added to the electrolyte. The solvent thus requires a high dielectric constant to dissolve the salt. Moreover, low viscosity is desired to facilitate ion transport. Unfortunately, both prerequisites for high conductivity are contradictory, with one achieved at the expense of the other. As a compromise, binary or ternary mixtures of cyclic carbonates such as EC or PC (with a high dielectric constant but also high viscosity) and acyclic carbonates (DMC, DEC, EMC with low viscosity) provide conductivities of 5-10 mS/cm.[7]

Third, the transference number of lithium cations should be high as the anions do not contribute to the cell performance, but instead introduce concentration polarization due to anion enrichment at the respective electrode at high currents. Normally, the Li-ion transference number ranges between 0.2 and 0.4[7 and cited therein] depending on temperature, concentration and measurement method,[24] with a value of ~0.35 suggested for $LiPF_6$.[6] The inferior mobility of the smaller cations is attributed to the strong solvent-cation interactions as opposed to relatively weak solvation of the anions in the nonaqueous solvents. Thus, the lithium ion is coordinated by 4-6 solvent molecules.[25,26] Evidently,

coordination proceeds via the carbonyl oxygen[27] of preferentially cyclic carbonates with high donicity.[28]

Additional requirements comprise a wide liquid range, safety, low cost, low toxicity and the ability to form a stable SEI. Due to this multitude of prerequisites, novel approaches frequently improve one property while failing to meet others. Therefore the bulk composition of electrolytes has changed little in the last decade, despite extensive research dedicated to novel solvents and salts.

2.3 Solid electrolyte interface

Extreme potentials in Li-ion batteries induce sacrificial decomposition of the electrolytes, mainly at the carbonaceous negative electrodes. A film of insoluble reaction products is formed that ideally enables fast lithium ion conduction while inhibiting electron transfer and thus further electrolyte degradation. A stable SEI is of utmost importance to key parameters of the Li-ion battery such as cycle life, self-discharge rate, faradaic efficiency, safety and the irreversible capacity loss during the first cycle.

Despite its significance and close attention being paid by numerous researchers, the SEI remains what Winter calls “the most important and least understood component” of Li-ion batteries.[29] The reason for this is the elusive and sensitive nature of the SEI, whose structure and composition not only depends on solvents, conductive salts, electrolyte additives and electrode materials, but also the cell history and cycling conditions. Moreover, the SEI is extremely thin and sensitive to moisture and air. Thus the results obtained from SEI analysis have often been unclear or even contradictory. Nevertheless, steady advances in our understanding of the SEI are made by employing new in-situ analysis methods, computer simulations or characterization of SEI components.

2.3.1 Formation

SEI formation on the anode during the first cycle is described by the Besenhard-Winter model.[30] At potentials below 1.0 V, solvated lithium ions start to intercalate into the graphene layers that expand to 15.9 Å to accommodate the additional solvent molecules.[31] In presence of hydroxyl, carbonyl and carboxylate groups, the solvent molecules are reduced upon decreasing potential, as indicated by the contraction of graphene layers to a slightly increased spacing of 3.5 Å. Interestingly, in absence of functional groups on the graphite surface (or with “too stable” electrolytes), cointercalation continues resulting in exfoliation of graphite and eventually disintegration of the anode.[32]

Importantly, degradation reactions consume lithium ions and electrons. Hence, an irreversible capacity loss is introduced and increases the total weight of the battery, as the cathode as lithium source must compensate for lithium losses. After the first cycle, faradaic efficiencies approach 100% as SEI growth steadily declines. However, kinetic stability provided by the SEI is imperfect, thus parasitic currents never completely stop.[33]

This formation mechanism also highlights the importance of the lithium solvation sheath. Molecules that preferentially and too strongly solvate Li^+ will likely cointercalate and thus be embodied in the SEI and the graphite. Xu et al. observed this effect for electrolyte mixtures of EC and propylene carbonate (PC), where the latter is known for promoting graphite exfoliation even as a minor component. E.g., at 20 %mol PC constitutes 50% of the lithium ion solvation sheath, thus explaining the large influence of PC at low concentrations.[34]

2.3.2 Structure

Generally, the SEI on the graphitic negative electrode is described as a roughly layered structure, similar to the concept Aurbach developed for the SEI on lithium metal.[35] The inner part is believed to consist of mainly inorganic components, while organic molecules and polymers dominate the porous, electrolyte soaked outer layer.

Alkyl carbonates and dicarbonates (also called semicarbonates) are one of the most abundant species in the SEI, originating from solvent decomposition of linear and cyclic electrolytes, respectively, as well as decomposition products of the salt anion.[7] The proposed single-electron pathway for the reduction is depicted in eq. 4 and 5.

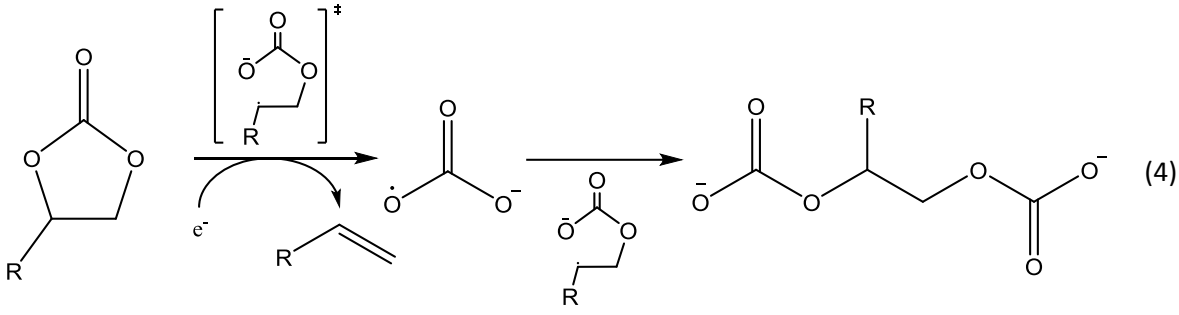

(4)

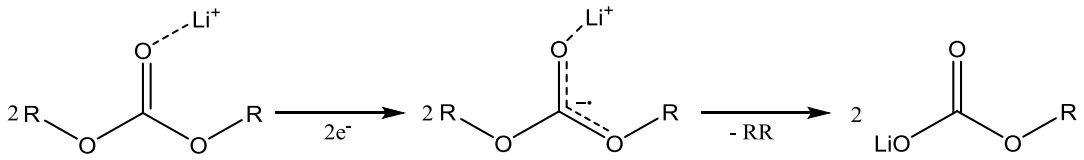

(5)

Further components include alkoxides, succinates, oxalates and oligomers with ethylene oxide repeating units or polycarbonates.[36,37] The formation mechanism of the latter was elucidated by Gachot et al. who concluded that both linear and cyclic electrolytes must be present to allow for formation of oligomers.[1] Oligomers were also proposed to be efficient in forming a stable SEI, which is also reflected by the success of vinylene carbonate (VC), a widely used additive that forms polymeric networks and increases SEI stability.[38]

Inorganic decomposition products from electrolytes or salts, such as LiF and various fluorophosphates and phosphates[39] constitute the inorganic part of the SEI. The presence of Li_2CO_3 is controversial and it was suggested that it appeared only in aged cells[37], in combination with certain salts[40] or after reaction with atmospheric CO_2.[41] This debate further demonstrates the challenges that researchers are facing in SEI analysis.

2.3.3 Li-ion conduction

Despite its importance, Li-ion conduction through the SEI layer is not well understood. Lu and Harris monitored the ion exchange of a SEI layer grown from ^7Li with an electrolyte containing $^6LiBF_4$. They concluded that while diffusion of the solvent into pores is responsible for ^6Li up to a depth of 5 nm, further exchange is driven by ion exchange and the associated entropy of mixing.[42] It was proposed that lithium containing moieties function like an ion-exchanger, similar to the Grotthus-mechanism for proton and hydroxide ion conduction.

These findings, however, also established that solvent diffusion is limited to the outer part of the SEI. Consequently, Li-ion desolvation occurs within the SEI, accounting for an additional energy barrier

and thus resistance. Hitherto, the estimated total energy barrier of a Li-ion moving through the SEI (50-100 kJ/mol) and the corresponding impedance was generally attributed to “charge transfer”. Following studies focused on discriminating the influence of Li-ion desolvation and ion migration. The results demonstrate that the energy barrier for the former is ~50 kJ/mol and thus – at least under ideal circumstances – contributes more to the overall resistance than the ion transport through the interface.[7]

Computer simulations provide additional information on diffusion mechanisms. Harris et al. modeled Li-ion diffusion in crystalline Li_2CO_3, concluding that movement proceeds via a series of transition states. The coordination by 4 to 5 oxygen atoms strongly diminished the activation energy compared to a direct longitudinal diffusion.[43] The Li-ion conductivity in lithium ethylene dicarbonate (LEDC) was computed by Borodin et al. to be between 10^{-8} to 10^{-10} S/cm, which is in excellent agreement with the experimental value (10^{-9} S/cm). They found somewhat improved conductivity in ordered versus amorphous material. Again, Li-ions are coordinated by approximately 4 oxygen atoms, resulting in an activation energy of 64-84 kJ/mol for lithium ion conduction. This value is similar to lithium dissolution on an electrolyte/LEDC-interface, but differs from experimental results obtained by impedance spectroscopy (~20 kJ/mol).[4] Later they extended the simulation to both LEDC and lithium butyl dicarbonate (LBDC) in contact with electrolyte and could confirm a dependence of Li-ion desolvation rate and conductivity on structure. However, they argue that Li-ion transport in the SEI does contribute significantly to overall impedance.[3]

2.3.4 Interfaces on positive electrodes

In contrast to the SEI on the negative electrode, the effort devoted to interfaces on the positive electrode has been limited.[44] As the operating potential of now used commercial cathode materials is within the stability window of carbonate electrolytes, electrolyte stability can be maintained even without an SEI. Thus, the issue of interfaces on the cathode was considered less pressing. However, while the SEI on the cathode is initially thinner than on the anode, coverage is incomplete resulting in continuous deposition of material.[45] Eventually, cathodic SEI resistance exceeds other resistances and renders the cathodic interface the kinetic bottleneck of the cell.

Film formation on the cathode starts during synthesis and storage of the electrode material and proceeds when the surface is wetted with electrolyte. Spontaneous reactions occur, forming products such as LiF, PO_xF_y and Li_2CO_3, but also organic components such as alkoxides and alkyl (di)carbonates.[46,47,48] Furthermore, the presence of polymers formed from electrolytes with mixed carbonate and ether based repeating units was proposed.[49,50]

2.4 Novel approaches

During the last 25 years, the Li-ion technology has significantly evolved and maturated. Unprecedented energy density and satisfying reliability enabled broad commercial application in the portable electronics market. However, certain inherent limitations remained and prevent the advancement of Li-ion batteries into new areas.

Whereas cycle life is sufficient for electronics that demand hundreds of cycles, applications in stationary systems and electric vehicles require high capacity retention over thousands of cycles. Moreover, cathodes often rely on expensive and rare elements such as cobalt. Finally, the intercalation materials confine the achievable energy density.[51] Therefore, there is intense interest in developing

new materials and technologies that offer new chances, but also face new challenges, as will be highlighted in the next sections.

2.4.1 High voltage cathodes

Presently the overall energy density is limited by the cathode. As compared to the typical anode capacity of > 300 mAh/g, the typical cathode materials show up to around 170 mAh/g and chances seem slim to reach beyond 300 mAh/g which is targeted with multi electron materials.[52] One approach to improved specific energy is to increase the operating potential of the battery. As a carbonaceous negative electrode is already very close to the minimum potential set by metallic lithium, researchers invariably focused on positive electrodes. Amongst new cathode materials developed, promising candidates include predominantly variations of the aforementioned layered oxide, spinel and olivine structured cathode materials.[53]

$LiMn_{1.5}Ni_{0.5}O_4$ (LMNO) crystallizes in spinel structure and features a specific capacity of 135 mAh/g at 4.7 V.[54] Full cells with $Li_4Ti_5O_{12}$ were reported to achieve an energy density of 372 Wh/kg, which exceeds commercial Li-ion batteries.[55] Furthermore, LMNO showed excellent electrochemical performance, especially when doped with metals such as ruthenium or chromium.[56] In the layered-oxide derivative $xLi_2MnO_3 \cdot (1-x)LiMeO_2$, excessive lithium ions partially replace the transition metal. The additional lithium entails outstanding discharge capacities of 314 mAh/g.[57] Although the average potential is 3.5 V, high capacities are only obtained by charging above 4.5 V. Unfortunately, structural instability of the material results in low coulombic efficiencies and capacity deterioration, adding to poor electronic and ionic conductivities.[53] In a previous section, LFP was described as a benign and reliable cathode material, albeit operating at a potential of only 3.5 V. Replacing the iron with Mn, Co or Ni would, however, increase this value to 4.1, 4.8 and 5.2 V, respectively. $LiCoPO_4$ (LCP) has sparked particular interest due to its high energy density of 800 Wh/kg.[58] As LFP, LCP is plagued with unsatisfactory electronic and Li-ion conductivity, which was somewhat alleviated by iron doping.[59]

A universal approach to increase ionic transport is to employ nanoparticles for reduced diffusion path length. Unfortunately, electrolyte stability only extends to a potential of 4.5 V which is easily surpassed in high voltage cathodes.[7] As no protective SEI forms in standard electrolytes on the positive electrode, oxidation ensues and is greatly accelerated by the huge surface area of nanoparticles. Diverse coatings, for example carbon,[60] aluminum oxide[61] or from acidic fluorinated solutions[62] are able to mitigate these issues to variable degree. However, irreversible capacity losses and poor cycle life severely hamper commercial realization of high voltage cathodes.

A more basic solution would be an electrolyte or additive with improved oxidative stability to sustain reversible cycling. In terms of additives a range of molecules has been investigated including anhydrides, sulfones, lactones.[63,64,65,66,67] Moreover, other salts than $LiPF_6$ such as perfluoroalkylphosphates (e.g. lithium tris(pentafluoroethyl)trifluorophosphate (LiFAP)) have been proposed for high voltage electrolytes.[68] Room temperature ionic liquids mixed with organic electrolytes[69] and sulfones combined with various additives[70] have been investigated to that purpose, but suffer from low rate performance. A novel class of compounds, perfluorinated cyclic alkyl carbonates, was recently proven to enhance cycling stability remarkably at loadings of only 0.5 %. The authors concluded that the hydrophilic carbonate moiety is decomposed on the cathode surface, while the hydrophobic tail of the molecule acts as a barrier for further electrolyte decomposition.[71] Amphiphilic molecules thus offer exciting possibilities as additives for high voltage cathodes.

2.4.2 Alloying and conversion anodes

Extensive interest has also been dedicated to the development of new anode materials that offer higher specific capacities.

Amongst the elements forming alloys with lithium, silicon and tin are the most auspicious due to high theoretical specific capacities and favorable environmental and economic features. Alloying in silicon and tin proceeds via complex multistep reaction pathways that are dependent on voltage limits, temperature and morphology. The fully lithiated phases, $Li_{15}Si_4$[72] and $Li_{17}Sn_4$,[73,74] accommodate multiple lithium atoms per host atom. Hence, impressive specific capacities of 3579[72] and 993 mAh/g for silicon and tin alloys, respectively, could be achieved, compared to only 372 mAh/g for graphite.

Unfortunately, gravimetric specific capacities of delithiated phases are not meaningful for estimating improvements in a practical cell. First, alloying materials expand by more than 200 % upon lithiation which has to be considered in cell construction. Therefore the volumetric capacity with respect to the lithiated phase would be much more significant. Second, nanostructured materials are frequently employed to cushion the volume expansion, thereby introducing porosity to the material which further reduces volumetric capacity. Third, alloying materials operate at higher potentials (0.4 V for Si, 0.5V for Sn[75]) and thus decrease the energy density of the cell. In consequence, enhancements in energy density are limited to still noticeable ~40 % for practical cells, while current alloys offer quite modest 15-20 % improvement.[75]

Conversion materials reversibly react with lithium to form metal particles embedded lithium salt, as described by the following equation (eq. 6)

$$M_aX_b + (b \cdot n)\,Li \rightleftharpoons aM + bLi_nX \qquad (6)$$

where M is a metal such as Cr, Cu, Co or Mg, X an anion such as O, N, F, S, P, H and *n* the formal oxidation state of X. Interestingly, lithiation occurs at significantly lower potentials than predicted by thermodynamic calculations,[76] which might be attributed to the surface energy on the interface between metal and lithium salt.[77] De-conversion proceeds at higher potentials than conversion, as depicted in Fig. 4. The resulting voltage hysteresis could originate from fundamentally different reaction paths for both processes, as density functional theory (DFT) calculations suggest for FeF_3.[78] Furthermore, low electronegativity of the anion seems to correlate with a small hysteresis.[79] Considering the demand for high energy efficiency in a lithium-ion battery, this inefficiency poses a major obstacle to commercial conversion cells.

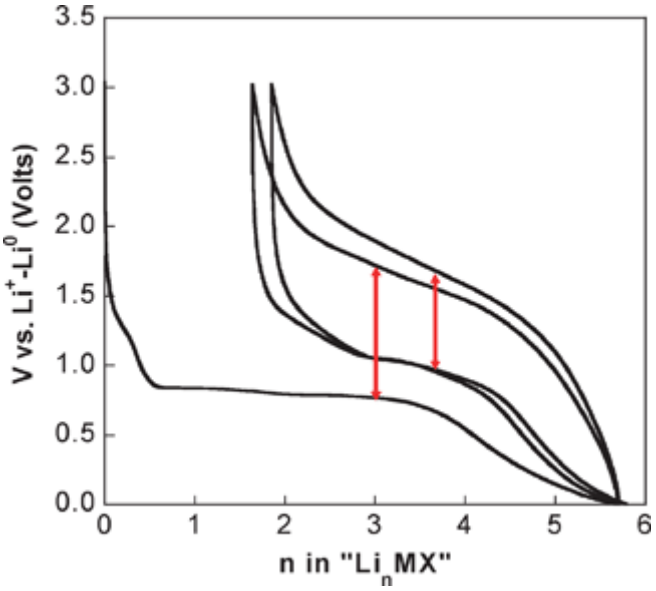

Fig. 4: The typical voltage hysteresis of a conversion material, depicted in a voltage vs. composition diagram. Figure taken from Palacín et al.. [80]

Furthermore, as alloying materials, conversion electrodes undergo serious structural reorganization during cycling, reflected by large volume changes. Particles can fracture and lose electric contact, eventually leading to capacity fading. The strategies to overcome this issue are similar in both cases. Heat treatments and optimization of the binder were shown to delay capacity deterioration, as were the incorporation of alloying or conversion material into a carbon matrix.[77 and cited therein,81] Nanostructured particles are another successful approach to suppress particle pulverization but, as for all nanostructured electrodes, increase the requirements placed on the electrolyte to form a protective SEI.

In carbonate-based electrolytes, identified components were similar to the SEI on carbon, including alkyl carbonates.[82,83,84] Due to the large volume changes, the film is frequently broken and reformed, decreasing reversible capacity. Addition of VC and especially fluorethylene carbonate (FEC) enhanced cycling stability.[85] Nevertheless, further improvements in electrode design, binder development and electrolyte formulation are needed to enable broad commercial application of alloying and conversion materials.

3 Results and discussion

3.1 Characterization of SEI components

3.1.1 Purity and contaminations

Infrared spectra were recorded by Dr. Yuhui Chen under inert atmosphere to confirm the identity of the moisture sensitive SEI components. Any exposure to air during the synthesis or the subsequent washing and drying steps would lead to a reaction of water with the respective organic alkali metal carbonate to form the corresponding alcohol, CO_2 and inorganic Li_2CO_3 or Na_2CO_3. After the washing and drying steps, the latter ones should be the only remaining decomposition products. Thus, the absence of Li_2CO_3 or Na_2CO_3 and the presence of characteristic peaks in a Fourier transform infrared spectroscopy (FTIR) spectrum prove a successful synthesis of the desired SEI components.

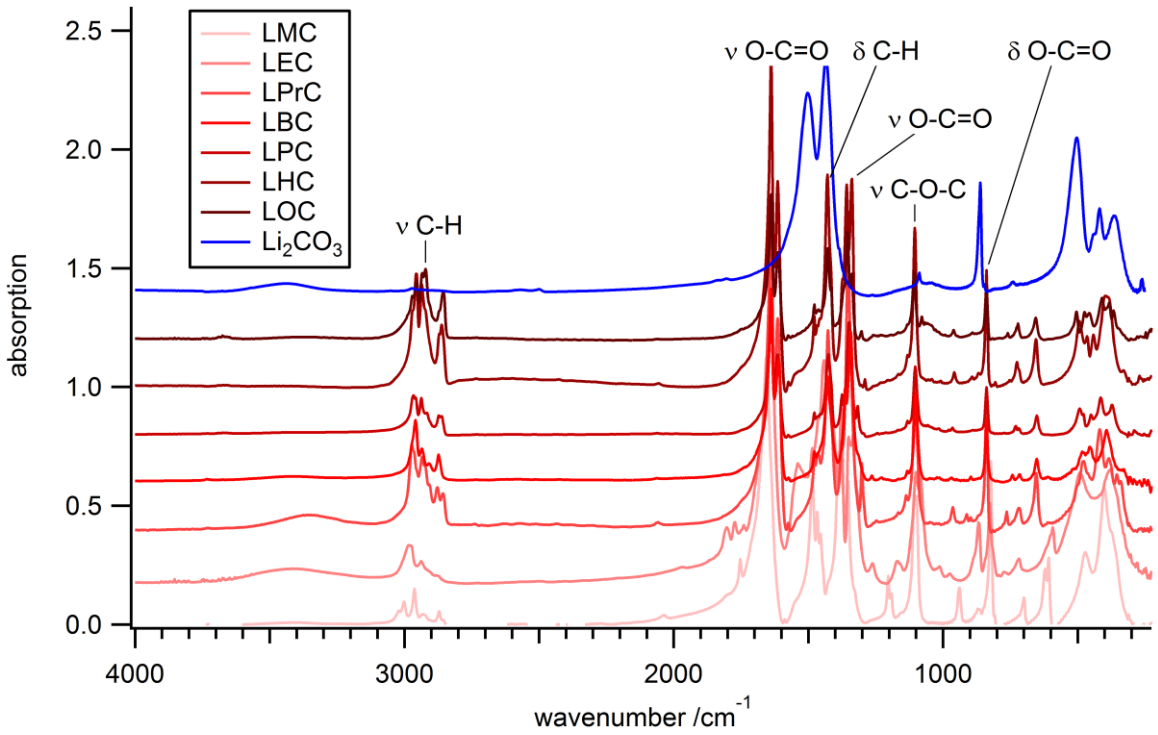

Fig. 5: FTIR spectra of all lithium carbonates from LMC (bottom) to LOC (top). Li_2CO_3 is depicted as reference (blue line). The offset between the baselines is 0.2.

In Fig. 5, the spectra of all lithium alkyl monocarbonates are compared to Li_2CO_3, which displays distinctive peaks at 1495, 1432, 862 and 503 cm^{-1} (see Table 1 for a summary of all vibrations). Unfortunately, the latter three coincide with similar peaks in the organic carbonates rendering a distinction dubious. The peak at 1495 cm^{-1}, however, is not present in the organic carbonates excluding LEC. Additionally, LEC exclusively exhibits a double peak at around 850 cm^{-1} mimicking both organic and inorganic carbonates.

This points to the difficulties during the synthesis of this particular carbonate LEC. All other compounds formed a precipitate immediately after a CO_2 atmosphere was established in the reaction vessel. The lithium ethoxide solution, however, did not cloud at all in three of four experiments. In the fourth attempt, finally a slight precipitate was obtained yielding merely 11 % product. Interest-

ingly, the educts ethanol, CO_2 and lithium metal were successfully employed in the synthesis of NEC, excluding a possible contamination. Additionally, steric or electronic hindrances are unlikely as the reaction proceeded smoothly for both LMC and LPrC. Thus, the reason for the complications in the synthesis of LEC remains unresolved.

Fortunately, solely LEC is contaminated with Li_2CO_3. Other lithium carbonates display peaks predominantly at the same wavenumbers. The peaks at 1080-1130 and 1410-1450 cm^{-1} correspond to the C-O stretching and the C-H rocking vibrations, respectively. Another strong absorption band is observed at 1610-1660 cm^{-1} and characteristic for carbonyl groups (ν O-C=O), whereas the medium band at 2860-3000 cm^{-1} originates from C-H stretching vibrations. All of the aforementioned peaks are absent in the inorganic Li_2CO_3 which features only three equivalent, mesomeric C-O bonds.

The spectra of the lithium alkyl dicarbonates (Fig. 6) generally resemble the ones discussed previously and are free of Li_2CO_3. LHDC, however, seems to incorporate alcohol functionalities, supposedly due to incomplete formation of the lithium alkoxides or conversion to the carbonate.

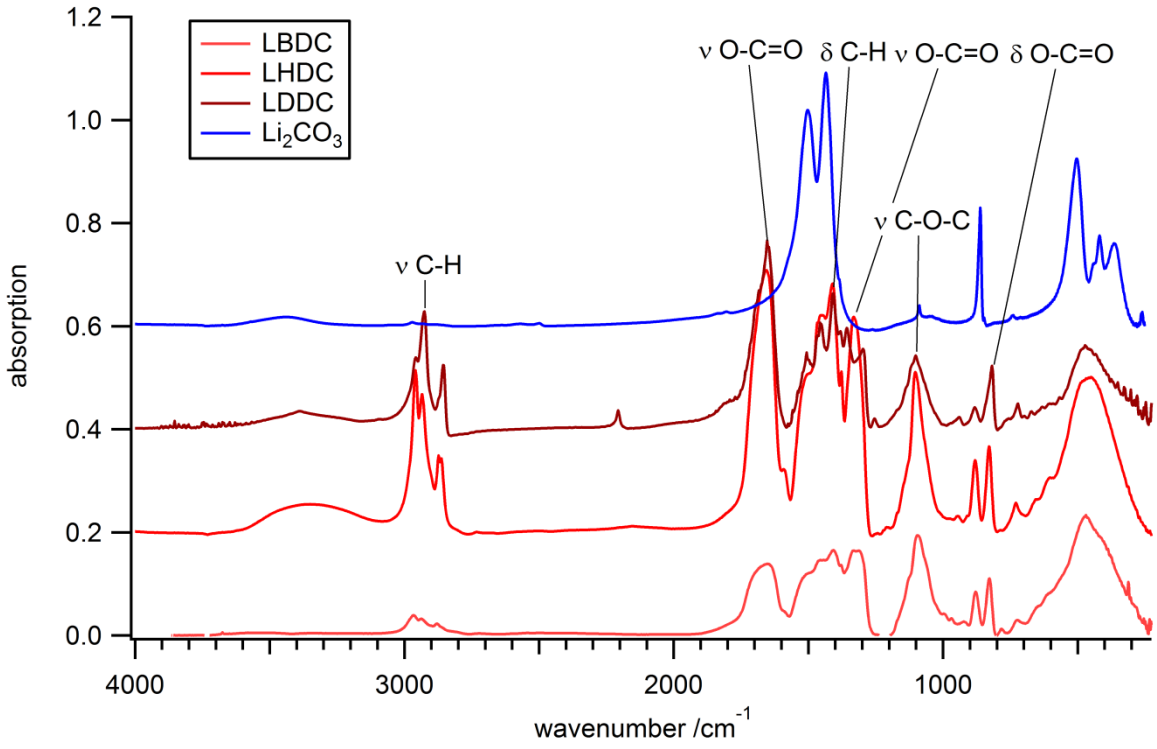

Fig. 6: FTIR-spectra of lithium dicarbonates from LBDC (bottom) to LDDC (top). Li_2CO_3 is depicted as reference (blue line). The offset between the baselines is 0.2.

Fig. 7 depicts the spectra of the sodium alkyl monocarbonates, which were compared to the spectra of Na_2CO_3 found in the literature. Na_2CO_3 exhibits a very strong peak at 1440 cm^{-1}, a strong and very broad band at around 2800-3600 cm^{-1} and a medium peak at 880 cm^{-1}. The spectra recorded with the organic carbonates bear no evidence of the latter two peaks, as the sharp bands at 2800-3000 cm^{-1} originate from C-H stretching vibrations. As no O-H bands are present, the products do not contain alcohol contaminations. Similar to the lithium carbonates, a distinctive carbonyl peak is observed at 1600-1650 cm^{-1}, adjacent to several bands in the area of 1300-1500 cm^{-1}. The medium bands at 1310-1390 and 1050-1110 cm^{-1}, again corresponding to C=O rocking and C-O stretching vibrations, are likewise observed for both alkali metals.

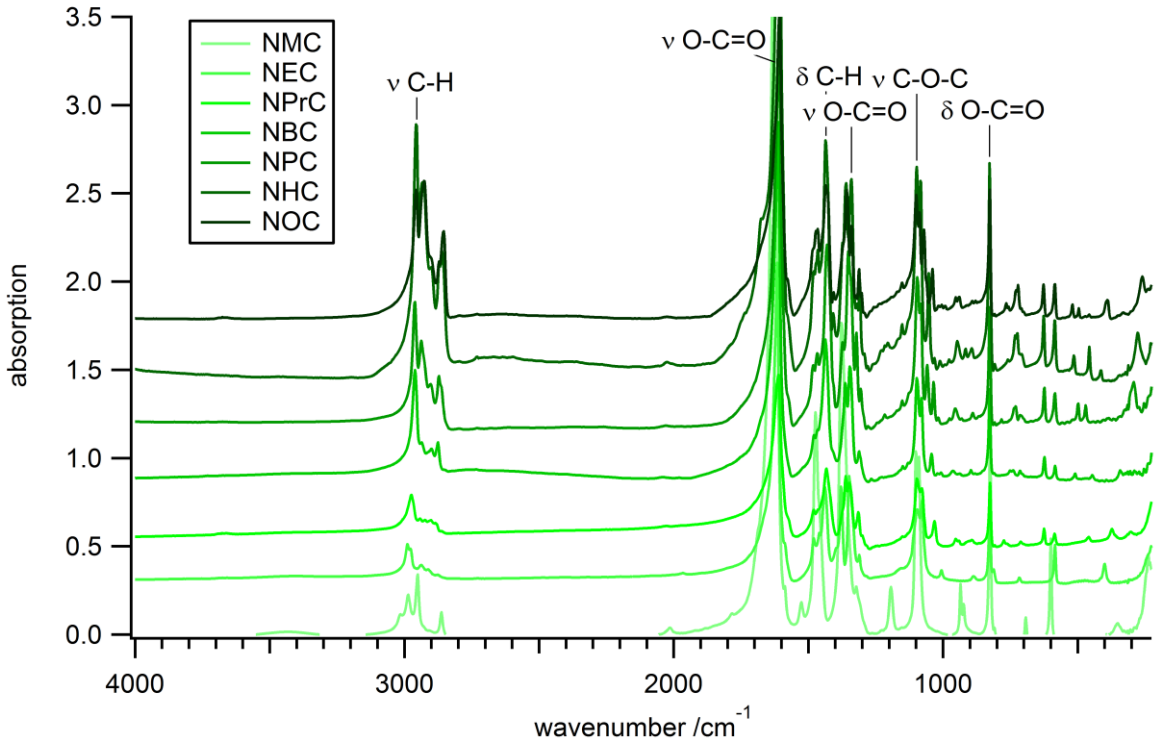

Fig. 7: FTIR spectra of all sodium carbonates from NMC (bottom) to NOC (top). The offset between the baselines is 0.3.

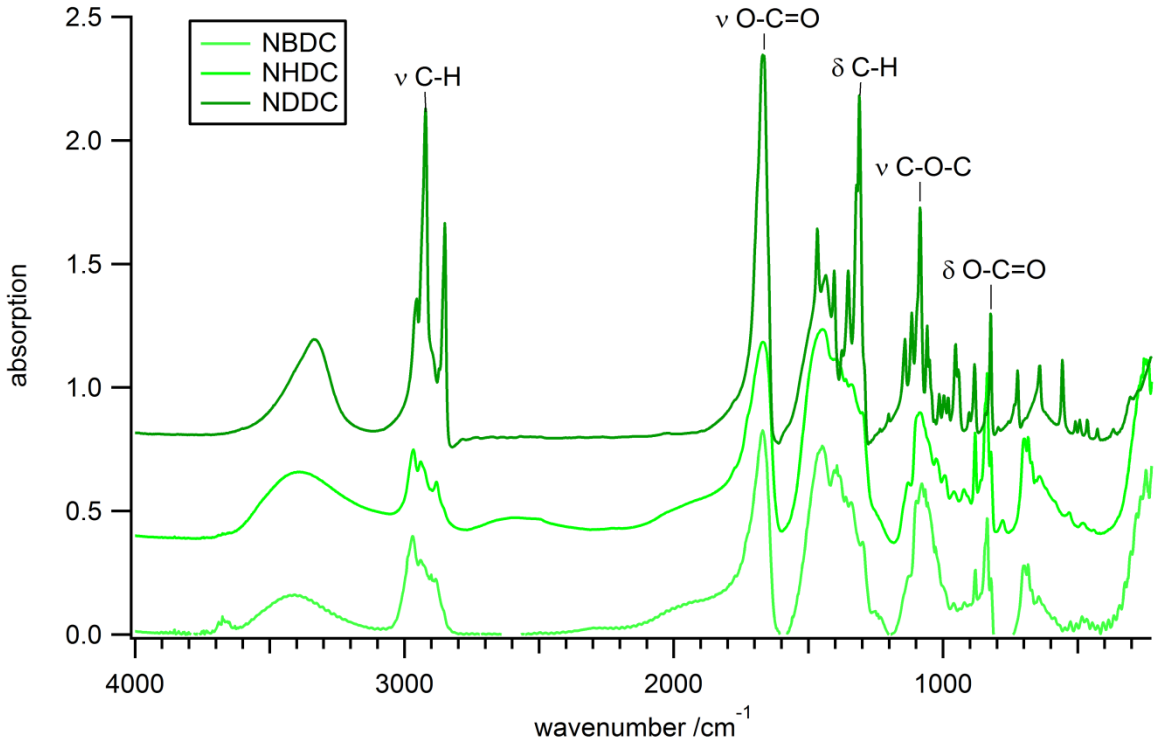

Fig. 8: FTIR-spectra of sodium dicarbonates from NBDC (bottom) to NDDC (top). The offset between the baselines is 0.4.

Applying a similar argumentation to the sodium alkyl dicarbonates (see Fig. 8), it can be concluded that they do not contain Na_2CO_3. However, the medium and broad band above 3100 cm^{-1} indicates a significant concentration of alcohol groups. Presumably, this is due to the lower reactivity of sodium hydride as compared to the *n*-butyl lithium employed in the lithium alkyl dicarbonate synthesis. This

effect seems to prevail over prolonged reaction times, leading to incomplete deprotonation of the alcohol and thus to remaining alcohol functionalities.

Table 1: Summary of all assigned vibrations for Li_2CO_3, lithium and sodium carbonates.

Compounds	Functional group	Vibration /cm^{-1}
Li_2CO_3	ν C-O	1495, 1432
	δ O-C=O	862
R-CO_3Li	ν C-H	3000-2860
	ν O-C=O	1660-1610
	δ C-H	1450-1410
	ν O-C=O	1380-1330
	ν C-O-C	1130-1080
	δ O-C-O	850-810
R-CO_3Na	ν O-H	3600-3100
	ν C-H	3000-2800
	ν O-C=O	1650-1600
	δ C-H	1460-1400
	ν O-C=O	1390-1310
	ν C-O-C	1110-1050
	δ O-C-O	850-810

3.1.2 Thermal stability and decomposition

The SEI components were subjected to differential scanning calorimetry (DSC) and thermogravimetric analysis with mass spectrometry (TGA-MS) to identify phase transitions and assess their thermal stability.

3.1.2.1 Thermal stability

Decomposition generally starts with a gradual mass decrease, thus a precise determination of the onset is difficult. Therefore, the highest temperatures with more than 90 % of the mass remaining were used for comparison. The results are presented in Fig. 9.

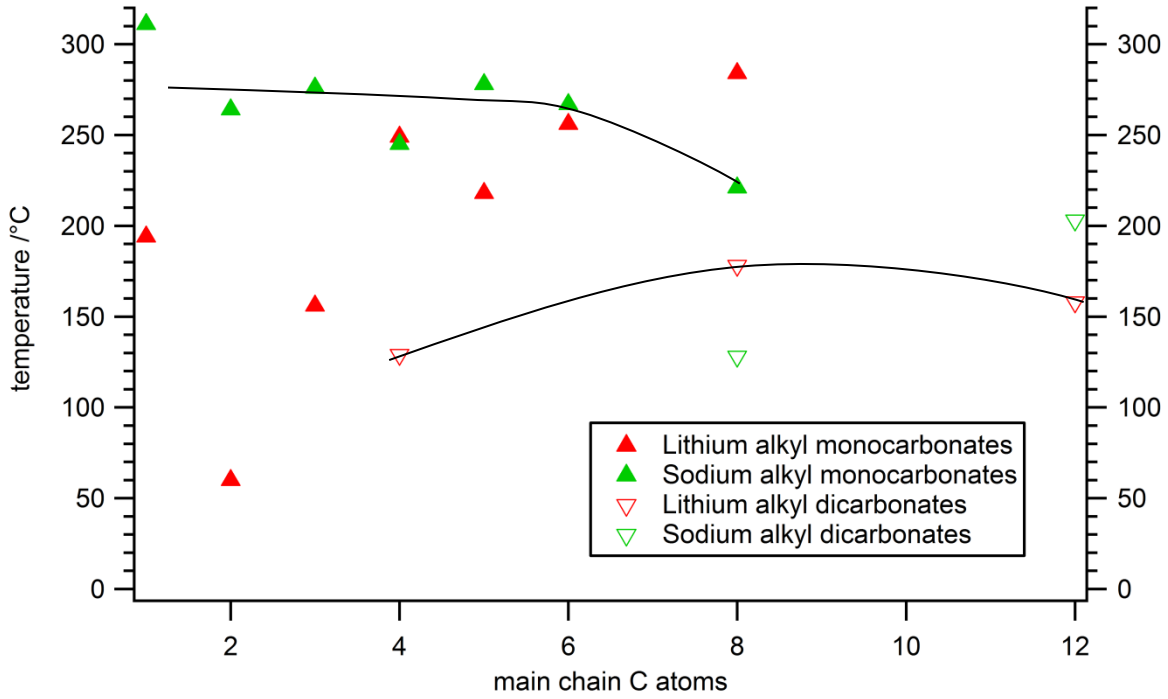

Fig. 9: Decomposition temperatures for lithium and sodium alkyl carbonates (filled) and –dicarbonates (empty triangles).

The sodium compounds show higher thermal stability than the lithium containing SEI components, decomposing mostly at >200 °C and >150 °C, respectively. While no significant influence of the chain length was observed, dicarbonates are somewhat less stable with LBDC decomposing above 129 °C and LDDC above 159 °C. Once again, LEC deviates from the behavior of its homologues, as considerable mass decrease starts already at 60 °C, presumably due to contamination with Li_2CO_3 and possibly other substances. The other SEI components, however, are stable in the temperature region relevant for lithium ion batteries and where the conductivity spectra were measured in pouch cells.

Phase transitions were not found in this temperature range, with one notable exception. LDDC exhibits a peak at 48,7 °C. As a melting process or a decomposition reaction are unlikely at this temperature (pellets for electrochemical impedance spectroscopy (EIS) measurements were heated to 100 °C without visible signs of decomposition, see below), the peak probably relates to a phase transition, which might be of interest in EIS studies.

3.1.2.2 Emitted ions

During the DSC/TGA analysis, emitted ions were continually monitored by mass spectroscopy. The resulting MS spectra were similar for all samples, featuring three large peaks at m/z ratios of 18, 28 and 32, with 28 being the base peak for all spectra. Those peaks appeared over the complete meas-

urement, even after the decomposition had finished, and were attributed to remaining N_2, O_2 and H_2O in the measurement device. Furthermore, a multitude of m/z ratios specific to the decomposition process could be observed, the most prominent m/z ratios being shown in Table 2.

Table 2: Detected masses and relative abundance in Methyl-, Ethyl-, Propyl- and Butylcarbonates and presumed formula of the ions. Ions marked with a minus were not detected, wave, plus and two pluses mark increasing relative abundance.

m/z	Relative abundance in -carbonates				Proposed structure
	Methyl	Ethyl	Propyl	Butyl	
15	+	~	~	~	CH_3
26	-	+	~	~	C_2H_2
27	-	+	+	+	C_2H_3
29	+	+	+	+	CHO
31	~	+	++	++	CH_3O
39	-	-	~	+	C_3H_3
41	-	-	+	+	C_3H_5
42	-	-	+	+	C_3H_6
43	-	~	+	+	CH_3CO
44	+	+	+	+	CO_2
45	+	+	-	~	H_3COCH_2
46	+	~	-	-	H_3COCH_3
55	-	-	-	~	C_4H_7
56	-	-	-	+	C_4H_8

The proposed structure of the ion was derived from the m/z ratio and the molecular formula of the parent SEI component. A m/z ratio of 29, for example, could correspond to both C_2H_5 and CHO. A C_2H_5 fragment, however, is unlikely to originate from LMC. As this is the case, the peak was attributed to CHO. Similarly, the ions at m/z 39-42 are only observed in carbonates with three or more carbon atoms in the main chain. For longer carbonates even small quantities of m/z 68-70 and 82-84 were detected.

3.1.2.3 Decomposition products

The thermal decomposition of LMC was studied in detail by Ross et al. by means of DSC/TGA-FTIR, identifying two decomposition products.[86] In the predominant reaction, CO_2 is released forming lithium methoxide (eq. 7). The second reaction yields Li_2CO_3 while CO_2 and dimethyl ether were detected in the gas phase (eq. 8). Our data for LMC is in good agreement with these results, showing similar thermal behavior, mass loss and CO_2 and dimethyl ether as gaseous reaction products.

$$\mathrm{ROCOOLi} \longrightarrow \mathrm{ROLi} + \mathrm{CO_2} \quad (7)$$

$$2\ \mathrm{ROCOOLi} \longrightarrow \mathrm{ROR} + \mathrm{Li_2CO_3} + \mathrm{CO_2} \quad (8)$$

Care has to be taken in interpreting the results for LEC due to the contaminations present. As in LMC, two endothermic processes mark the beginning and the end of significant mass loss in LPrC (see Fig. 10). In contrast, higher lithium homologues show a more complex behavior. Three endothermic peaks are normally found in the beginning and during the temperature range where mass loss occurs. Additionally, mass loss often proceeds in two clearly distinguishable steps, the second one being more pronounced for greater chain lengths. Interestingly, this second step is not associated with an endothermic process. In fact, sometimes even small exothermic peaks concurred with the mass loss.

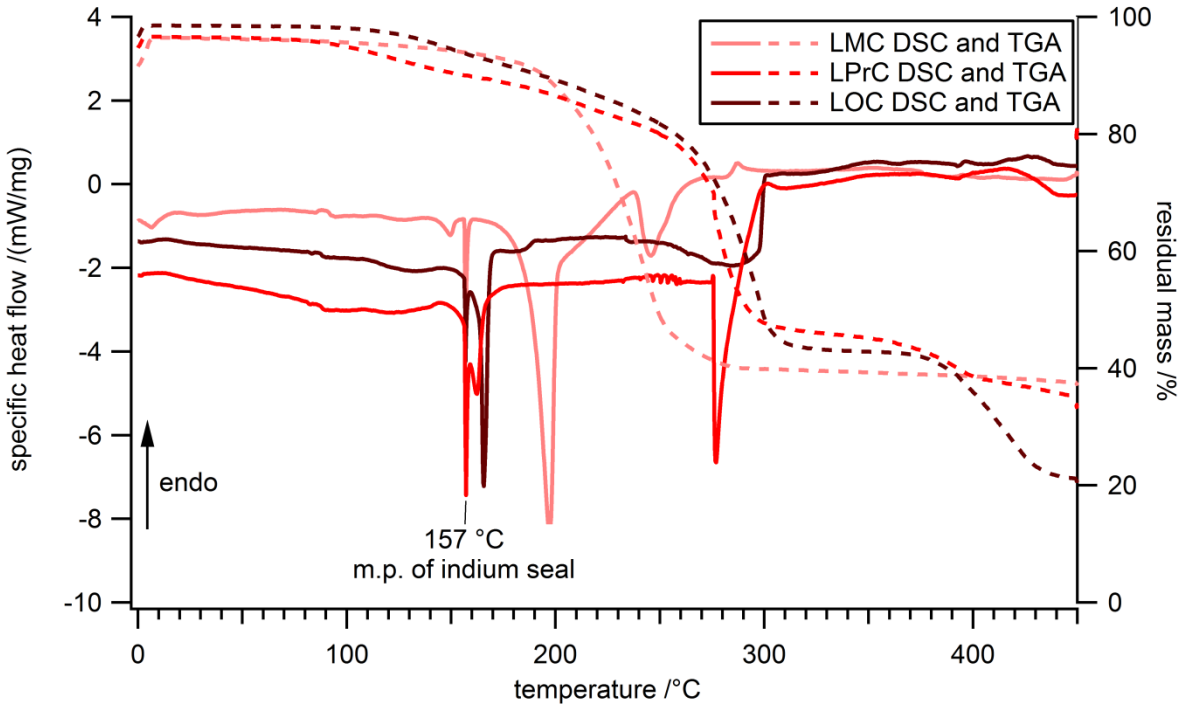

Fig. 10: Exemplary DSC (lines) and TGA (dashed lines, secondary axis) data for LMC, LPrC and LOC. The melting of the indium sealing causes the sharp peak at 157 °C.

Sodium carbonates again differ from their lithium analogues. NMC and NEC show only a single, large endothermic peak during the mass loss. This indicates that only one of the two reaction mechanisms identified by Ross takes place. As both CO_2 and dimethyl ether were detected by MS, the reaction product is probably sodium methoxide. Higher sodium alkyl carbonates exhibit three or more endothermic peaks mostly at the beginning of the decomposition process, as seen in Fig. 11.

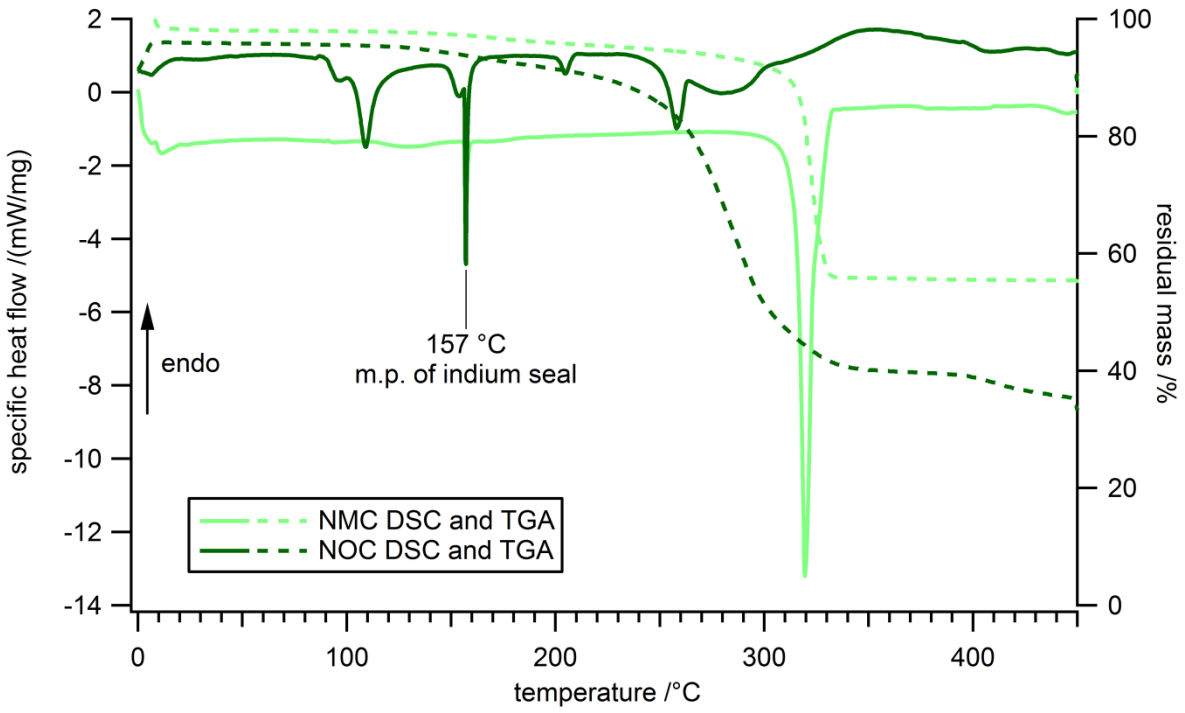

Fig. 11: Exemplary DSC (lines) and TGA (dashed lines, secondary axis) data for NMC and NOC. NMC melts in a single, sharp decomposition step with only one endothermic peak, whereas NOC shows several smaller peaks.

Although it is difficult to assign specific reactions to all endothermic peaks, our data allows conclusions regarding the solid decomposition product. Inevitably, this product must contain the alkali metal, thus lithium and sodium salts are likely candidates. Therefore I compared the residual mass of a specific sample with the theoretical residual masses if the only reaction product were, for example, Li_2CO_3 or sodium alkoxide. For instance, if NHC decomposed solely to Na_2CO_3, 31,5 % of the original mass should remain in the crucible. This value increases to 73,8 % if the product was sodium hexoxide. The results are presented in Fig. 12.

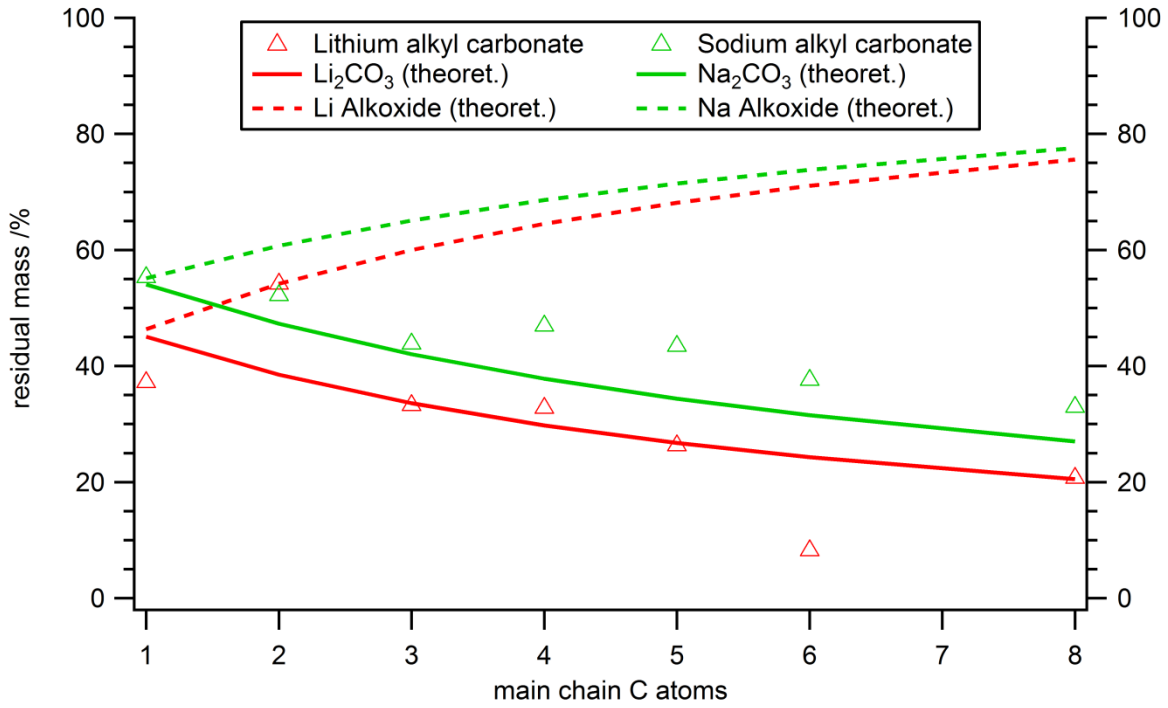

Fig. 12: The residual mass of all lithium- and sodium alkyl carbonates (triangles) is compared to the residual mass if the single decomposition products were alkali metal carbonates (lines) or alkali metal alkoxides (dashed lines). Apparently, inorganic carbonates are the predominant residues for higher homolgues.

Evidently, alkoxides can be excluded as predominant decomposition products of long-chain alkali metal carbonates. Thus, while Yang's findings on LMC are unchallenged, they cannot be straightforwardly extended to longer carbonates. Fig. 5 suggests that, despite major aberrations, the inorganic alkali metal carbonates are probably the main solid residue. These deviations can be explained by weighing errors in the sample preparation caused by pressure changes in the glove box, accounting to a large relative error (sample weight 2-3 mg). Additionally, the decomposition might have been incomplete or yielded side products. Lastly in LEC, Li_2CO_3 was incorporated already after the synthesis elucidating the drastically higher measured residual weight.

In conclusion, our results suggest that all studied SEI components are thermally stable at temperatures relevant to following SEI measurements and application in batteries and mainly decompose to Li_2CO_3 and Na_2CO_3 upon further heating.

3.1.3 Molecular Arrangement

Further structural information was obtained from powder X-ray diffraction (PXRD) and small-angle X-ray scattering (SAXS). The samples were filled in glass capillaries and enclosed with silicon rubber under inert atmosphere. Outside the glove box, the capillaries were flame sealed and sent for analysis.

Experimental difficulties included breaking the extremely thin (0.01 mm) glass capillaries by incautious manipulation, disintegration in XRD vacuum or slow decomposition due to imperfect sealing. The latter was apparent after the first measurements, that were conducted a week after sample preparation, when several samples appeared moist or yellowish. Therefore, samples were prepared immediately before the measurement and scrutinized carefully afterwards. Once more, the diffractograms were compared with reference patterns for the respective inorganic carbonates, oxides and hydroxides. The diffractogram of LEC contained Li_2CO_3, which is consistent with the results obtained from FTIR and TGA. In addition, the diffractograms of LHDC and to lesser extent LDDC contain Li_2CO_3 (Fig. 18), although both display additional peaks. Both decomposition in possibly not ideally sealed capillaries and a general resemblance of the spectra could justify this finding since the IR spectra (Fig. 6) confirmed initial purity of the samples. Other contaminants could not be found.

Data from both SAXS and XRD were obtained in a 2 theta range of 4.51 to 8.43. The results were consistent with only negligible shifts of the peak maxim, confirming the reliability of the methods. The spectra for lithium alkyl carbonates are presented in Fig. 13 and Fig. 14. Besides LEC, these samples display highly ordered phases. The SAXS spectra prove that interlayer spacing corresponds with chain length. However, a lamellar structure would exhibit several peaks with equal spacing, as reflections of higher order are observed. Therefore, the solitary peak of LBC at 4.12 nm^{-1} (SAXS) and 5.75 ° (XRD) is due to a crystalline, not lamellar, structure. LHC and LOC, in contrast, form lamellar structures, with three maxima observed for a interlayer distance of 19.8 and 23.8 Å, respectively. The spectra clearly establish that alkyl carbonates indeed form lamellar phases when the alkyl chain exceeds four carbon atoms.

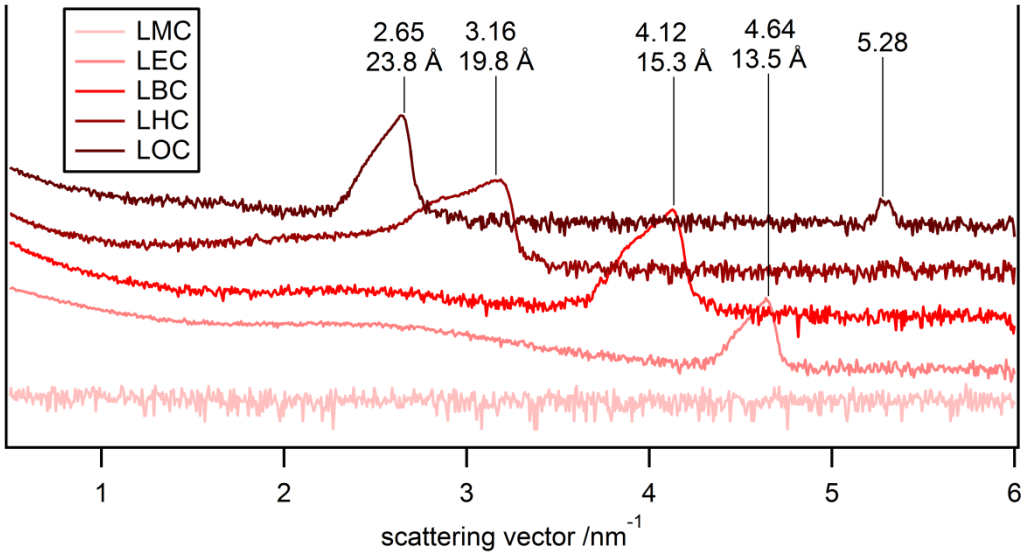

Fig. 13: SAXS patterns of lithium alkyl carbonates. Tags annotate the scattering vector of each peak and the corresponding interlayer distances.

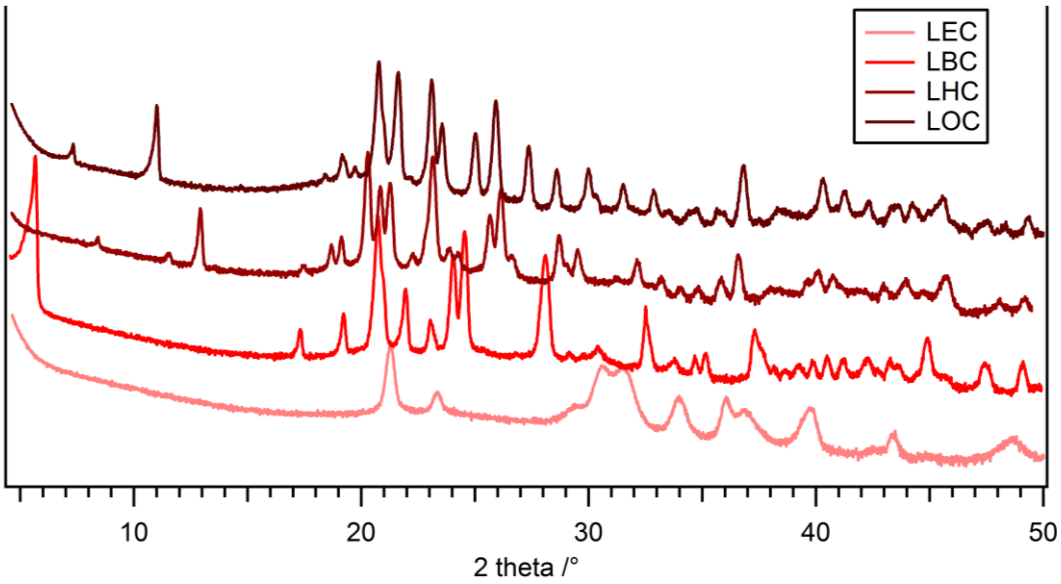

Fig. 14: PXRD patterns (2Θ CuK_α) of lithium alkyl carbonates. LEC strongly resembles Li_2CO_3.

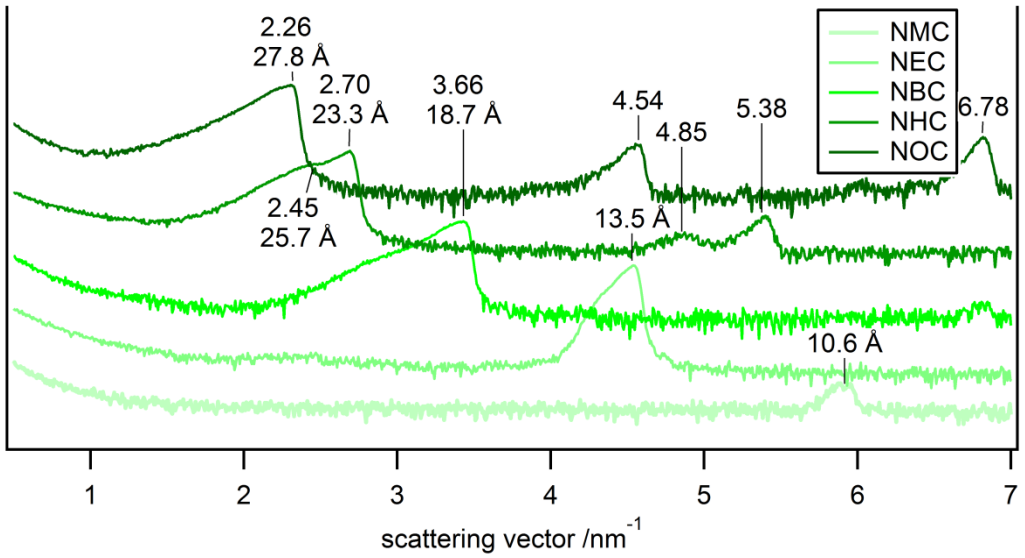

Fig. 15: SAXS patterns of sodium alkyl carbonates. Interlayer distances are higher than for the lithium analogues.

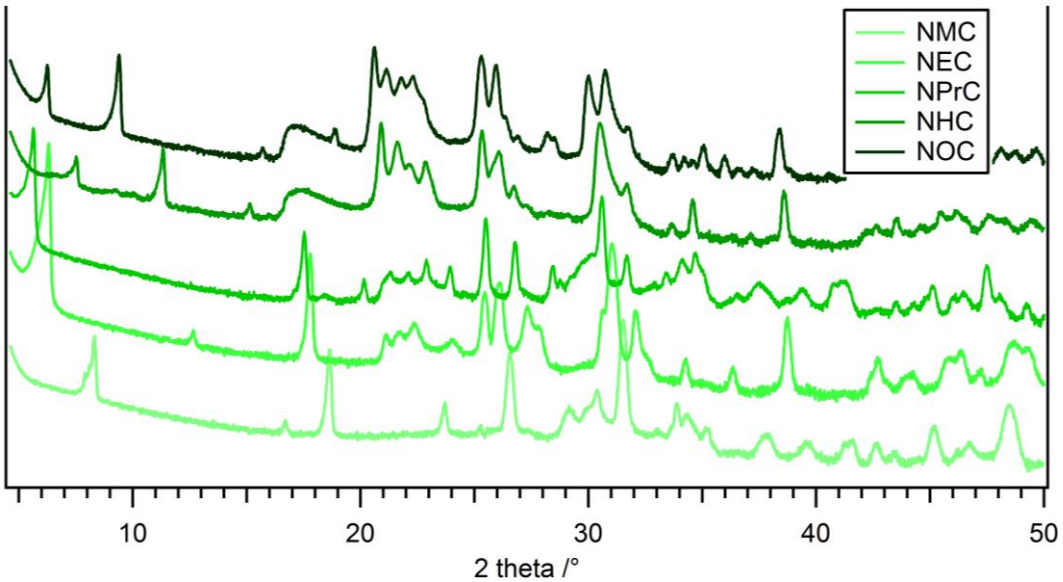

Fig. 16: PXRD patterns (2Θ CuK_α) of sodium alkyl carbonates.

Sodium alkyl carbonates behave almost identical to their lithium analogues (see Fig. 15, Fig. 16). All structures show distinct reflexes, disproving an amorphous phase. Interlayer distances are generally slightly higher for sodium. Interestingly, however, NMC and NEC displayed recurring peaks at low angles (two leftmost peaks in Fig. 16), albeit less pronounced than NHC and NOC. Considering the structure of e.g. LMC with its large polar head group and an almost insignificant apolar tail, a bilayer structure is highly unlikely.

In contrast, short dicarbonates are amorphous, with LBDC not featuring any peak in XRD or SAXS. The structure is more ordered for sodium and longer chain lengths, however, as demonstrated in Fig. 17 and Fig. 18. Lamellar structures were identified for NHDC, NDDC and LDDC. Interestingly, two different lattices are observed in the sodium samples. Arguably, this could be due to incomplete conversion of the alkoxides into the carbonate are the remaining alcohol in the synthesis as detected by FTIR. Chains with alcohol groups are significantly shorter than the sodium carbonates, thus accounting for a shorter interlayer distance.

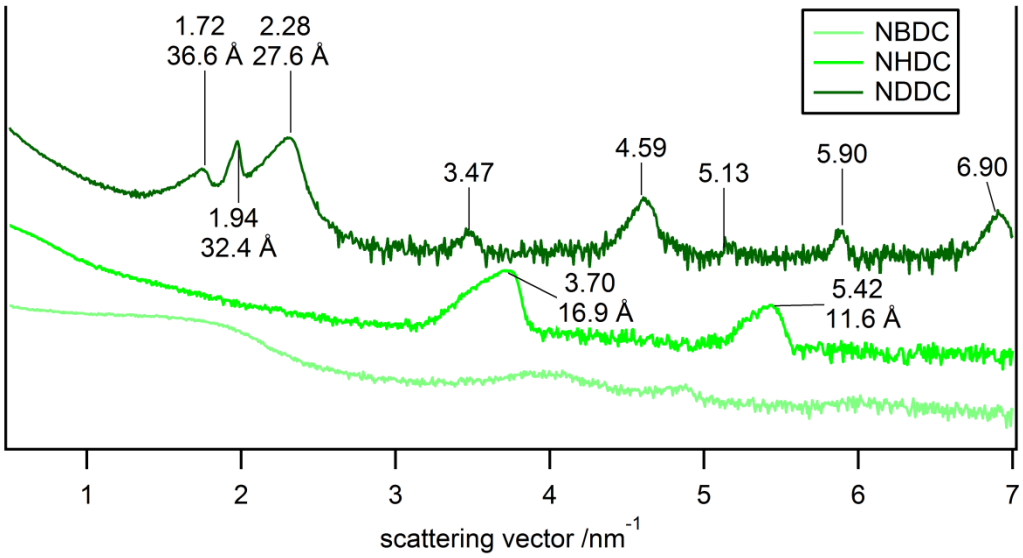

Fig. 17 SAXS patterns of sodium alkyl dicarbonates. NHDC and NDDC exhibit likely an intergrowth of two different lattices with different spacing.

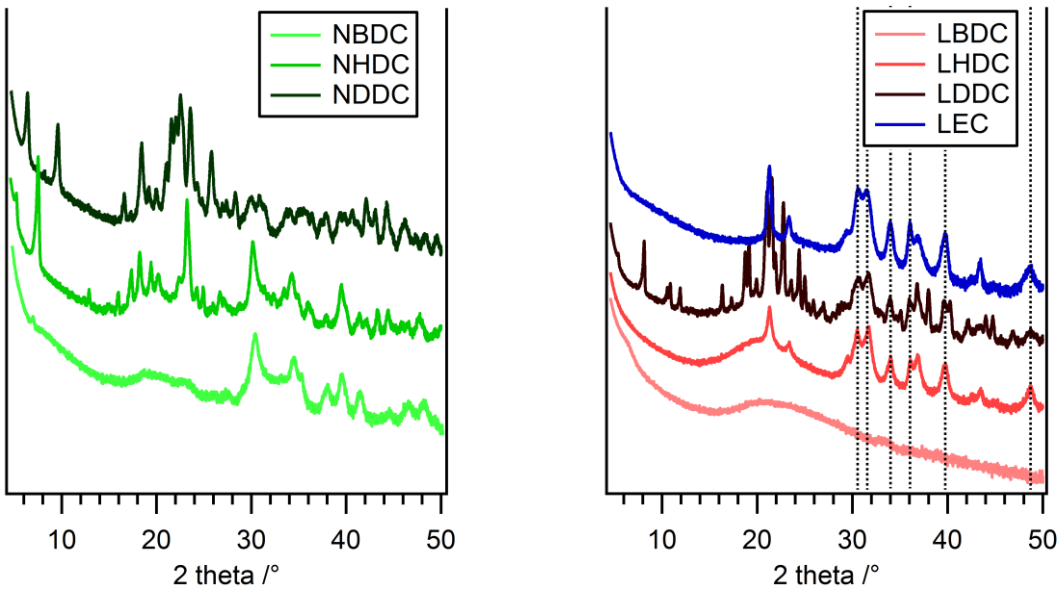

Fig. 18: XRD patterns of sodium (left) and lithium alkyl dicarbonate (right). LEC is added to the right figure for comparison.

Structural reasons can readily explain the larger disorder in dicarbonates as well. Assuming an ordered bilayer structure for monocarbonates, the additional $–CO_3M$ moiety disrupts the stacking and reduces order. Importantly, the disruption is limited to the polar head of the molecules, thus influencing short-chained polar molecules as LBDC and NBDC more severely than the longer, more apolar molecules like NDDC and LDDC.
Furthermore, the crystallite sizes were estimated employing the Debye-Scherrer equation (eq. 9)

$$\tau = \frac{K * \lambda}{\beta * \cos\theta} \tag{9}$$

with τ as the average size of an ordered domain, K the shape factor close to unity, λ the wavelength (0.154 nm), β the full width at half maximum of a peak in radians and θ the Bragg angle of the respective peak. Both K and β were assumed to be one, thus neglecting shape factor and peak broadening due to other reasons than crystallite size. Consequently, the results are relative estimates for comparison rather than exact values (see Table 3). For lithium samples, the crystallite size increases with the chain length, whereas for sodium samples an inverse relationship is observed.

So far, however, a bilayer structure was only assumed to constitute the layered structure observed but no proof or even cue was presented. To rationalize this postulation, the lengths of the SEI component molecules were calculated for an ideal all-trans configuration. For *n* carbon atoms, the length *L* is given by eq. 10

$$L = (n-1) * \sin(\alpha) * l(C-C) + l(C-O) * (\sin(\alpha) + 2 * \sin(\gamma)) \tag{10}$$

where α is the tetrahedron angle (109.5 °), *l*(C-C) is the carbon-carbon bond length (1,53 Å), *l*(C-O) the carbon oxygen bond length (1.43 Å) and γ the bond angle in the sp^2 hybridized carbonate group (120 °C). Note that this calculation do not consider the ion situated between the two hybridized oxygen atoms. The results were multiplied by 2 to emulate a bilayer with alkyl chains that do not overlap and were then compared with the values obtained from SAXS and XRD measurements, as shown in Table 3.

Table 3: Crystallite sizes, calculated and measured bilayer diameters.

sample	crystallite size /nm	bilayer diameter /Å		sample	crystallite size /nm	bilayer diameter /Å	
		cal.	mes.			cal.	mes.
LMC	-	7,3	10,4[a,b]	NMC	51	7,3	10,6
LEC	26	10	13,5[b]	NEC	51	10	13,5
LBC	32	15	15,3[b]	NBC	-	15	18,7
LHC	54	20	19,8	NHC	47	20	23,3
LDC	52	25	23,8	NOC	49	25	27,8
LBDC	-	15	-	NBDC	-	15	-
LHDC	22	20	-	NHDC	41	20	16,9[c], 11,6
LDDC	53	35	29,8	NDDC	31	35	36,6, 27,6[c]

[a)] value taken from [87]; [b)] no lamellar structure observed; [c)] predominant phase;

Experimental and calculated data are in good agreement for the samples where lamellar structures were detected. The sodium samples display higher bilayer diameters, possibly due to the larger ion. Longer chains deviate slightly from the ideal behavior as hydrophobic interactions and chain flexibility increases, rendering ideal behavior unlikely. In conclusion, however, our results strongly suggest that long chained alkali metal carbonates form lamellar bilayered structures.

3.1.4 Conductivities

Finally the samples were subjected to EIS measurements to compare the influence of structure on conductivities. The samples were pressed, covered with a gold layer to ensure ion blocking electronic contact and embodied in airtight pouch cells. All preparation steps were executed under inert atmosphere to avoid contamination.

The measurements were conducted at frequencies between 10^{7} and 10^{-2} Hz and temperatures between -100 °C and 100 °C. Higher temperatures were avoided due to the limited stability of the pouch cell components as well as some of the samples. Direct current plateaus where conductivity is independent over a certain frequency range were identified, as shown in Fig. 19. It is assumed that the frequency-independent conductivity equals the direct current conductivity.

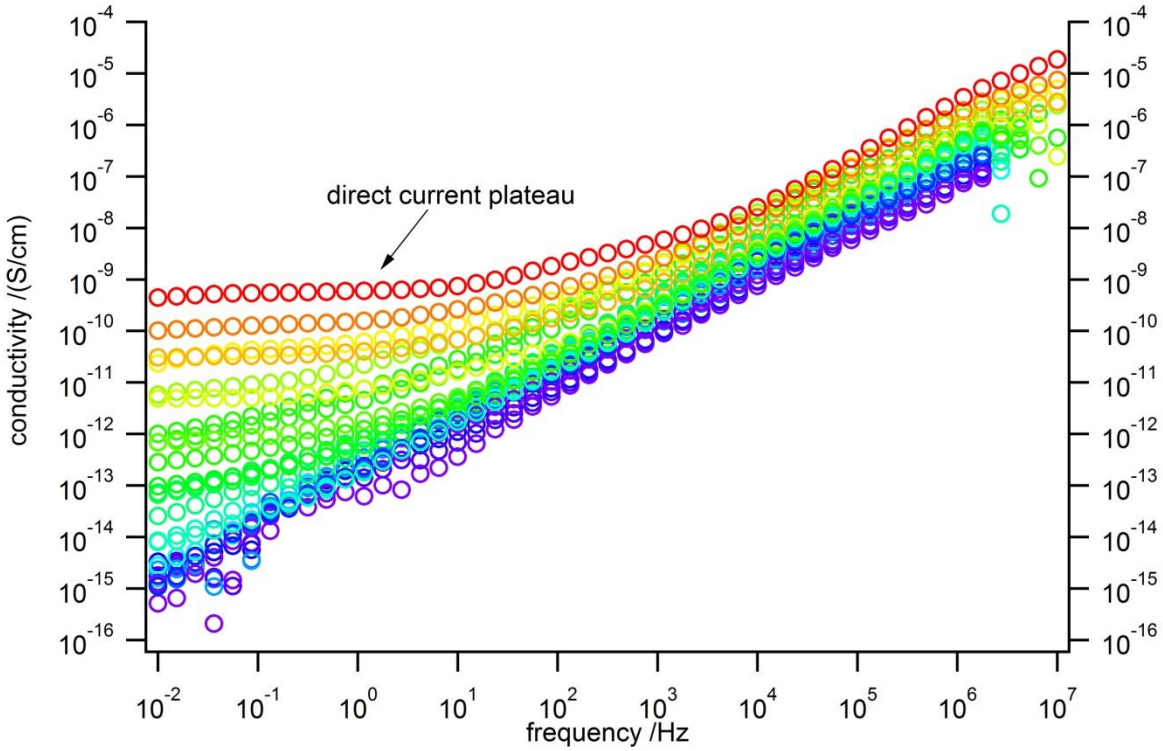

Fig. 19: Exemplary EIS data for LMC. The colors represent temperatures ranging from -100 °C (purple) to 100 °C (red). LMC displays direct current plateaus at elevated temperatures.

As most samples exhibited no distinctive direct current plateaus, the conductivities at two temperatures (20 °C and 100 °C) were compared. The results for lithium alkyl monocarbonates are presented in Fig. 20. Evidently the conductivity decreases with increasing chain length. This effect is more pronounced at 100 °C, while lithium ion mobility at 20 °C is similar for the higher analogues LBC, LHC and LOC. Hence, the influence of chain length is limited to shorter molecules.

Interestingly, there is no significant difference between lamellar and crystalline structures, as LBC and LHC show similar conductivities. In other words, Fig. 20 disproves our anticipation that lamellar structures would lead to increased overall lithium ion mobility.

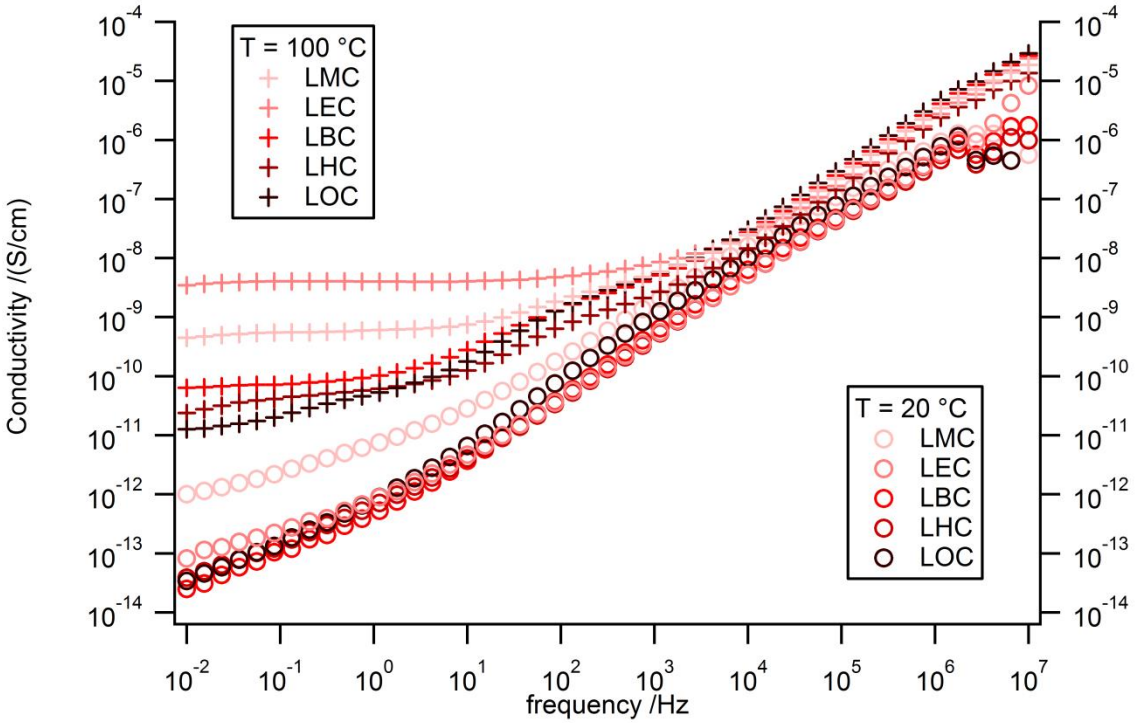

Fig. 20: AC Conductivities for lithium alkyl monocarbonates at 20 and 100 °C drop with increasing chain length. LMC, LEC and LBC exhibit constant current plateaus at 100 °C.

Introduction of Li_2CO_3 into the organic samples seems to positively affect conductivities at elevated temperatures, as the conductivities of LEC surpass even LMC at 100 °C. As described previously, however, thermal decomposition in LEC starts at temperatures as low as 60 °C. Therefore, thermal decomposition presumably causes this unexpected behavior. As the sample continually degrades over time, one would assume that the results obtained during the heating process differs from measurements during subsequent cooling. This would be visible in an Arrhenius plot from which also the activation energy can be determined.

The Arrhenius equation, already in its logarithmic form is eq. 11

$$\log(\sigma * T) = \log(A) - \frac{log\ (e) * E_a}{k_b * T} \tag{11}$$

with σ being the conductivity at a direct current plateau, log(*A*) the pre-exponential factor, T the temperature in Kelvin, E_a the activation energy, k_b the Boltzmann constant and log(*e*) a factor to compensate for not using the natural logarithm. The logarithm of $\sigma * T$ was then plotted against the inverse temperature to obtain a linear relationship, from which the activation energy is obtained (see eq. 12 respective figures).

$$E_a = \frac{slope * k_b}{\log(e)} \tag{12}$$

The Arrhenius plots for LMC and LEC are presented in Fig. 24. Surprisingly, the data point obtained during the cooling of LEC does not deviate from the trend. In contrast, LMC exhibits a significantly lower conductivity during the cooling process. Phase transition, chemical reactions and decomposition processes can be excluded as the DSC spectrum shows no peaks in this area. The release of

moisture at 100 °C is unlikely as well, given the reactivity of the sample towards water. Imaginably, the altered behavior is caused by a recrystallization process at elevated temperatures. The corresponding, broad exothermic peak might either be too indistinct to be observed or recrystallization occurs exclusively in the pellets that were subjected to large pressures and thus show a higher concentration of dislocations.

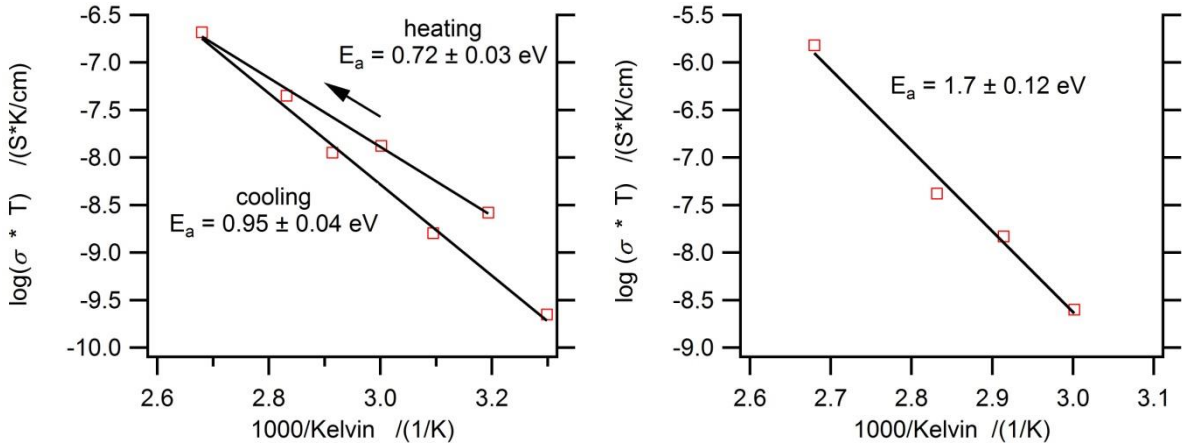

Fig. 21: Arrhenius plots of LMC (left) and LEC (right). The values obtained in the heating process differ from the cooling process for LMC, but not for LEC.

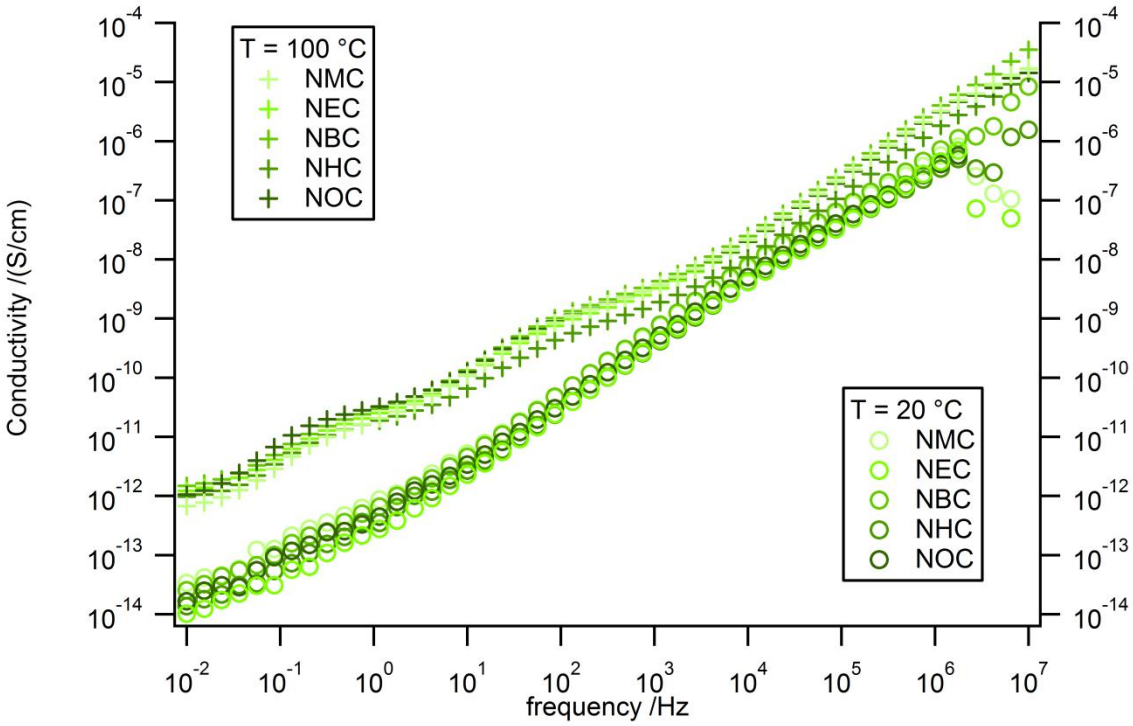

Fig. 22: AC conductivities for sodium alkyl carbonates with increasing chain lengths. Neither chain length nor structure correlate with conductivities.

As expected, due to the higher ionic radii for sodium compared to lithium, conductivities for sodium alkyl monocarbonates are inferior to its lithium counterparts. Astonishingly, however, neither variation of chain length or intermolecular arrangement results in significantly increased sodium ion mobility. Both structure and arrangement seem to have no effect whatsoever. The meager conductivities might imply that sodium alkyl monocarbonates are not paramount in sodium ion conduction

through the SEI. However, it is entirely possible that other SEI components exhibit even worse conductivities.

From another point of view, conductivities of longer sodium alkyl carbonates are equal to those originating from currently used electrolytes. Although electrolytes or additives yielding such decomposition products might not decrease interfacial resistance, they might ameliorate other SEI characteristics without hampering sodium ion transport.

The results for sodium alkyl dicarbonates are distinct in two ways. Firstly, all samples display direct current plateaus at elevated temperatures, NBDC and NHDC even at 20 °C enabling a comparison of direct current conductivity in Fig. 23. Secondly, conductivities surpass those of other samples by several orders of magnitude. In fact, the results differ so drastically from those observed for sodium alkyl monocarbonates and lithium alkyl dicarbonates as to raise concerns about whether sodium ion mobility is truly responsible for the observed conductivities. As explained previously, conversion in the synthesis of sodium alkyl dicarbonates was high but not complete. Remaining alcohol groups (pKa around 16-18) result in free protons that should, due to their small size, be highly mobile and could thus explain the unexpectedly high total conductivity.

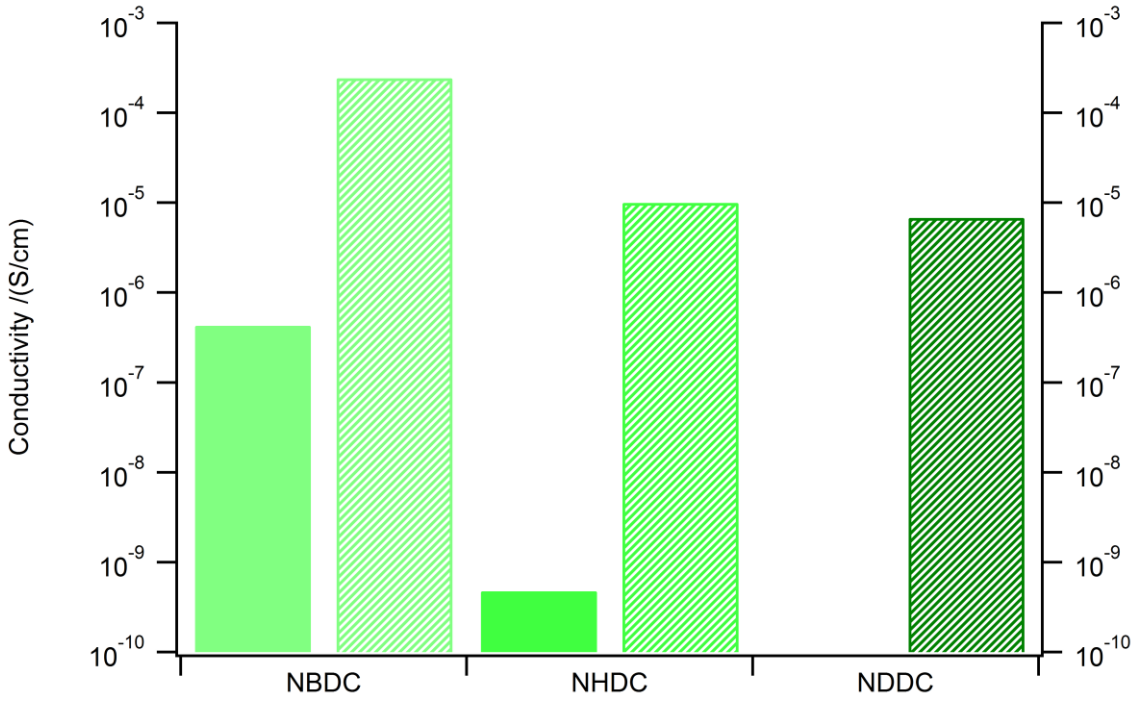

Fig. 23: Direct current conductivities for sodium alkyl dicarbonates at 20 °C (left, filled) and 100 °C (right, striped).

The correlation of conductivity with chain length is similar to that of lithium alkyl carbonates. Again, conductivity is highest for the shortest chains and decreases with chain length. Importantly, the difference is higher between NBDC and NHDC (4 and 6 carbon atoms in the main chain, respectively) than between NHDC and NDDC (6 and 12 carbon atoms), resembling the behavior of lithium alkyl carbonates.

The sodium alkyl dicarbonate's Arrhenius plots reveal that again there is a difference between the heating and cooling processes (Fig. 24 for NBDC and NHDC, see Appendix for NDDC). In contrast to

LMC, however, the conductivity increases during the measurement. This is reflected by drastically deviating activation energies, dropping from 0.74 eV to 0.41 eV and from 1.24 eV to 0.57 eV for NBDC and NHDC, respectively.

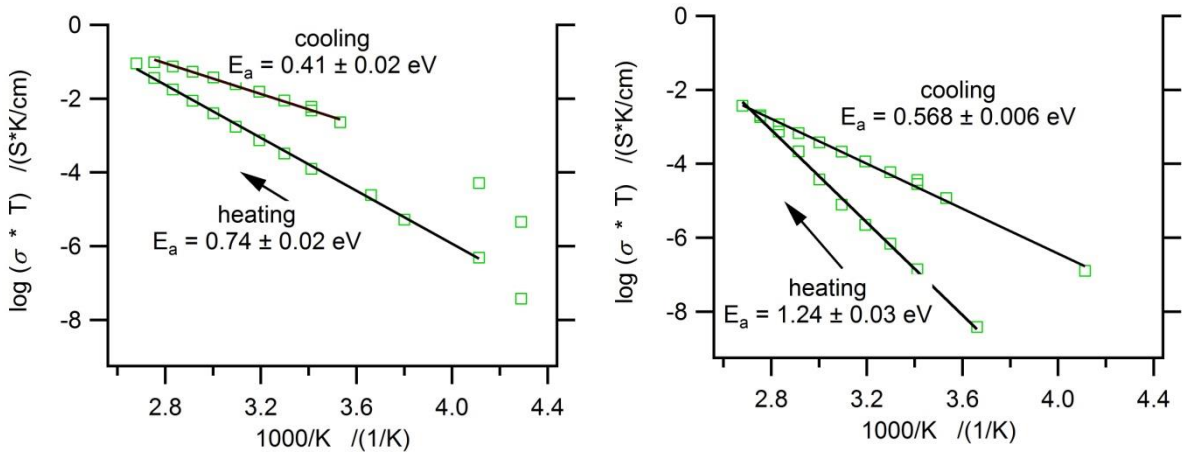

Fig. 24: Arrhenius plots of NBDC (left) and NHDC (right). Both samples show increased conductivity and lower activation energies during cooling.

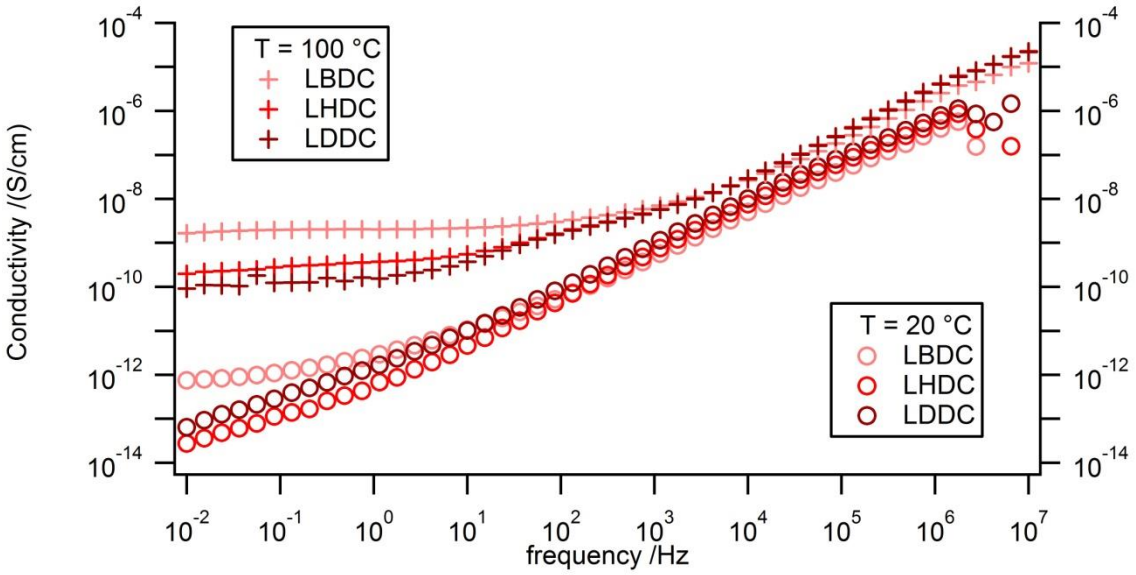

Fig. 25: AC conductivities of lithium alkyl dicarbonates at 20 and 100 °C drop with increasing chain lengths, although differences between LHDC and LDDC are small.

Results for lithium alkyl dicarbonates generally resemble the sodium analogues as a significant difference is observed between the shorter LBDC and LHDC samples, whereas the latter and LDDC display similar conductivities (see Fig. 25). The conductivity of LEDC is reported to be 10^{-10} which is consistent with the trend observed.[88] Compared to the sodium alkyl dicarbonates, total conductivities are roughly 6 orders of magnitude lower. However, conductivities still exceed those of lithium monocarbonates with LBDC showing slightly higher values than even LMC and LDDC outperforming long-chain monocarbonates by up to a factor of 10 at 100 °C.

In a first measurement, much higher conductivities were measured for LDDC, with dc conductivities of $3*10^{-10}$ at 20 °C and $8*10^{-6}$ at 100 °C. The corresponding Arrhenius plot is presented in Fig. 26, displaying a kink around 50 °C. The buckle perfectly matches the DSC data showing a large endothermic

peak at 48.7 °C. These results suggest that a phase change or chemical reaction not associated with thermal decomposition is responsible for a drastic decrease in activation energy. Despite this interrelationship, the measurement could not be reproduced in two identical experiments. Presumably, the increased conductivity is due to contact with moisture and Li_2CO_3 formation which was shown to improve conductivity at elevated temperatures for LEC and the interrelationship is a coincidence. The latter two experiments are unlikely to be compromised as, apart from the vapor deposition, both samples were handled separately. A leaky transport box would not have remained unnoticed as the leak results in an underpressure in the vessel during the transfer into the glove box. Thus it would have been impossible to immediately open the transport box.

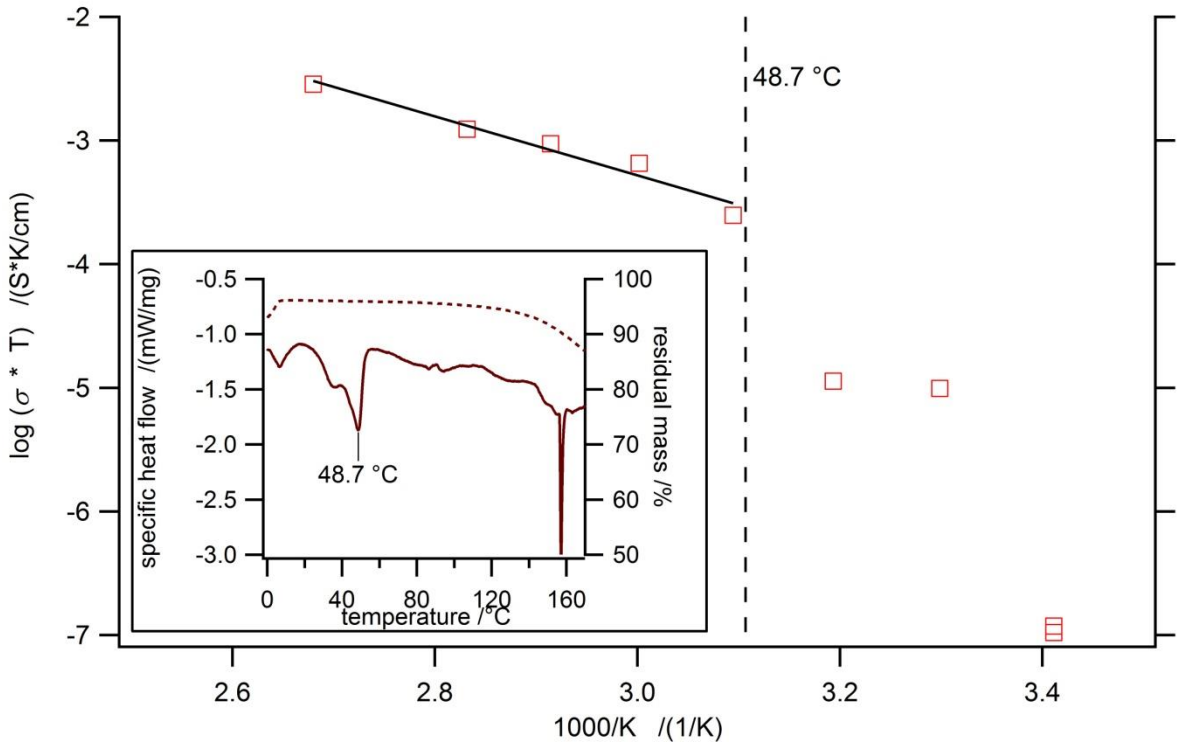

Fig. 26: Arrhenius plot for the first measurement of LDDC, showing a sharp bend at roughly 50 °C. The inset shows DSC and TG curves, with a significant endothermic peak at 48.7 °C indicating a phase change or a chemical reaction not related to decomposition.

To summarize, conductivities generally decrease with increasing chain length for short to medium chain lengths (1 to 4 C atoms). For longer chains, conductivity becomes largely independent of chain length. Besides the contaminated sodium dicarbonate samples, replacement of lithium with sodium diminishes conductivity, whereas alkali metal dicarbonates exhibit increased conductivity.

Importantly, these results suggest that lamellar structures do not significantly augment long range ion mobility. Increased volume fraction of insulating alkyl phase and/or tortuosity of lamellar phases could contribute to this unexpected result, the latter resulting in a longer diffusion pathway due to misaligned or angled domains. Solid state ^{6}Li and ^{7}Li NMR will be employed to further investigate local ionic mobility. In contrast, amorphous samples as the short chained butyl dicarbonates show the highest conductivities.

3.2 Preliminary electrolyte testing

Parallel to the study of decomposition products, several electrolytes designed to be yielding such or similar decomposition products were synthesized and characterized with respect to electrochemical stability, SEI formation on glassy carbon and their performance in testing cells with intercalation and alloying anodes.

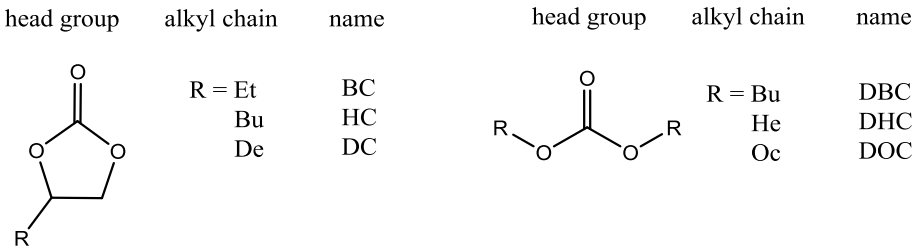

Fig. 27: Overview of the synthesized electrolytes and the respective abbreviations.

3.2.1 Electrochemical Stability

Oxidative and reductive stability of the electrolytes was determined by linear sweep voltammetry. All measurements were conducted at a low slew rate of 1 mV/s to inhibit the influence of polarization effects. The measurement system consisted of a glassy carbon working and lithium metal reference and counter electrodes, with the respective electrolyte and $LiPF_6$ as the salt. The concentration of $LiPF_6$ was varied from 0.2 to 0.4 and 1.0 mol/L of electrolyte so as not to disregard a correlation of salt concentration and stability. Limited solubility of $LiPF_6$ in more nonpolar electrolytes (DC, DHC, DOC) resulted in a viscous suspension at 1.0 mol/L electrolyte. Therefore, the last sweeps were performed at 0.7 (and 0.4 for DC) where a clear, albeit highly viscous, solution was obtained.

Utmost care was taken during the purification and drying of the electrolytes, as even traces of moisture or other contaminants interferes with electrochemical measurements. The crude products were purified by column chromatography to remove major impurities. Subsequently, the electrolytes (except DC due to its high boiling point) were distilled *in vacuo* and the collected fractions were dried at 60 °C under reduced pressure for at least 4 hours. The vacuum tap was then closed and the still evacuated flasks were moved directly to the glove box, where the electrolytes were stored at least 3 days over freshly activated molecular sieves. After this treatment, nuclear magnetic resonance (NMR) analysis showed no sign of contaminants for any of the electrolytes. However, NMR spectroscopy is not sensitive enough to identify traces of impurities. In fact, despite the rigorous measures described above, some electrolytes adopted a yellowish or brownish color after addition of $LiPF_6$, indicating the presence of significant traces of moisture.

The glassy carbon working electrode was polished, washed and dried at 80 °C after each measurement and the lithium electrodes were simply replaced in order to assure reproducible conditions. Especially polishing the working electrode proved critical as a surface film of decomposition products is formed during the measurement and deficient cleaning resulted in significant changes of the open circuit potential (OCV). Normally, the OCV against lithium was 2.7-3.1 V for every electrolyte.

The results are presented in Fig. 28. The outliers observed particularly for LP30 and BC are most likely due to pressure changes or vibrations in the glove box and could not be avoided by changes in the measurement setup. Interestingly, outliers were less frequent during overnight measurements, reinforcing this reasoning.

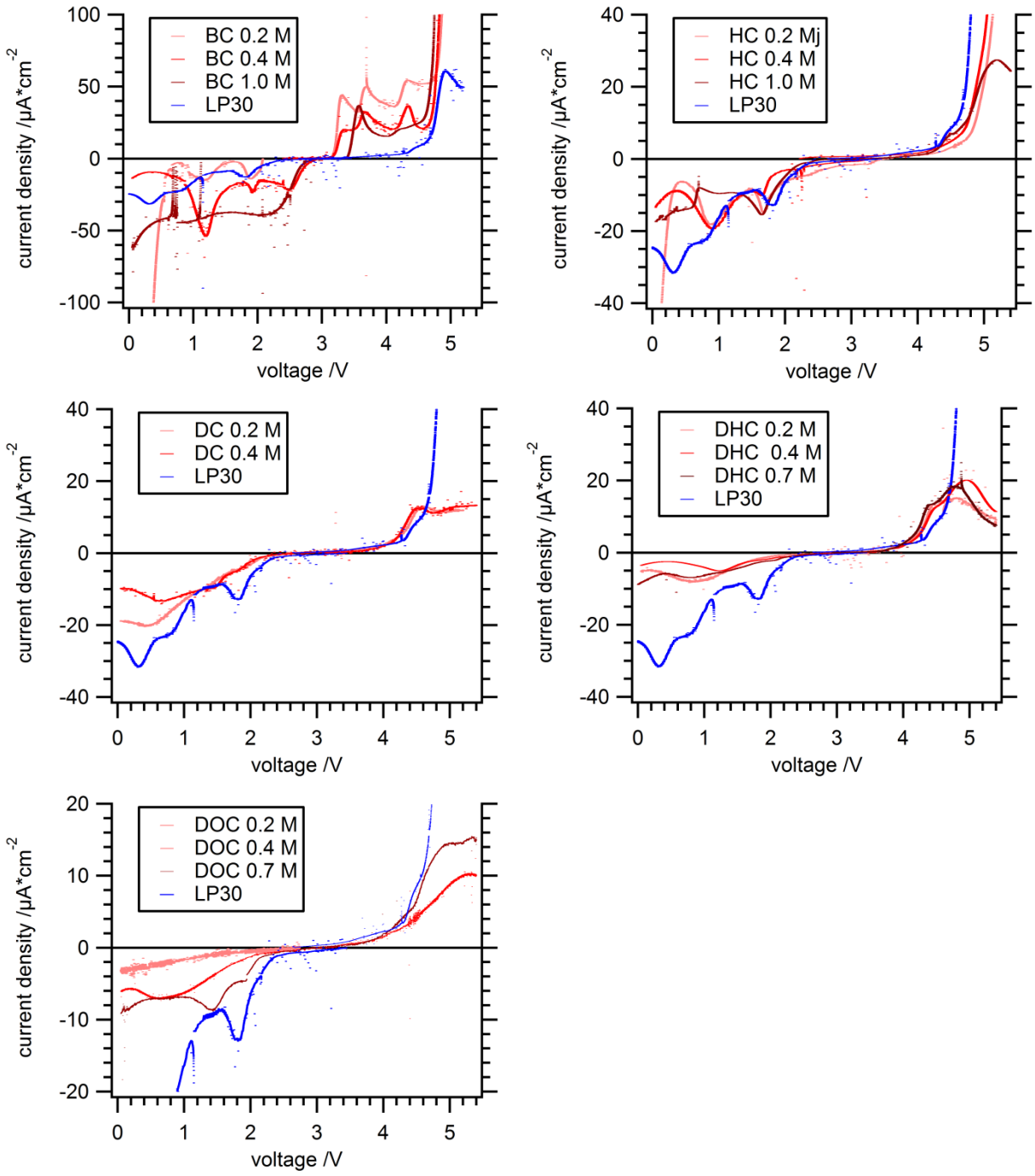

Fig. 28: Linear sweeps in oxidative and reductive direction at 1 mV/s for BC, HC, DC, DHC and DOC (from top left to bottom right). Darker colors show higher $LiPF_6$ concentrations, while commercial LP30 is shown as a comparison in blue.

Decomposition normally resulted in a gradual increase of current density, rendering the determination of its onset challenging. For the oxidative reactions, the linear region of each oxidative sweep was extrapolated to zero, using the corresponding voltage for comparison. Reductive sweeps rarely showed high current densities or a linear region, thus the onset was read from the diagram directly. Table 4 shows the results for the highest salt concentration tested. Oxidative stabilities of short chained cyclic electrolytes (BC, HC) were marginally higher than those of LP30, whereas DC and linear electrolytes showed reduced resistance to oxidation. Higher salt concentrations caused an earlier onset of decomposition for all electrolytes investigated, although the effect was almost negligible.

Table 4: Comparison of oxidative and reductive stabilities at the highest salt concentration investigated.

	LP30	BC	HC	DC	DHC	DOC
Oxidative dec. onset /V	4.67	4.70	4.72	4.11	4.07	4.27
Reductive dec. onset /V	2.37	OCV	2.16	2.17	2.12	2.22

Reductive stability was in the range of 2.4 to 2.1 V, with LP30 showing least resistance to reduction. As opposed to oxidation, a high concentration of $LiPF_6$ is not detrimental to cathodic stability. BC is a noteworthy exception to this, showing large current densities close to OCV. However, the results for BC (Fig. 28) show more unexpected features. Firstly, the current densities in general are several times higher than those of all other electrolytes including LP30, although BC and EC contained in LP30 are structurally similar. Secondly, three oxidative peaks are visible before oxidative degradation, where none would be expected for a carbonate based electrolyte. Most likely, BC is contaminated with an impurity that was not visible in NMR, thus compromising these measurements. Fortunately, oxidative stability can still be estimated from the sharp increase in current densities between 4.8 and 5 V.

Current densities decrease in the order of (BC >) HC > LP30 > DHC > DC > DOC, with more polar electrolytes showing maximum current densities. Besides polarity, salt concentration plays an important role. Nonpolar electrolytes like DOC showed minimal current densities at 0.2 M $LiPF_6$ (Fig. 28, bottom left), with a maximum of 2 $\mu A/cm^2$. Upon increasing salt concentration, higher current densities were observed. The results for HC highlight the limits of this effect, as the current density during oxidation at 1.0 mol/L is significantly lower than at 0.4 mol/L. Presumably, the increased viscosity at higher salt concentrations decreases conductivity.

To summarize, the electrolytes investigated (except BC) start to be reduced between 2.22 and 2.12 V, thus being somewhat more stable that LP30. In contrast, oxidative stability is reduced for more nonpolar electrolytes, with DHC decomposing already at 4.07 V.

3.2.2 SEI formation

In the next step, SEI formation on the glassy carbon electrode was examined. Therefore, I used the measurement system and samples (at the highest $LiPF_6$ concentration) described in the previous section and cycled each electrolyte 10 times in a range from OCV to 0.05 or 5.4 V, respectively. If the reduction or oxidation products indeed formed a stable SEI, the measured current densities would diminish from cycle to cycle, reflecting passivation or the decreasing free electrode surface.

The results were diverse, as can be seen in Fig. 29 for the cyclic electrolytes. The reductive region of BC shows almost no difference between the first and the last cycle, indicating no SEI formation at all. Similarly, anodic current densities remained at levels far surpassing other electrolytes. The reductive peak at around 3.5 V is also exclusive to BC and originates from the mysterious contaminant.

In contrast, HC showed a sharp decline in current densities, both during reduction and oxidation. The large peaks at 1.4 and 4.5 V disappear after the first cycle. Moreover, after ten cycles, the maximum current density during oxidation is 5 $\mu A/cm^2$ at a potential of 5.4 V, which translates to an almost 10 fold reduction compared to the peak in the first cycle. During reduction, current densities decline sharply as well, although significant currents can still be observed below 1.5 V. These results suggest that HC does form a stable SEI, particularly during oxidation.

The results for DC were somewhere between those intermediates. After ten cycles, its SEI is resistant to oxidation for up to 5 V, whereas reductive currents remain largely constant. Arguably, reduction involves changes at the highly oxidized carbonate group, which in DC constitutes a particularly small part of the molecule. The polarity might thus not change enough for the molecule to be insoluble preventing the formation of a stable SEI.

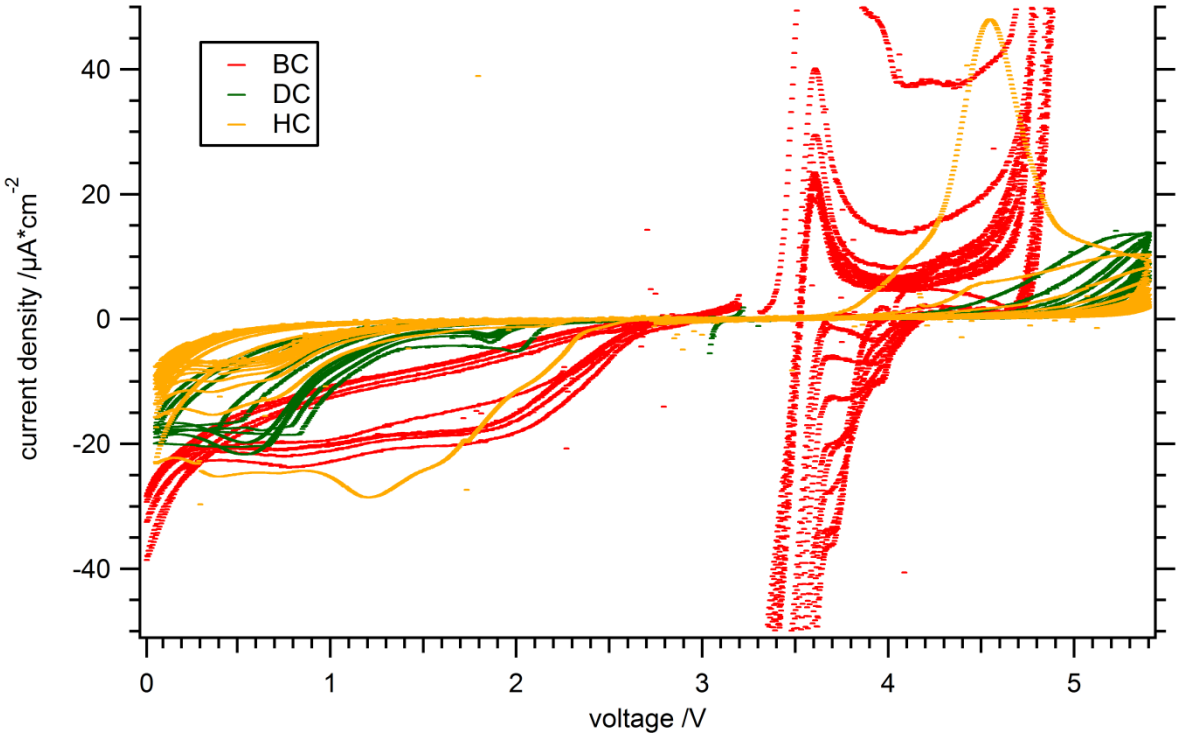

Fig. 29: Cyclic voltammogramms of the cyclic electrolytes BC (red), HC (orange) and DC (green). Anodic current densities decrease strongly for HC and DC, cathodic current densities only for HC.

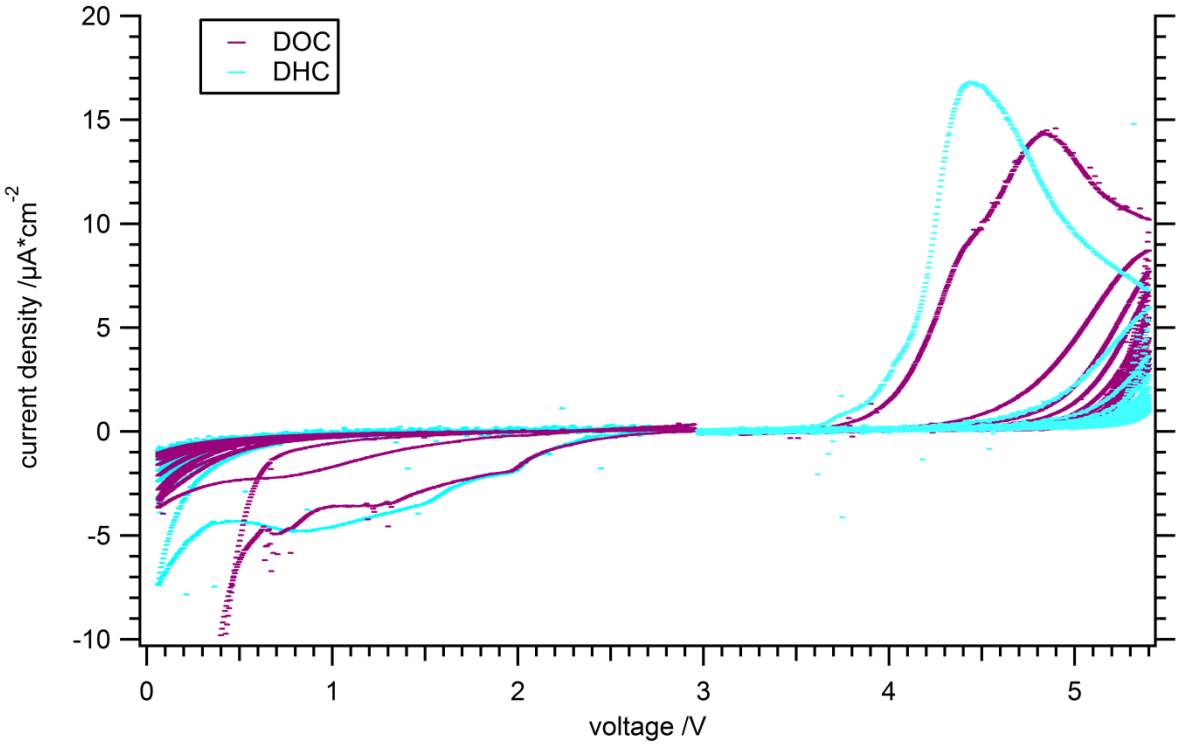

Fig. 30: Cyclic voltammogramms for the linear electrolytes DHC (blue) and DOC (purple). Both electrolytes are highly efficient in forming a stable SEI during reduction and oxidation.

In Fig. 30, the cyclic voltamograms of the linear electrolytes DHC and DOC are shown. As mentioned previously, these electrolytes were least resistant to oxidative decomposition above 4 V. Surprisingly, however, both electrolytes rapidly formed a stable SEI and eventually became more resistant to oxidation than any other electrolyte. In comparison, DHC is even more promising than DOC, resisting oxidation until 5.0 V after three cycles and 5.2 V after 10 cycles. Moreover, DHC is equally efficient during reduction, starting at 2.0 – 2.5 V in the first cycle and at <0.5 V in subsequent cycles.

The first and the tenth oxidative and reductive cycle for DHC and LP30, respectively, are compared in Fig. 31. While DHC is less stable in the first cycle both during oxidation and reduction, the current density is greatly reduced after ten cycles. As the conductivity of DHC is presumably too low to allow its use as a bulk electrolyte, it might be useful as an additive for 5 V class batteries. In this context, its low stability during the first cycle is advantageous, as this facilitates preferential incorporation into the SEI. However, its ability to form a stable SEI on a real electrode surface has yet to be proven.

:

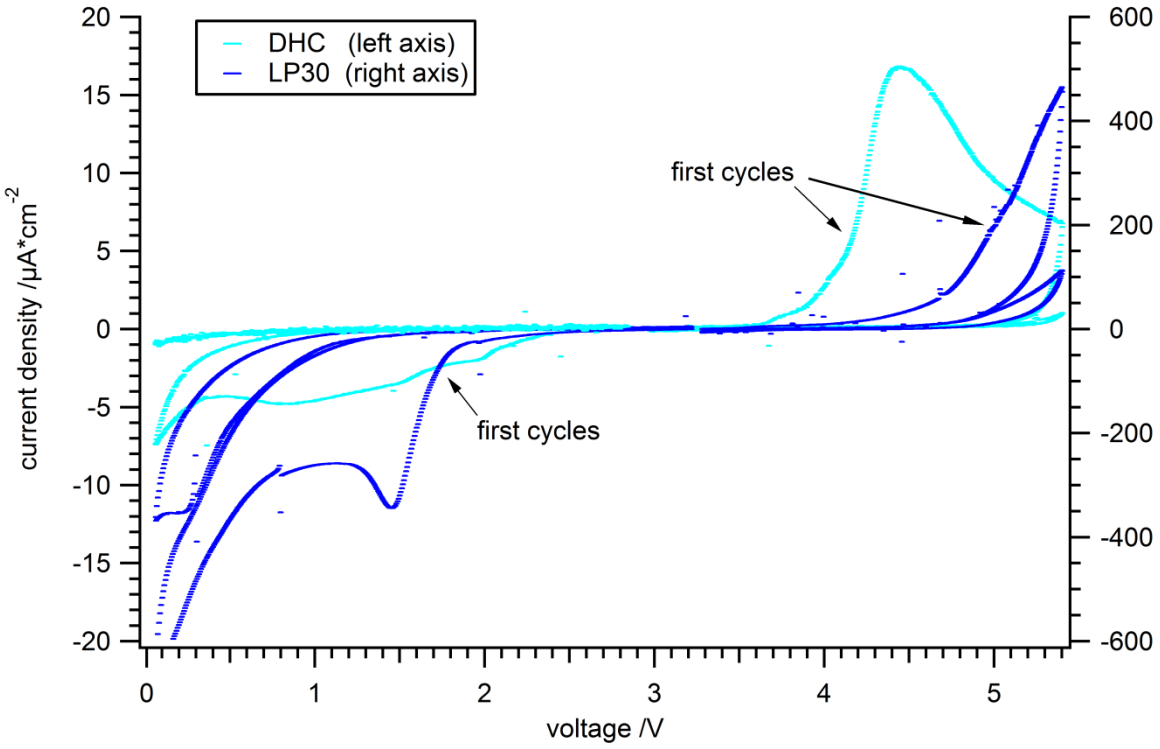

Fig. 31: First and tenth oxidative and reductive cycle for DHC (left axis) and LP30 (right axis).

3.2.3 Galvanostatic cycling

Finally, self-manufactured electrodes and electrolytes were incorporated in Swagelok cells with lithium counter and reference electrodes. As galvanostatic cycling with potential limitation (GCPL) measurements at low C rates are time consuming, they were conducted in parallel to the electrolyte characterization and stability testing. While this precludes a targeted approach, the first cells were aimed mainly at reproducing literature results and ensuring reproducibility as well as getting first impressions of how the new electrolytes may influence cycling behavior. I tried the electrolytes for two different anode materials which pose different challenges onto the passivation layer albeit operating at similar voltages. Firstly, graphite was employed where cointercalation of solvent must be precluded. Second, a Sn/C composite material that acts as a test piece for an anode material where the active material undergoes volume changes during cycling. The introduction of longer alkyl chains into the SEI components is aimed at forming a possibly more flexible SEI than what is forming from standard electrolytes.

The first cells included two 10 µm Celgard polypropylene films as separators so as to minimize the consumption of the synthesized electrolytes. However, those separators resulted in several short circuits or contact losses during the GCPL measurements. Therefore, thicker Whatman glass microfiber separators superseded Celgard films, eliminating the aforementioned problems.

First, the cells were assembled containing graphite electrodes and a standard EC/DMC electrolyte. The results for those two cells are shown in Fig. 32 (blue lines). Specific capacities are sometimes higher than the theoretical maximum, owing to an underestimation of the actual active material weight (see below). Additionally, one cell showed irreversible capacities for each cycle and significant capacity fading over 100 cycles was observed for both cells.

Those issues also apply to cells with a HC/PC 4/1 (v/v) electrolyte intended to reproduce the results obtained by Ross.[89] Ross employed this mixture to prevent exfoliation of graphite caused by co-intercalation of PC and achieved high coulombic efficiencies and a stable capacity of 300 mAh/g after 10 cycles. In contrast, my cells showed a rather low efficiency and significant capacity fading although at a similar capacity level. One reason for capacity fading could be that Ross' electrodes were compressed to achieve a lower porosity which increases cyclabiliy. As expected, pure HC performs extremely poorly due to massive irreversible capacities of more than 1500 mAh/g in the first cycle.

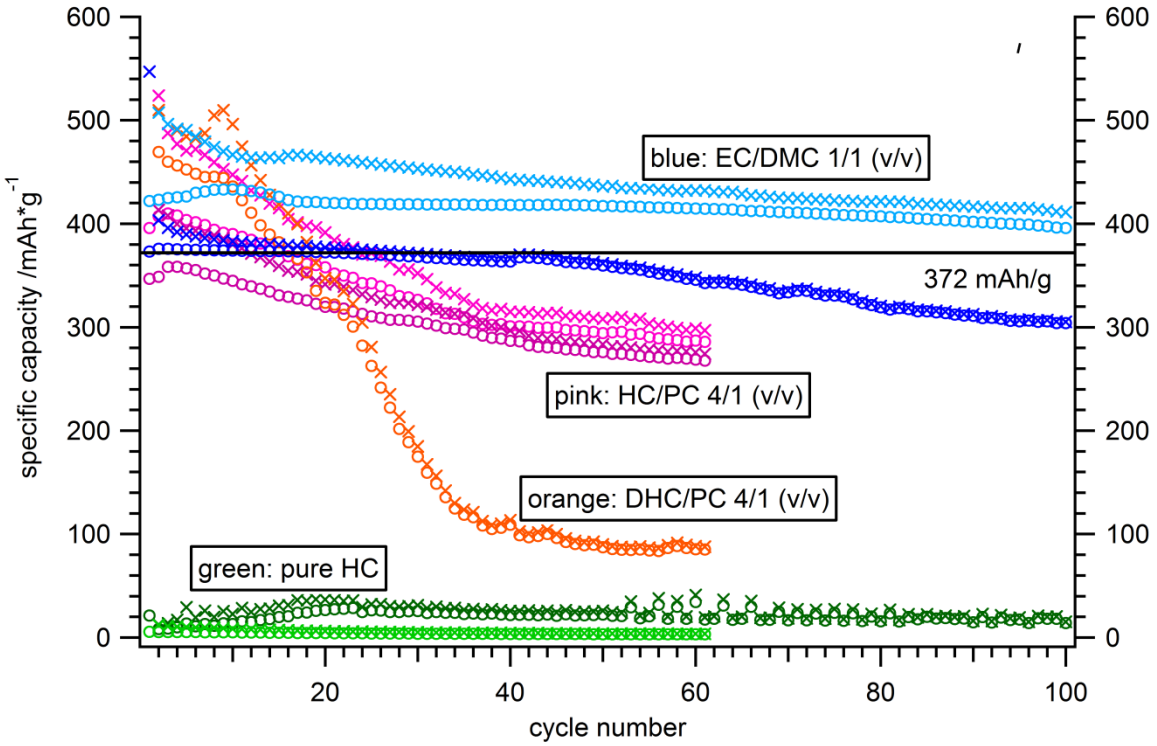

Fig. 32: GCPL at 0.1 C rates of cells containing graphite electrodes and electrolytes with a 1 mol/L concentration of $LiPF_6$. Crosses mark cathodic capacities, circles anodic capacities. The horizontal line marks the theoretical capacity for graphite.

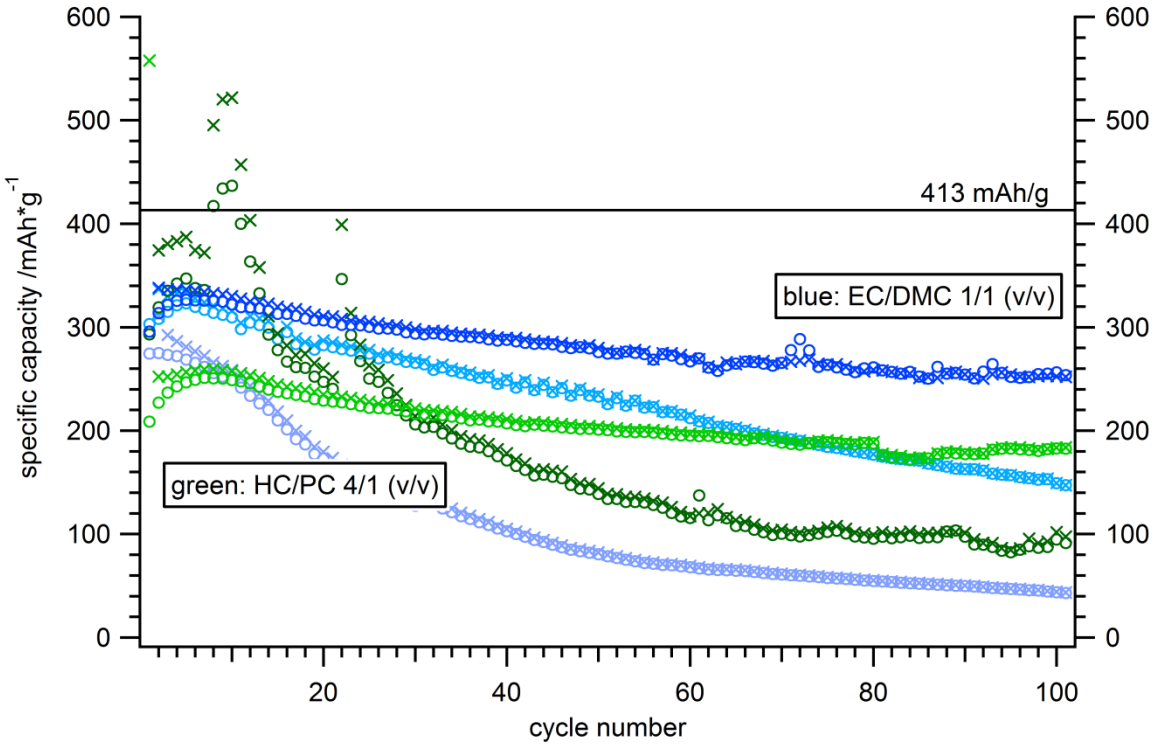

Fig. 33: GCPL at 0.24 C rates of cells containing Sn-C electrodes and varying electrolyte mixtures with 1 mol/L $LiPF_6$. Crosses mark cathodic capacities, rings anodic capacities. The horizontal line marks the theoretical capacity for the Sn/C composite.

For the Sn/C electrodes, coulombic efficiencies were higher, but capacity fading and low capacities in general remained problematic. Interestingly, HC/PC mixtures seem to perform similar to EC/DMC for Sn/C electrodes. Large irreversible capacities in the first cycle are characteristic for this type of anodes and were also observed in my measurements (see Table 5).[90] The values match those by Scrosati and were remarkably similar for both electrolytes, indicating that electrolyte decomposition is not confined to EC or DMC.

Table 5: Irreversible capacities in the first cycle for Sn/C electrodes and EC/DMC 1/1 (v/v) and HC/PC 4/1 (v/v) electrolytes with 1 mol/L $LiPF_6$, respectively.

EC/DMC /%	HC/PC /%
63.7	62.6
60.4	64.3
58.7	

In general, however, both reproducibility and performance of the so far assembled Swagelok cells were unsatisfactory. One serious limitation to high reproducibility is the fact that it is impossible to precisely determine the mass of electrode material on the working electrode. Only the total mass comprising electrode material and the copper current collector can be measured, but their contributions cannot be separated for the particular sample. Therefore, I attempted to obtain the average weight of the current collector by punching out 13 blanks from the untreated copper foil, the average mass of which was 12.63±0.06 mg. This value was subtracted from the total mass, leading to an average active material mass of 0.8±0.1 mg. The standard deviation might be low in absolute numbers, but amounts to 13 % in relative numbers.

Additionally, this method features an inherent error. The mass fluctuation of the current collector is not considered. According to this calculation, a high total mass is due to a high amount of active material. In fact, however, the high total mass could also originate from an unusually heavy current collector. In this case, the amount of active material is overestimated resulting in a low perceived specific capacity. Unfortunately, this problem also extends to the Sn/C electrodes punched from the films of Dr. Hassoun. He used a thicker copper foil (23.0±0.3 mg) and a higher electrode loading, resulting in an average active material mass of 3.2±0.5. Nevertheless, the relative standard deviation of 14 % is remarkably similar to that of the graphite electrodes.

Reducing the fluctuation of blank masses would be a way to alleviate this error, for example by employing a more precise punching device. Alternately, it might be more accurate to establish an average electrode loading from larger copper blanks and an equally large piece of coated film. Then the average loading would be applied to all electrodes cut from the respective piece of film. Due to the higher absolute masses, the average loading could be determined with a smaller relative error. This method, however, relies on a reproducible way to cut a large, defined area.

The second important source of error is cell assembly. Various possible mistakes during fabrication could result in untight cells, contact loss, short circuits and capacity fading. It is assumed, that such mistakes can be avoided with increasing proficiency.

4 Conclusion and Outlook

In the present work, a small library of lithium and sodium alkyl (di)carbonates was synthesized and analyzed with respect to thermal stability and decomposition, molecular arrangement and ionic conductivity. Combined DSC/TGA-MS measurements suggest that thermal degradation proceeds via one or more endothermic processes, the major mass losses occurring well above the operating temperature of Li-ion cells. Organic residues and CO_2 are emitted, while the inorganic metal carbonate remains as main decomposition product.

Our results show that bilayered structures are indeed formed by long chained alkyl carbonates, with the measured interlayer distances found to be in good agreement with the estimated spacing. However, layered structures do not significantly enhance ionic diffusion on a macroscopic scale. In fact, the highest conductivities were observed for the most disordered phases formed by alkyl dicarbonates, followed by the crystalline short-chained alkyl carbonates. Further investigations by ^{6}Li and ^{7}Li solid state NMR will focus on the question whether lithium diffusion is higher on a molecular level and the low overall conductivity is due to increased diffusion distance caused by tortuous pathways or the lower volume available to diffusion.

Furthermore, facile synthetic routes were employed to obtain corresponding cyclic and linear carbonate-based electrolytes in high, albeit not absolute, purity. The electrochemical stability window with $LiPF_6$ was comparable to a mixture of EC and DMC. DHC passivated the glassy carbon electrode up to a potential of 5V within three cycles and retained superior stability after ten cycles. Due to its initially lower resistance to oxidation, it could be an efficient additive for high voltage cathodes. Future testing should disclose DHC's performance on real electrodes and in combination with common electrolyte mixtures so as to better estimate its potential.

Future work should focus on deeper understanding of a more extended set of "designed" SEI components such as alkoxides with respect to ion mobility, structure, mechanical properties, and stability. Ultimately, we want to arrive at improved electrolytes for Li and Na based batteries that address the shortcomings of current electrolytes for the emerging materials. These include alloying and conversion anodes and high voltage cathodes with Li and all types of materials with Na. For the latter no standard electrolyte has emerged unlike for Li-intercalation batteries. While the solvents polarity and donor properties are essential to dissolve salts to allow ion transport, the very same qualities cause problematic interactions with many active materials or constituents of the SEI. Thereby inspired, a class of bi-functional molecules shall be investigated that allows tailoring polar and non-polar portions according to the battery chemistry's requirements. Moreover viscosity and local arrangement can be affected this way with possible beneficial effects for conductivity or interaction with active material as discussed below. The general building principle is to covalently bond immiscible polar and non-polar portions into a molecule. Polar groups may be carbonates, ethers and sulfones and the apolar groups may be drawn from (halogenated) alkanes or dimethylsiloxoanes linked linearly or branched. Foremost the work needs to be underpinned by a comprehensive set of (in-situ) spectroscopy to understand the behavior in the working environment.

5 Experimental Part

5.1 Synthesis

5.1.1 Chemicals

Chemicals were generally purchased from Sigma-Aldrich, Merck, Alfa Aesar, ACBR and Fluka and were -unless stated differently - used as received. Carbon dioxide (CO_2) with a purity >99,995% and <5 ppm H_2O was obtained from Messer.

The concentration of *n*-Butyllithium (BuLi) in hexane was determined by titration with *sec*-Butanol employing 1,10-Phenanthroline as indicator. Sodium hydride was stored as a dispersion (60 %) in mineral oil, washed with pentane (3x) and dried *in vacuo* prior to use. Lithium and sodium metal were opened and stored in the glove box and the oxide layer was removed by scratching before usage.

Cyclohexane (CH) was distilled to remove impurities. Dry dichloromethane (DCM) was obtained by distillation over P_2O_5, dry diethyl ether by passing over an aluminum oxide column. Dry hexane and acetonitrile (MeCN) containing very low amounts of water were purchased from Sigma-Aldrich and opened exclusively in the glove box. All dry solvents were stored at least one day over molecular sieves that had been activated at 200 °C in high vacuum before being used.

Alcohols for the synthesis of decomposition products were refluxed and distilled over lithium metal under an inert atmosphere or vacuum and subsequently stored over molecular sieves in the glove box for at least one day. The water content determined by Karl-Fischer-titration was in the range of 20 ppm.

5.1.2 Analytical methods

Silica-gel plates from Merck (silicagel 60 F_{254}) were used for thin layer chromatography. The spots were detected using an UV lamp, or employing a potassium permanganate or cerium ammonium molybdate (CAM) dipping solution. Potassium permanganate solution was prepared by dissolving 1 wt% $KMnO_4$ in distilled water (dH_2O). CAM was obtained by adding a 10 wt% solution of $(NH_3)_3MO_4.4H_2O$ in H_2SO_4 (10 %) to a solution of 10 w% cerium(IV)-sulfate in H_2SO_4 (10%) in a ratio of 12.5 to 1 (v/v).

NMR was performed using an Avance III 300 spectrometer with auto sampler with 300 MHz for ^{1}H- and 75 MHz for ^{13}C-spectra, respectively. Deuterated chloroform ($CDCl_3$) and water (D_2O) were employed as solvents, with their residual peaks at 7.26 ($CDCl_3$, ^{1}H), 77.16 ($CDCl_3$, ^{13}C) and 4.79 ppm (D_2O, ^{1}H) serving as reference for chemical shifts.

With the help of Yuhui Chen from the University of St. Andrews, moisture sensitive decomposition products were characterized by Fourier FTIR. FTIR spectra were collected on a Nicolet 6700 spectrometer (Thermo Fisher Scientific) located in a N_2-filled glovebox using a resolution of 4 cm^{-1} from 4000 to 225 cm^{-1}. A small amount of powder was ground with ~0.1 g of dried CsI. The resulting fine powder was then compressed into a transparent pellet by a die-set press.

5.1.3 Synthesis of SEI components

As all synthesized SEI components were susceptible to moisture, all preparations and purification steps requiring an open reaction vessel were performed in an Ar-filled glove box containing <1 ppm H_2O. Obviously, this does not hold true for the precursors, whose synthesis included deionized water as solvent.

5.1.3.1 General procedure for the synthesis of lithium and sodium alkyl carbonates

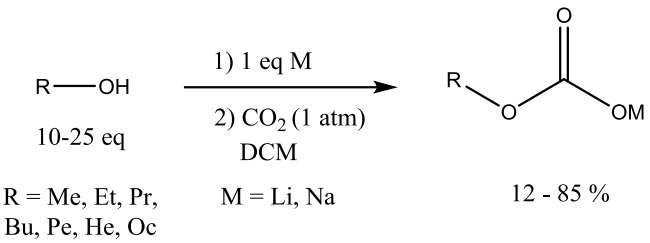

In a 100 mL Schott bottle, the alkali metal (1.0 eq) was dissolved in dry alcohol (10-25 eq) and subsequently diluted with 10 mL DCM. CO_2 was generated by the evaporation of dry ice or the reaction of aqueous 1.8 M K_2CO_3 with 10 M H_2SO_4 and dried by flowing through a cooling trap (-40 °C) and a $CaCl_2$ filled tube. As the dry gas was flushed through the vigorously stirred suspension, a colorless precipitate started to form almost immediately.

After 45 minutes, the cap was reinstated in the glove box and the solvent was removed by centrifugation and subsequent decanting of the supernatant. The crude product was then washed by suspending it in 10 mL DCM, centrifugation and decanting (2x) and dried *in vacuo* at room temperature (RT).

Table 6: Equivalents employed and yields achieved for the synthesis of lithium and sodium alkyl carbonates.

product	eq alcohol	yield /g	yield /%	product	eq alcohol	yield /g	yield /%
LMC	25	0.524	36	NMC	25	1.24	67
LEC	15	0.18	12	NEC	15	1.25	70
LPrC	10	1.11	63	NPrC	10	1.48	74
LBC	10	0.41	30	NBC	10	0.93	61
LPC	10	0.73	52	NPC	10	1.33	85
LHC	10	1.15	78	NHC	10	0.99	56
LOC	10	0.91	88	NOC	10	1.55	83

5.1.3.2 LS 3: 1,2-Butandiol

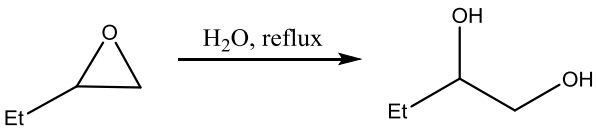

In a 1 L round bottomed flask (RBF) mounted with a reflux condenser, 1,2-Epoxybutane (6.201 g, 86 mmol) was dissolved in 550 mL dH_2O and refluxed for 15 h. Then, the mixture was cooled to RT and the solvent removed *in vacuo*.

yield = 7.72 g (>99%) colorless liquid

^{1}H-NMR (D_2O, 25 °C, 300 MHz): δ (ppm) = 3.67-3.54 (m, 2H, C*H*(OH)C*H*$_2$OH), 3.53-3.41 (q, 1H, C*H*$_2$OH), 1.60-1.32 (m, 2H, C*H*$_2$), 0.96-0.87 (t, 3H, $^{3}J_{HH}$=7.8 Hz, C*H*$_3$).

^{13}C{^{1}H}-NMR ($CDCl_3$, 25 °C, 75 MHz):): δ (ppm) = 73.9 (1C, *C*H), 66.3 (1C, *C*H$_2$OH), 26.2 (1C, *C*H$_2$), 10.0 (1C, *C*H$_3$).

5.1.3.3 LS 7: 1,2-Hexanediol

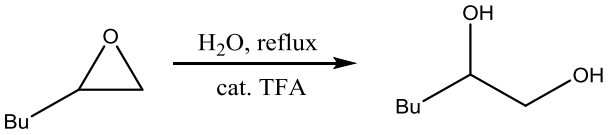

In a 500 mL RBF with a reflux condenser, 1,2-Epoxyhexane (3.005 g, 30 mmol) was added to 210 mL dH_2O with three drops of trifluoracetic acid and refluxed until TLC indicated full conversion (20 h). Subsequently, the mixture was cooled to RT and the solvent was removed *in vacuo*.

yield = 3.32 g (94%) colorless liquid

^{1}H-NMR ($CDCl_3$, 25 °C, 300 MHz): δ (ppm) = 3.75-3.61 (m, 2H, C*H*(OH)C*H*$_2$OH), 3.49-3.37 (q, 1H, C*H*$_2$OH), 1.50-1.25 (m, 6H, C*H*$_2$), 0.95-0.85 (t, 3H, $^{3}J_{HH}$=6.7 Hz, C*H*$_3$).

^{13}C{^{1}H}-NMR ($CDCl_3$, 25 °C, 75 MHz):): δ (ppm) = 72.5 (1C, *C*H), 66.9 (1C, *C*H$_2$OH), 32.9, 27.9, 22.8 (3C, *C*H$_2$), 14.1 (1C, *C*H$_3$).

5.1.3.4 LS 4: 1,2-Dodecanediol

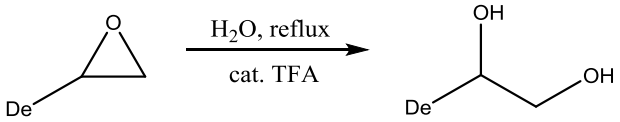

1,2-Epoxydodecane (6.144g, 30 mmol) was added to a mixture of 220 mL dH_2O and a few drops of trifluoracetic acid in a 500 mL RBF with condenser and heated until TLC showed full consumption of educt (5 d). After cooling the mixture to RT and removing the solvent in vacuo, the crude product was purified by flash column chromatography (CH/EA 2/1 to 1/2 (v/v)).

yield = 2.20 g (35%) colorless solid

^{1}H-NMR ($CDCl_3$, 25 °C, 300 MHz): δ (ppm) = 3.76-3.61 (m, 2H, C*H*(OH)C*H*$_2$OH), 3.49-3.38 (q, 1H, C*H*$_2$OH), 2.1-1.8 (bs, 2H, O*H*) 1.50-1.18 (m, 18H, C*H*$_2$), 0.94-0.82 (t, 3H, $^{3}J_{HH}$=6.5 Hz, C*H*$_3$).

^{13}C{^{1}H}-NMR ($CDCl_3$, 25 °C, 75 MHz):): δ (ppm) = 72.5 (1C, *C*H), 67.0 (1C, *C*H$_2$OH), 33.3, 32.0, 29.8, 29.8, 29.8, 29.7, 29.5, 25.7, 22.8 (9C, *C*H$_2$), 14.2 (1C, *C*H$_3$).

5.1.3.5 Synthesis of lithium alkyl dicarbonates

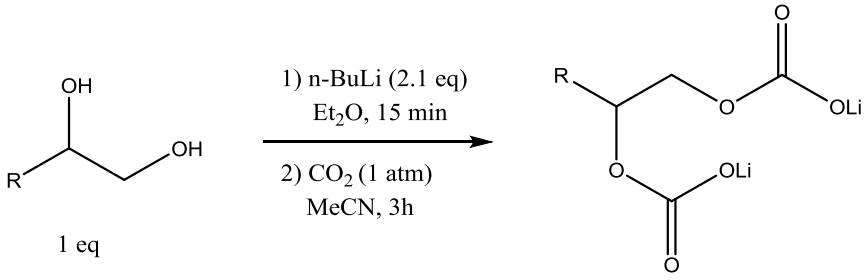

1,2-Diol (4-6 mmol, 1 eq) in 2-4 g Et_2O was added drop wise to a vigorously stirred solution of BuLi (2.1 eq) in 4g Et_2O in a 50 mL Schott flask, forming a colorless precipitate. The suspension was stirred for 15 min, centrifuged and the supernatant decanted. Subsequently the solid was suspended in 15 mL hexane, centrifuged and decanted again (2x) to remove remaining BuLi.

Then the solid was suspended in 15 mL MeCN and CO_2 was flushed through the reaction vessel for 3 h. The solvent was removed by centrifugation and subsequent decantation, washed with MeCN (2x, as with hexane) and dried over night at RT *in vacuo*.

LS-11: 1,2-Lithium butyl dicarbonate: yield = 0.91 g (82%) colorless solid

LS-12: 1,2-Lithium hexyl dicarbonate: yield = 1.26 g (98%) colorless solid

LS-13: 1,2-Lithium dodecyl dicarbonate: yield = 1.05 g (88%) colorless solid

5.1.3.6 Synthesis of sodium alkyl dicarbonates

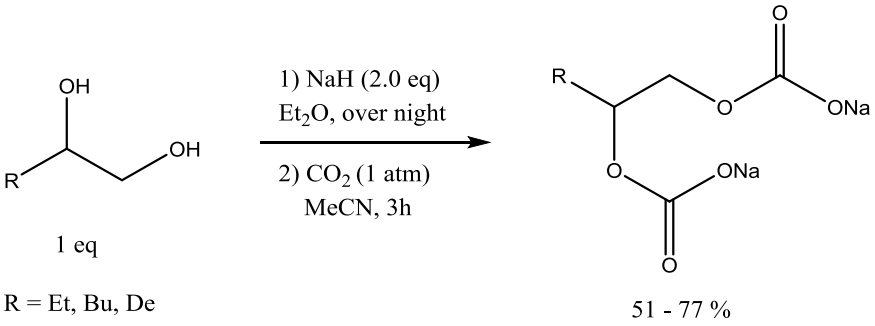

1,2-Diol (3-5 mmol, 1 eq) in 3-10 mL Et_2O was added drop wise to a vigorously stirred suspension of sodium hydride (2 eq) in 10 g Et_2O. The reaction mixture was left to react over night. Then, the solvent was replaced with 10 mL MeCN and held under a CO_2 atmosphere for 3h. The resulting moist solid was suspended in MeCN, centrifuged and the supernatant decanted (3x).

LS-14: 1,2-Sodium butyl dicarbonate: yield = 0.62 g (62%) colorless solid

LS- 16: 1,2-Sodium hexyl dicarbonate: yield = 0.51 g (51%) colorless solid

LS-17: 1,2-Sodium dodecyl dicarbonate: yield = 0.77 g (77%) colorless solid

5.1.4 Synthesis of electrolytes

When the reactions required inert conditions, classical Schlenk techniques were used. Flasks were evacuated, heated up and flushed with N_2 three times prior to use. After purification and drying, the electrolytes were transferred directly to the glove box and stored over molecular sieves.

5.1.4.1 Cyclic carbonates

5.1.4.1.1 LS 5: Triphenylphosphine hydroiodide

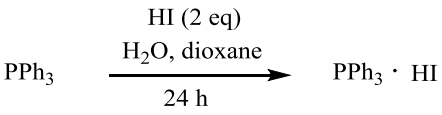

In a 50 mL RBF, triphenylphosphine (2.107 g, 8 mmol, 1 eq) was dissolved in 16 mL 1,4-dioxane, forming a yellowish solution. Subsequently, 2.1 mL of a 58% hydrogen iodide solution in water (3.53 g, 16 mmol, 2 eq) was added slowly drop wise, instantly resulting in a colorless precipitate. After stirring at RT for 24 h, the solvent was removed in vacuo and the crude product was washed with Et_2O (6 x). The resulting pale yellow solid was dried in high vacuum at 40 °C for 6 h.

yield = 2.968 g (95%) pale yellow solid

^{1}H-NMR ($CDCl_3$, 25 °C, 300 MHz): δ (ppm) = 7.65-7.48 (m, 15H, ArH).

$^{13}C\{^1H\}$-NMR ($CDCl_3$, 25 °C, 75 MHz):): δ (ppm) = 135.3, 135.3, 134.2, 134.1, 130.6, 130.4 (15C, ArC), 117.1, 116.0 (3C, C_q).

5.1.4.1.2 LS 6: Butylene carbonate

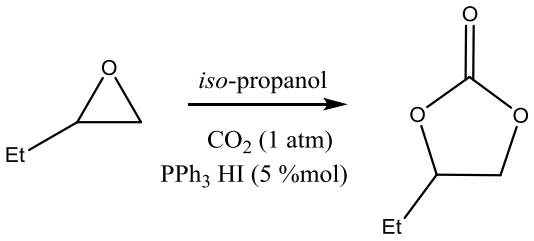

52 %

In a 100 mL three necked RBF equipped with a CO_2 balloon, a gas/vacuum inlet and a stopper, 1,2-epoxybutane (5.770 g, 80 mmol, 1 eq) was dissolved in 20 mL isopropanol. After addition of triphenyphosphine hydroiodide (1.560 g, 4 mmol, 0.05 eq) , the vacuum valve was opened shortly, closed again and followed by opening the CO_2 inlet (2x) to saturate the reaction atmosphere with CO_2.

The reaction mixture was stirred for 2 d at 45 °C, then the solvent was removed in vacuo and the crude product purified by Silica gel filtration (DCM) and subsequent vacuum distillation (head temperature 76-78 °C).

yield = 3.651 (52%) colorless liquid

^{1}H-NMR ($CDCl_3$, 25 °C, 300 MHz): δ (ppm) = 4.71-4.59 (quint., 1H, $^3J_{HH}$=6.8 Hz, C*H*), 4.55-4.47 (t, 1H, $^3J_{HH}$=8.1 Hz, CH_2O), 4.11-4.02 (t, 1H, $^3J_{HH}$=7.7 Hz, CH_2O), 1.87-1.65 (m, 2H, CH_2), 1.05-0.96 (t, 3H, $^3J_{HH}$=7.4 Hz).

$^{13}C\{^{1}H\}$-NMR ($CDCl_3$, 25 °C, 75 MHz):): δ (ppm) = 155.2 (1C, C_q), 78.1 (1C, *C*H), 69.1 (1C, CH*C*H_2), 26.9 (1C, *C*H_2CH$_3$), 8.4 (1C, *C*H_3).

5.1.4.1.3 LS 9: Hexylene carbonate

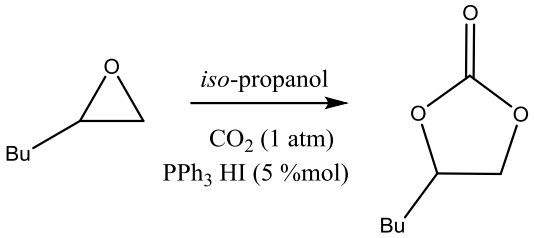

41 %

In a 100 mL three necked RBF with a CO_2 balloon, a gas/vacuum inlet and a stopper, 1,2-epoxyhexane (10.020 g, 100 mmol, 1 eq) and triphenylphosphine hydroiodide (1.95 g, 5 mmol, 0.05 eq) were added to 25 mL isopropanol. Then, the atmosphere inside the flask was saturated with CO_2 by shortly opening the vacuum inlet and subsequent opening of the CO_2 inlet.

After stirring the reaction mixture 3 d at 45 °C, the catalyst was removed by silica gel filtration (DCM) and the solvent removed in vacuo. The crude product was purified by column chromatography (CH/EA 15/1 (v/v)). Finally, the product was obtained by vacuum distillation (head temperature 103-105 °C).

yield = 5.805 g (41%) colorless liquid

^{1}H-NMR ($CDCl_3$, 25 °C, 300 MHz): δ (ppm) = 4.76-4.64 (quint., 1H, $^{3}J_{HH}$=7.0 Hz, C*H*), 4.57-4.48 (t, 1H, ^{3}J=8.1 Hz, CH_2O), 4.11-4.02 (t, 1H, $^{3}J_{HH}$=7.8 Hz, CH_2O), 1.89-1.61 (m, 2H, CH_2CH), 1.52-1.29 (m, 4H, CH_2), 0.98-0.87 (t, 3H, $^{3}J_{HH}$=6.9 Hz).

$^{13}C\{^{1}H\}$-NMR ($CDCl_3$, 25 °C, 75 MHz):): δ (ppm) = 155.2 (1C, C_q), 77.2 (1C, *C*H), 69.5 (1C, CH*C*H_2), 33.7, 26.6, 22.4 (3C, *C*H_2), 13.9 (1C, *C*H_3).

5.1.4.1.4 LS 10: Dodecylene carbonate

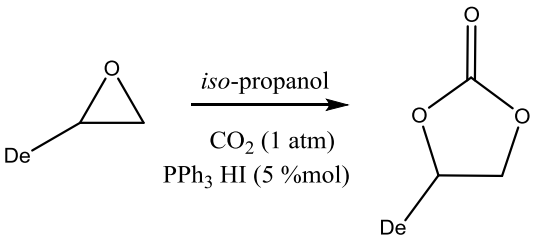

59 %

In a 100 mL Schlenk flask, 1,2-epoxydodecane (10.240 g, 50 mmol, 1 eq) and triphenylphosphine hydroiodide (0.975 g, 2.5 mmol, 0.05 eq). The reaction atmosphere was saturated with CO_2 by shortly opening the vacuum inlet and then the CO_2 inlet (2x).

The colorless solution was stirred for 3 d at 45°C, then the liquid was filtered through Silica gel (DCM), the solvent removed and the crude product purified by flash column chromatography (CH/EA 15/1 (v/v) to pure EA).

yield = 6.026 g (59%) colorless oil

^{1}H-NMR ($CDCl_3$, 25 °C, 300 MHz): δ (ppm) = 4.76-4.63 (quint., 1H, $^{3}J_{HH}$=7.0 Hz, C*H*), 4.56-4.47 (t, 1H, $^{3}J_{HH}$=8.1 Hz, CH_2O), 4.11-4.01 (t, 1H, $^{3}J_{HH}$=7.8 Hz, CH_2O), 1.89-1.59 (m, 2H, CH_2CH), 1.55-1.19 (m, 16H, CH_2), 0.92-0.82 (t, 3H, $^{3}J_{HH}$=6.5 Hz).

^{13}C{^{1}H}-NMR ($CDCl_3$, 25 °C, 75 MHz):): δ (ppm) = 69.5 (1C, *C*H_2O), 34.1 (1C, *C*H_2CH), 32.0, 29.7, 29.6, 29.5, 29.3, 27.1, 24.5, 22.8 (8C, *C*H_2), 14.2 (1*C*, CH_3).

5.1.4.2 Linear Carbonates

5.1.4.2.1 Synthesis of dialkyl carbonates

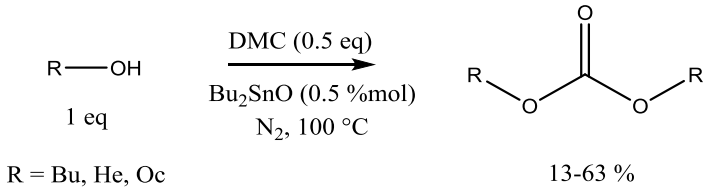

R = Bu, He, Oc

13-63 %

A three necked RBF with gas/vacuum inlet was evacuated and flushed with N_2 (3x). Under N_2-stream, the stopper was replaced with a condenser with a bubbler. Dibutyl tin oxide (0.005 eq) and alcohol (50-70 mmol, 1 eq) were added and the resulting suspension heated to 100 °C until the catalyst was completely dissolved. Subsequently, diethyl carbonate was added drop wise through a septum and the solution was heated to 110 °C for 1 d.

Then, the yellowish mixture was taken up in 50 mL DCM, washed with dH_2O (3x 30 mL) and the aqueous phase re-extracted with DCM (3x20 mL).The combined organic phase was dried over Na_2SO_4 and the solvent removed in vacuo. The crude product was purified by flash column chromatography (CH/EA 10/1 (v/v)) and vacuum distillation (head temperature 95-98 °C) for dioctyl and dihexyl carbonate, respectively.

LS-18: Dihexyl carbonate: yield = 2.06 g (13%) colorless liquid

^{1}H-NMR ($CDCl_3$, 25 °C, 300 MHz): δ (ppm) = 4.15-4.08 (t, 4H, $^{3}J_{HH}$=6.7 Hz, CH_2O), 1.72-1.60 (quint., 4H, $^{3}J_{HH}$=7.1, CH_2CH_2O), 1.44-1.22 (m, 12H, CH_2), 0.95-0.82 (t, 6H, $^{3}J_{HH}$=6.6, CH_3).

^{13}C{^{1}H}-NMR ($CDCl_3$, 25 °C, 75 MHz):): δ (ppm) = 155.6 (1C, C_q), 68.2 (2C, *C*H_2O), 31.6, 28.8, 25.5, 22.7 (8C, *C*H_2), 14.1 (2C, *C*H_3).

LS-15: Diocytl carbonate: yield = 4.52 g (63%) colorless liquid

^{1}H-NMR ($CDCl_3$, 25 °C, 300 MHz): δ (ppm) = 4.16-4.07 (t, 4H, $^{3}J_{HH}$=6.7 Hz, CH_2O), 1.72-1.59 (quint., 4H, $^{3}J_{HH}$=7.0, CH_2CH_2O), 1.44-1.19 (m, 20H, CH_2), 0.93-0.82 (t, 6H, $^{3}J_{HH}$=6.2, CH_3).

^{13}C{^{1}H}-NMR ($CDCl_3$, 25 °C, 75 MHz):): δ (ppm) = 155.6 (1C, C_q), 68.2 (2C, *C*H_2O), 31.9, 29.3, 29.3, 28.8, 25.9, 22.8 (12C, *C*H_2), 14.2 (2C, *C*H_3).

5.1.4.2.2 LS-19: Dibutyl carbonate

Dibutyltin oxide (0.398 g, 1.6 mmol, 0.02 eq) was suspended in Butanol (14.46 mL, 160 mmol, 2 eq) in a dry three necked RBF with gas/vacuum inlet. Under nitrogen stream, a stopper was replaced with a reflux condenser with bubbler and the mixture was heated to 110 °C until the dibutyltin oxide was completely dissolved. Subsequently, dimethyl carbonate was added drop wise through a septum. The solution was heated to 110 °C for 1d, then the temperature was raised to 150 °C over 4h.

Then the reaction mixture was cooled to RT, taken up in 90 mL DCM, washed with dH_2O (3x 90 mL), dried over Na_2SO_4 and the solvent was removed under reduced pressure. The crude product was purified by vacuum distillation (head temperature 44-46 °C).

yield = 6.46 g (46%) colorless liquid

^{1}H-NMR ($CDCl_3$, 25 °C, 300 MHz): δ (ppm) = 4.16-4.07 (t, 4H, $^3J_{HH}$=6.6 Hz, C*H*$_2$O), 1.71-1.57 (quint., 4H, $^3J_{HH}$=7.0, C*H*$_2$CH$_2$O), 1.47-1.31 (quint., 4H, $^3J_{HH}$=9.3, C*H*$_2$), 0.97-0.88 (t, 6H, $^3J_{HH}$=7.3, C*H*$_3$).

^{13}C{^{1}H}-NMR ($CDCl_3$, 25 °C, 75 MHz):): δ (ppm) = 155.6 (1C, C_q), 67.8 (2C, *C*H$_2$O), 30.8, 19.1 (4C, *C*H$_2$), 13.8 (2C, *C*H$_3$).

5.2 Characterization of SEI components

5.2.1 Differential Scanning Calorimetry/Thermogravimetry with Mass Spectrometry

In a glove box, 2 to 3 mg of the respective product was placed in a DSC-vial with an Indium metal sealing. Indiums melts at 157 °C, thus allowing gaseous decomposition products to be analyzed by MS-spectroscopy while preventing preliminary contamination with moisture. DSC and TGA measurements were simultaneously conducted in a Netzsch STA 449 C Jupiter instrument. The temperature program is depicted in Fig. 34, the ramping rate was 10 °C/min. With a helium stream evolving decomposition products were carried to the Netzsch QMS 403 C Aeolus mass spectrometer and analyzed in a m/z range of 15 to 200.

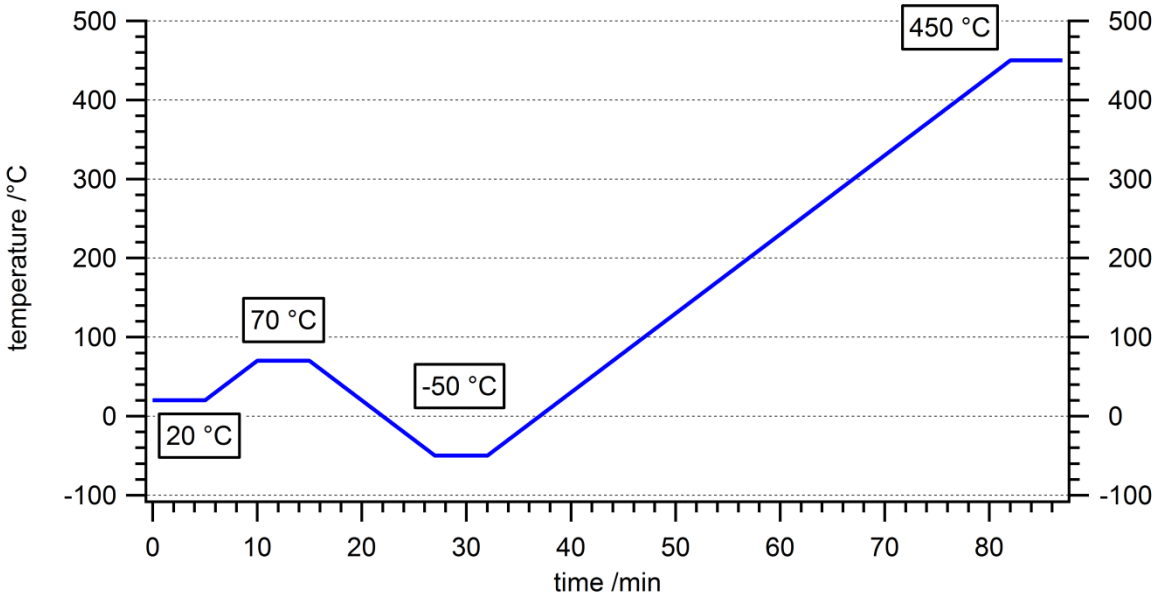

Fig. 34: Temperature program for the DSC/TGA-MS measurements with plateau temperatures. The ramping rate is 10 °C/min.

5.2.2 Small Angle X-Ray Scattering

SAXS measurements were recorded with a high-flux SAXSess camera linked to a Debyeflex 3003 X-ray generator. The CuK$_\alpha$ radiation beam (0.154 nm) was generated at 40 kV and 50 mA in a sealed-tube Cu anode, focused and collimated using a Goebel-mirror and a Kratky-slit, respectively, to a line shape of 17 mm horizontal dimension at the sample. Scattered radiation was measured in transmission mode in a q-range of 0.1 to 6 nm^{-1}. According to eq. 13

$$q = \frac{4\pi * \sin\theta}{\lambda} \tag{13}$$

with q being the magnitude of the scattering vector, 2 θ the scattering angle and λ the wavelength, the 2θ range is 1.4 ° to 8.4 °. All samples were filled into 1.5 mm diameter glass capillaries and sealed with silicon rubber in the glove box. Outside the box, the samples were flame-sealed and measured at 20 °C under vacuum (2 mbar) with an exposure time of 100 s each.

5.2.3 Powder X-Ray Diffraction

XRD patterns were collected with an Empyrian reflectometer. CuK_{α} radition (0.154 nm) was provided from a sealed tube operating at 40 kV and 40 mA. The beam was passed through 10 mm and 1/8 inch slits and then through sample mounted parallel to the beam. The diffracted intensities were recorded with a PixCel 3D detector equipped with a 7.5 mm anti-scatter slit. The detector was moved from a 2θ angle of 4.51 ° to 50.0 ° with a step size of 10^{-4}. Samples were prepared in the same way as SAXS samples.

Full width at half maximum (FWHM) values were calculated using IgorPro 6.34's built-in Multi Peak Fit package. A linear baseline was added in proximity to a solitary peak, which was subsequently fitted to a Voigt or experimentally modified Gauss function. Generally, the maximum residues were at roughly 5 % of the respective peak height.

5.2.4 Electrochmical impedance spectroscopy

Pellets of the SEI components with a diameter of 7 mm were pressed by applying a pressure of 500 kg for 10 min followed by 1000 kg for 15 min. A Braun MB EVAP high vacuum coating plant connected to a SQM 160 coating thickness measurement device was used for vacuum deposition of a roughly 100 nm conducting gold layer on both sides of the pellets. Subsequently, the pellets were embodied in an air-tight aluminum pouch with an insulating coating on the outside and copper current collectors. Hitherto, all manipulations were performed in the glove box.

EIS measurements were conducted using a Novocontrol broadband dielectric/impedance spectrometer with an Alpha A high performance frequency analyzer in a range from 10^{7} to 10^{-2} Hz. The respective temperatures for each measurement are depicted in Fig. 35, with a minimal equilibration time of 240 s. The first samples were subjected to program 1, which was eventually replaced with program 2 to generate more data points at elevated temperatures. Subsequently, the pouch cells were opened to determine the sample tablet's thickness and calculate the correct stray factor.

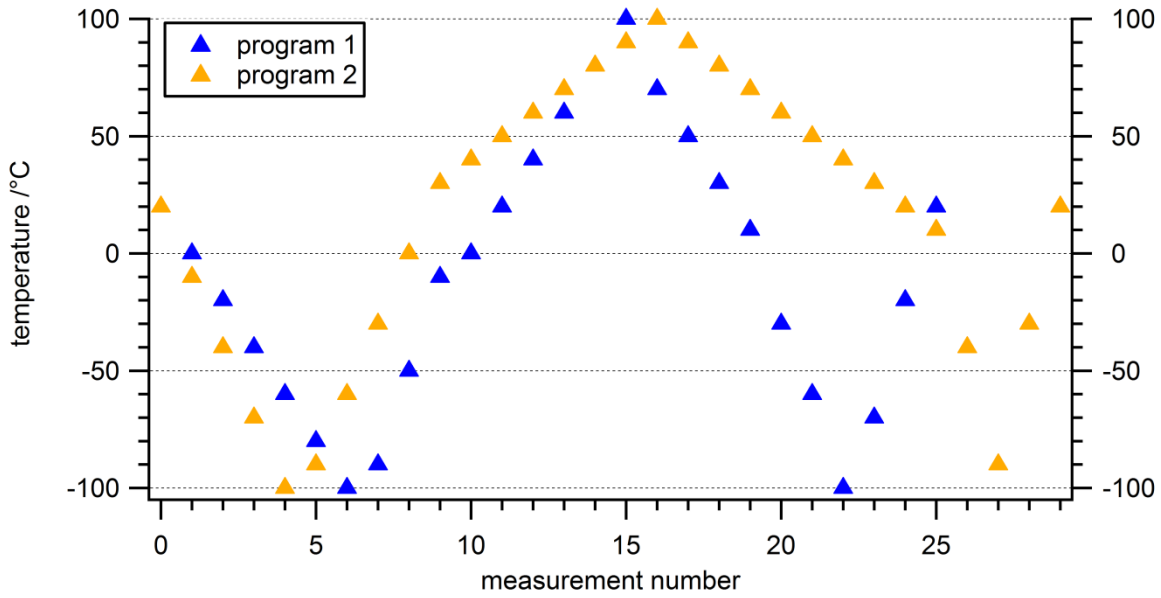

Fig. 35: Temperature programs for EIS measurements. Program 1 was used for the first measurements and later replaced with program 2 to generate more data at high temperatures.

5.3 Preliminary electrolyte testing

5.3.1 Linear sweep- and cyclic voltammetry

The electrochemical stability of the prepared electrolytes was assessed by linear sweep voltammetry at a $LiPF_6$ concentration of 0.2, 0.4 and – if feasible - 1.0 mol/L, respectively, in an N_2-filled glove box. A Zahner Elektrik IM6 electrochemical workstation and a corresponding U-Buffer to extend the voltage range up to 10 V were employed. The slew rate was set to 1 mV/s and the voltage limits to 0.05 and 5.4 V for reductive and oxidative sweeps, respectively.

The working electrode consisted of glassy carbon, the counter and reference electrodes of metallic lithium in a steel syringe tip. The latter ones were replaced as they darkened due to oxidation or reaction with nitrogen, while the first one was polished and dried after each measurement.

Cyclic voltammetry was conducted to study the formation of a protective layer on the glassy carbon working electrode. The electrolytes were cycled between open circuit potential and 0.05 and 5.4 V, respectively, with a slew rate of 1 mV/s in a system described above. The concentrations were 1.0 mol/L, except for DC, DOC and DHC which were studied at 0.7 mol/L.

5.3.2 Galvanostatic Cycling with Potential Limitation

5.3.2.1 Preparation of graphite electrodes

For the fabrication of the utilized graphite electrodes, 104 mg polymer binder (Kynar, polyvinyliden fluoride, ARKEMA) was added to 5.5 mL *N*-methylpyrollidone (NMP) and stirred until complete dissolution (30 min). Subsequently, 105 mg conductive additive (Super C65, conductive carbon black, Imerys Timcal C-NERGY) and 830 mg graphite active material (KS 6L, Imerys Timcal C-NERGY) were suspended in the mixture and remaining particles were washed from the vial wall with another 0.7 mL NMP. The resulting slurry was stirred for 24 h at 600 rpm.

Then the slurry was cast on a roughened copper foil (Goodfellow Cambridge Limited, 99.9%, thickness 18 µm) using an Erichsen Coatmaster 510 automatic film applicator. The casting blade moved at a speed of 10 mm/s, the gap width being 100 µm.

After drying the film at 60 °C over night, several electrodes with a diameter of 10 mm were punched and dried in a Büchi glass oven at 60 °C for at least 12 h. The individual electrodes were weighed on a analytical balance (Mettler Toledo XA20DU), dried again under identical conditions and transferred to a glove box.

Additionally, 13 pieces of 10 mm Cu-foil were punched and weighed, resulting in an average mass of 12.63±0.06 mg. This value was subtracted from every electrode's weight to determine the amount of film material on an electrode, 80% of which are active graphite. In average, the active material amounts to 0.8±0.1 mg.

5.3.2.2 Preparation of Sn-C electrodes

A cast film on Cu-foil featuring tin in a carbon matrix was received from Jusef Hassoun from the University of Rome Sapienza. The active Sn-C material, with a tin content of 35% as estimated by TGA, amounts to 80% of the film. Additives include a polymer binder (polyvinyliden fluoride 6020, Solvay, 10%) and a conductive agent (SP, carbon black, Timcal, 10%).

The following steps of cutting, drying, and weighing are identical to those described above. The average blank mass was calculated from 5 blanks to be 23.0±0.3 mg. The average electrode mass was 26.2±0.5 mg, resulting in an electrode loading of 3.2±0.5 mg. Interestingly, however, Mr. Hassoun assumed an electrode loading of only 2.6 mg.

5.3.2.3 Cell assembly and measurement

Testing cells were assembled in the glove box in a three electrode configuration with a graphite or Sn-C working electrode and Li foil as reference and counter electrode, respectively, using a PFA-220-3 Swagelok tube fitting. The electrodes were separated by two polypropylene foils (2400-1200 E-A, Celgard, 10 µm thickness). As this resulted in several short circuited cells, superseding cells comprised a thicker glass microfiber separator (Whatman, GF/B, GE Healthcare Life Sciences).

Reference cells were built to ensure that the cells give results similar to the literature. For those cells, LP30 (EC/DMC 1/1, 1 M $LiPF_6$), LP 40 (ED/DEC 1/1, 1 M $LiPF_6$; both from BASF, HF <50 ppm, H_2O < 20 ppm) served as electrolytes for Sn-C and graphite working electrodes, respectively. Self-synthesized electrolytes were employed in testing cells with graphite or Sn-C electrodes either pure or as a mixture with propylene carbonate (PC, Sigma-Aldrich, anhydrous 99.7 %) with 1 M $LiPF_6$ in any case.

GCPL measurements were conducted either in a Bio-Logic VMP3 Potentiostat/Galvanostat/EIS or in a Bio-Logic MPG-2 battery test station. After 12 h resting time, graphite cells were cycled 60-100 times at a 0.1 C rate between 0.05 and 2V. Sn-C cells were likewise allowed to equilibrate for 12 h and subsequently cycled 60-100 times at a 0.24 C rate between 0.01 and 2V.

6 Appendix

6.1 Literature

1. Gachot, G. *et al.* Deciphering the multi-step degradation mechanisms of carbonate-based electrolyte in Li batteries. *J. Power Sources* **178,** 409–421 (2008).

2. Xu, K., von Cresce, A. & Lee, U. Differentiating contributions to “ion transfer” barrier from interphasial resistance and Li+ desolvation at electrolyte/graphite interface. *Langmuir* **26,** 11538–43 (2010).

3. Borodin, O. & Bedrov, D. Interfacial Structure and Dynamics of the Lithium Alkyl Dicarbonate SEI Components in Contact with the Lithium Battery Electrolyte. *J. Phys. Chem. C* **118,** 18362–18371 (2014).

4. Borodin, O., Zhuang, G. V., Ross, P. N. & Xu, K. Molecular Dynamics Simulations and Experimental Study of Lithium Ion Transport in Dilithium Ethylene Dicarbonate. *J. Phys. Chem. C* **117,** 7433–7444 (2013).

5. Kishimoto, K. *et al.* Nano-segregated polymeric film exhibiting high ionic conductivities. *J. Am. Chem. Soc.* **127,** 15618–15623 (2005).

6. Reddy, T. *Linden’s Handbook of Batteries, 4th Edition*. *Amazon* 1200 (2010).

7. Xu, K. Electrolytes and interphases in li-ion batteries and beyond. *Chem Rev* **114,** 11503–11618 (2014).

8. Aurbach, D., Zinigrad, E., Cohen, Y. & Teller, H. A short review of failure mechanisms of lithium metal and lithiated graphite anodes in liquid electrolyte solutions. *Solid State Ionics* **148,** 405–416 (2002).

9. Besenhard, J. O. & Daniel, C. *Handbook of Battery Materials*. (Wiley-VCH, 2011).

10. Tran, T. D., Feikert, J. H., Song, X. & Kinoshita, K. Commercial Carbonaceous Materials as Lithium Intercalation Anodes. *J. Electrochem. Soc.* **142,** 3297–3302 (1995).

11. Song, X. Y., Kinoshita, K. & Tran, T. D. Microstructural characterization of lithiated graphite. *J. Electrochem. Soc.* **143,** L120–L123 (1996).

12. Akimoto, J., Gotoh, Y. & Oosawa, Y. Synthesis and structure refinement of LiCoO2 single crystals. *J. Solid State Chem.* **141,** 298–302 (1998).

13. Tukamoto, H. & West, A. Electronic conductivity of LiCoO2 and its enhancement by magnesium doping. *J. Electrochem. Soc.* **144,** 3164–3168 (1997).

14. Korthauer, R. *Handbuch Lithium-Ionen-Batterien*. (Springer Vieweg, 2013). doi:10.1007/978-3-642-30653-2

15. Venkatraman, S., Shin, Y. & Manthiram, A. Phase relationships and structural and chemical stabilities of charged Li1-xCoO2-delta and Li1-xNi0.85Co0.15O2-delta cathodes. *Electrochem. Solid State Lett.* **6,** A9–A12 (2003).

16. Molenda, J. & Marzec, J. FUNCTIONAL CATHODE MATERIALS FOR Li-ION BATTERIES — PART III: POTENTIAL CATHODE MATERIALS LixNi1-y-zCoyMnzO2 AND LiMn2O4. *Funct. Mater. Lett.* **02,** 1 (2009).

17. Islam, M. S. & Fisher, C. a J. Lithium and sodium battery cathode materials: computational insights into voltage, diffusion and nanostructural properties. *Chem. Soc. Rev.* **43,** 185–204 (2014).

18. Ellis, B. L., Lee, K. T. & Nazar, L. F. Positive Electrode Materials for Li-Ion and Li-Batteries †. *Chem. Mater.* **22,** 691–714 (2010).

19. Hunter, J. C. Preparation of a new crystal form of manganese dioxide: λ-MnO2. *J. Solid State Chem.* **39,** 142–147 (1981).

20. Xia, Y. *et al.* Improved cycling performance of oxygen-stoichiometric spinel Li1+xAlyMn2−x−yO4+δ at elevated temperature. *Electrochim. Acta* **52,** 4708–4714 (2007).

21. Islam, M. S., Driscoll, D. J., Fisher, C. A. J. & Slater, P. R. Atomic-Scale Investigation of Defects, Dopants, and Lithium Transport in the LiFePO4 Olivine-Type Battery Material. *Chem. Mater.* **17,** 5085–5092 (2005).

22. Kang, B. & Ceder, G. Battery materials for ultrafast charging and discharging. *Nature* **458,** 190–193 (2009).

23. Goodenough, J. B. & Kim, Y. Challenges for rechargeable batteries. *J. Power Sources* **196,** 6688–6694 (2011).

24. Zugmann, S. Messung von Lithium-Ionen Überführungszahlen an Elektrolyten für Lithium-Ionen Batterien-Eine vergleichende Studie mit fünf verschiedenen Methoden. (2011). at <http://epub.uni-regensburg.de/20968>

25. Deepa, M., Agnihotry, S. A., Gupta, D. & Chandra, R. Ion-pairing effects and ion-solvent-polymer interactions in LiN(CF 3SO2)2-PC-PMMA electrolytes: A FTIR study. *Electrochim. Acta* **49,** 373–383 (2004).

26. Burba, C. M. & Frech, R. Spectroscopic measurements of ionic association in solutions of LiPF 6. *J. Phys. Chem. B* **109,** 15161–15164 (2005).

27. Bogle, X., Vazquez, R., Greenbaum, S., Cresce, A. von W. & Xu, K. Understanding Li + –Solvent Interaction in Nonaqueous Carbonate Electrolytes with 17 O NMR. *J. Phys. Chem. Lett.* **4,** 1664–1668 (2013).

28. Von Cresce, A. & Xu, K. Preferential Solvation of Li+ Directs Formation of Interphase on Graphitic Anode. *Electrochemical and Solid-State Letters* **14,** A154 (2011).

29. Winter, M. The Solid Electrolyte Interphase – The Most Important and the Least Understood Solid Electrolyte in Rechargeable Li Batteries. *Zeitschrift für Phys. Chemie* **223,** 1395–1406 (2009).

30. Besenhard, J. O., Winter, M., Yang, J. & Biberacher, W. Filming mechanism of lithium-carbon anodes in organic and inorganic electrolytes. *J. Power Sources* **54,** 228–231 (1995).

31. Wagner, M. R., Albering, J. H., Moeller, K. C., Besenhard, J. O. & Winter, M. XRD evidence for the electrochemical formation of Li+(PC) yCn - in PC-based electrolytes. *Electrochem. commun.* **7,** 947–952 (2005).

32. Spahr, M. E. *et al.* Exfoliation of Graphite during Electrochemical Lithium Insertion in Ethylene Carbonate-Containing Electrolytes. *J. Electrochem. Soc.* **151 ,** A1383–A1395 (2004).

33. Smith, A. J., Burns, J. C., Zhao, X., Xiong, D. & Dahn, J. R. A High Precision Coulometry Study of the SEI Growth in Li/Graphite Cells. *J. Electrochem. Soc.* **158 ,** A447–A452 (2011).

34. Von Wald Cresce, A., Borodin, O. & Xu, K. Correlating Li+ solvation sheath structure with interphasial chemistry on graphite. *J. Phys. Chem. C* **116,** 26111–26117 (2012).

35. Aurbach, D. *et al.* Recent studies of the lithium-liquid electrolyte interface Electrochemical, morphological and spectral studies of a few important systems. *J. Power Sources* **54,** 76–84 (1995).

36. Augustsson, A. *et al.* Solid electrolyte interphase on graphite Li-ion battery anodes studied by soft X-ray spectroscopy. *Physical Chemistry Chemical Physics* **6,** 4185 (2004).

37. Zhao, L., Watanabe, I., Doi, T., Okada, S. & Yamaki, J. TG-MS analysis of solid electrolyte interphase (SEI) on graphite negative-electrode in lithium-ion batteries. *J. Power Sources* **161,** 1275–1280 (2006).

38. Broussely, M. *et al.* Main aging mechanisms in Li ion batteries. in *Journal of Power Sources* **146,** 90–96 (2005).

39. Philippe, B. *et al.* Improved performances of nanosilicon electrodes using the salt LiFSI: A photoelectron spectroscopy study. *J. Am. Chem. Soc.* **135,** 9829–9842 (2013).

40. Dedryvère, R. *et al.* XPS valence characterization of lithium salts as a tool to study electrode/electrolyte interfaces of Li-ion batteries. *J. Phys. Chem. B* **110,** 12986–12992 (2006).

41. Harilal, S. S., Allain, J. P., Hassanein, A., Hendricks, M. R. & Nieto-Perez, M. Reactivity of lithium exposed graphite surface. *Appl. Surf. Sci.* **255,** 8539–8543 (2009).

42. Lu, P. & Harris, S. J. Lithium transport within the solid electrolyte interphase. *Electrochem. commun.* **13,** 1035–1037 (2011).

43. Shi, S. *et al.* Direct calculation of Li-ion transport in the solid electrolyte interphase. *J. Am. Chem. Soc.* **134,** 15476–87 (2012).

44. Edström, K., Gustafsson, T. & Thomas, J. O. The cathode-electrolyte interface in the Li-ion battery. in *Electrochimica Acta* **50,** 397–403 (2004).

45. Dupré, N. *et al.* Aging of the LiNi1⁄2Mn1⁄2O2 Positive Electrode Interface in Electrolyte. *J. Electrochem. Soc.* **156,** C180–C185 (2009).

46. Wang, Z., Sun, Y., Chen, L. & Huang, X. Electrochemical Characterization of Positive Electrode Material LiNi1 / 3Co1 / 3Mn1 / 3 O 2 and Compatibility with Electrolyte for Lithium-Ion Batteries . *J. Electrochem. Soc.* **151 ,** A914–A921 (2004).

47. Wang, Z., Huang, X. & Chen, L. Characterization of Spontaneous Reactions of LiCoO2 with Electrolyte Solvent for Lithium-Ion Batteries . *J. Electrochem. Soc.* **151 ,** A1641–A1652 (2004).

48. Liu, N., Li, H., Wang, Z., Huang, X. & Chen, L. Origin of Solid Electrolyte Interphase on Nanosized LiCoO2 . *Electrochem. Solid-State Lett.* **9 ,** A328–A331 (2006).

49. Aurbach, D. *et al.* Review on electrode-electrolyte solution interactions, related to cathode materials for Li-ion batteries. *Journal of Power Sources* **165,** 491–499 (2007).

50. Yang, L., Ravdel, B. & Lucht, B. L. Electrolyte Reactions with the Surface of High Voltage LiNi0.5Mn1.5O4 Cathodes for Lithium-Ion Batteries. *Electrochem. Solid-State Lett.* **13,** A95 (2010).

51. Whittingham, M. S. Ultimate Limits to Intercalation Reactions for Lithium Batteries. *Chem. Rev.* **114,** 11414–11443 (2014).

52. Islam, M. S. *et al.* Silicate cathodes for lithium batteries: alternatives to phosphates? *J. Mater. Chem.* **21,** 9811–9818 (2011).

53. Hu, M., Pang, X. & Zhou, Z. Recent progress in high-voltage lithium ion batteries. *J. Power Sources* **237,** 229–242 (2013).

54. Wang, H., Tan, T. A., Yang, P., Lai, M. O. & Lu, L. High-Rate Performances of the Ru-Doped Spinel LiNi0.5Mn1.5O4: Effects of Doping and Particle Size. *J. Phys. Chem. C* **115,** 6102–6110 (2011).

55. Jung, H.-G., Jang, M. W., Hassoun, J., Sun, Y. & Scrosati, B. A high-rate long-life Li4Ti5O12 / Li[Ni0.45Co0.1Mn1.45]O4 lithium-ion battery. *Nat. Commun.* **2,** 515–516 (2011).

56. Liu, D., Lu, Y. & Goodenough, J. B. Rate Properties and Elevated-Temperature Performances of LiNi0.5 − x Cr2x Mn1.5 − x O4 (0 ≤ 2x ≤ 0.8) as 5 V Cathode Materials for Lithium-Ion Batteries. *J. Electrochem. Soc.* **157 ,** A1269–A1273 (2010).

57. Lu, Z. & Dahn, J. R. Understanding the Anomalous Capacity of Li /Li[NixLi(1/3−2x/3)Mn(2/3−x/3)]O2Cells Using In Situ X-Ray Diffraction and Electrochemical Studies. *J. Electrochem. Soc.* **149,** A815–A822 (2002).

58. Amine, K., Yasuda, H. & Yamachi, M. Olivine LiCoPO4 as 4.8 V electrode material for lithium batteries. *Electrochem. Solid State Lett.* **3,** 178–179 (2000).

59. Han, D.-W., Kang, Y.-M., Yin, R.-Z., Song, M.-S. & Kwon, H.-S. Effects of Fe doping on the electrochemical performance of LiCoPO4/C composites for high power-density cathode materials. *Electrochem. commun.* **11,** 137–140 (2009).

60. Liu, J. *et al.* Spherical nanoporous LiCoPO4/C composites as high performance cathode materials for rechargeable lithium-ion batteries. *J. Mater. Chem.* **21,** 9984 (2011).

61. Liu, J. & Manthiram, A. Understanding the Improvement in the Electrochemical Properties of Surface Modified 5 V LiMn1.42Ni0.42Co0.16O4 Spinel Cathodes in Lithium-ion Cells. *Chem. Mater.* **21,** 1695–1707 (2009).

62. Kang, S.-H. & Thackeray, M. M. Stabilization of xLi2MnO3*(1-x)LiMO2 Electrode Surfaces(M = Mn, Ni, Co) with Mildly Acidic, Fluorinated Solutions. *J. Electrochem. Soc.* **155,** A269–A275 (2008).

63. Xu, K. & von Cresce, A. Interfacing electrolytes with electrodes in Li ion batteries. *Journal of Materials Chemistry* **21,** 9849 (2011).

64. Wang, Z. *et al.* Effect of glutaric anhydride additive on the LiNi 0.4Mn 1.6O 4 electrode/electrolyte interface evolution: A MAS NMR and TEM/EELS study. *J. Power Sources* **215,** 170–178 (2012).

65. Xu, M., Lu, D., Garsuch, A. & Lucht, B. L. Improved Performance of LiNi0.5Mn1.5O4 Cathodes with Electrolytes Containing Dimethylmethylphosphonate (DMMP). *Journal of the Electrochemical Society* **159,** A2130–A2134 (2012).

66. Yang, L. & Lucht, B. L. Inhibition of Electrolyte Oxidation in Lithium Ion Batteries with Electrolyte Additives. *Electrochemical and Solid-State Letters* **12,** A229 (2009).

67. Arbizzani, C. *et al.* Use of non-conventional electrolyte salt and additives in high-voltage graphite/LiNi0.4Mn1.6O4 batteries. *J. Power Sources* **238,** 17–20 (2013).

68. Carboni, M., Spezia, R. & Brutti, S. Perfluoroalkyl-Fluorophosphate Anions for High Voltage Electrolytes in Lithium Cells: DFT Study. *J. Phys. Chem. C* **118,** 24221–24230 (2014).

69. Jin, J. *et al.* Li/LiFePO4 batteries with room temperature ionic liquid as electrolyte. *Electrochem. commun.* **11,** 1500–1503 (2009).

70. Watanabe, Y. *et al.* Electrochemical properties and lithium ion solvation behavior of sulfone–ester mixed electrolytes for high-voltage rechargeable lithium cells. *J. Power Sources* **179,** 770–779 (2008).

71. Zhu, Y., Casselman, M. D., Li, Y., Wei, A. & Abraham, D. P. Perfluoroalkyl-substituted ethylene carbonates: Novel electrolyte additives for high-voltage lithium-ion batteries. *J. Power Sources* **246,** 184–191 (2014).

72. Obrovac, M. N. & Christensen, L. Structural Changes in Silicon Anodes during Lithium Insertion/Extraction. *Electrochemical and Solid-State Letters* **7,** A93 (2004).

73. Courtney, I. A., Tse, J. S., Mao, O., Hafner, J. & Dahn, J. R. Ab initio calculation of the lithium-tin voltage profile. *Phys. Rev. B* **58,** 15583–15588 (1998).

74. Goward, G. R., Taylor, N. J., Souza, D. C. S. & Nazar, L. F. The true crystal structure of Li17M4 (M=Ge, Sn, Pb)-revised from Li22M5. *J. Alloys Compd.* **329,** 82–91 (2001).

75. Obrovac, M. N. & Chevrier, V. L. Alloy negative electrodes for li-ion batteries. *Chem. Rev.* **114,** 11444–502 (2014).

76. Li, H., Balaya, P. & Maier, J. Li-Storage via Heterogeneous Reaction in Selected Binary Metal Fluorides and Oxides. *J. Electrochem. Soc.* **151,** A1878 (2004).

77. Cabana, J., Monconduit, L., Larcher, D. & Palacín, M. R. Beyond intercalation-based Li-ion batteries: the state of the art and challenges of electrode materials reacting through conversion reactions. *Adv. Mater.* **22,** E170–92 (2010).

78. Doe, R. E., Persson, K. A., Meng, Y. S. & Ceder, G. First-principles investigation of the Li-Fe-F phase diagram and equilibrium and nonequilibrium conversion reactions of iron fluorides with lithium. *Chem. Mater.* **20,** 5274–5283 (2008).

79. Oumellal, Y., Rougier, A., Nazri, G. A., Tarascon, J.-M. & Aymard, L. Metal hydrides for lithium-ion batteries. *Nat. Mater.* **7,** 916–921 (2008).

80. Palacín, M. R. Recent advances in rechargeable battery materials: a chemist's perspective. *Chem. Soc. Rev.* **38,** 2565–75 (2009).

81. Li, J., Le, D. B., Ferguson, P. P. & Dahn, J. R. Lithium polyacrylate as a binder for tin-cobalt-carbon negative electrodes in lithium-ion batteries. *Electrochim. Acta* **55,** 2991–2995 (2010).

82. Aurbach, D. Review of selected electrode – solution interactions which determine the performance of Li and Li ion batteries. *J. Power Sources* **89,** 206–218 (2000).

83. Choi, N. S. *et al.* Effect of fluoroethylene carbonate additive on interfacial properties of silicon thin-film electrode. *J. Power Sources* **161,** 1254–1259 (2006).

84. Lee, Y. M., Lee, J. Y., Shim, H.-T., Lee, J. K. & Park, J.-K. SEI Layer Formation on Amorphous Si Thin Electrode during Precycling. *J. Electrochem. Soc.* **154 ,** A515–A519 (2007).

85. Dalavi, S., Guduru, P. & Lucht, B. L. Performance Enhancing Electrolyte Additives for Lithium Ion Batteries with Silicon Anodes. *J. Electrochem. Soc.* **159 ,** A642–A646 (2012).

86. Zhuang, G. V., Yang, H., Ross, P. N., Xu, K. & Jow, T. R. Lithium Methyl Carbonate as a Reaction Product of Metallic Lithium and Dimethyl Carbonate. *Electrochem. Solid-State Lett.* **9,** A64–A68 (2006).

87. Xu, K. *et al.* Syntheses and characterization of lithium alkyl mono- and dicarbonates as components of surface films in Li-ion batteries. *J. Phys. Chem. B* **110,** 7708–19 (2006).

88. Borodin, O., Smith, G. D. & Fan, P. Molecular dynamics simulations of lithium alkyl carbonates. *J. Phys. Chem. B* **110,** 22773–9 (2006).

89. Zhao, H. *et al.* Propylene Carbonate (PC)-Based Electrolytes with High Coulombic Efficiency for Lithium-Ion Batteries. *J. Electrochem. Soc.* **161,** A194–A200 (2013).

90. Hassoun, J., Lee, K.-S., Sun, Y.-K. & Scrosati, B. An advanced lithium ion battery based on high performance electrode materials. *J. Am. Chem. Soc.* **133,** 3139–43 (2011).

6.2 List of Figures

Fig. 1: Overview of the synthesized SEI components (left) that might form lamellar structures allowing 2D ionic diffusion. 9
Fig. 2: Main structural classes of positive electrode materials: (a) Layered oxide structure of $LiMO_2$ (M=Co, Ni, Mn), (b) cubic $LiMn_2O_4$ spinel and (c) olivine $LiMPO_4$ (M=Fe, Co, Ni). Lithium ions are shown in green, octahedral CoO_6 in blue, MnO_6 in purple, FeO polyhedral in brown and PO_4 tetrahedra in lavender. Figure taken from ref. 13. 12
Fig. 3: Schematic energy diagram of a lithium ion battery at open circuit. Redox potentials of anode (E_a) and cathode (E_c) are within the stability window of the electrolyte (E_g). 13
Fig. 4: The typical voltage hysteresis of a conversion material, depicted in a voltage vs. composition diagram. Figure taken from ref 68. 19
Fig. 5: FTIR spectra of all lithium carbonates from LMC (bottom) to LOC (top). Li_2CO_3 is depicted as reference (blue line). The offset between the baselines is 0.2. 20
Fig. 6: FTIR-spectra of lithium dicarbonates from LBDC (bottom) to LDDC (top). Li_2CO_3 is depicted as reference (blue line). The offset between the baselines is 0.2. 21
Fig. 7: FTIR spectra of all sodium carbonates from NMC (bottom) to NOC (top). The offset between the baselines is 0.3. 22
Fig. 8: FTIR-spectra of sodium dicarbonates from NBDC (bottom) to NDDC (top). The offset between the baselines is 0.4. 22
Fig. 9: Decomposition temperatures for lithium and sodium alkyl carbonates (filled) and –dicarbonates (empty triangles). 24
Fig. 10: Exemplary DSC (lines) and TGA (dashed lines, secondary axis) data for LMC, LPrC and LOC. The melting of the indium sealing causes the sharp peak at 157 °C. 26
Fig. 11: Exemplary DSC (lines) and TGA (dashed lines, secondary axis) data for NMC and NOC. NMC melts in a single, sharp decomposition step with only one endothermic peak, whereas NOC shows several smaller peaks. 26
Fig. 12: The residual mass of all lithium- and sodium alkyl carbonates (triangles) is compared to the residual mass if the single decomposition products were alkali metal carbonates (lines) or alkali metal alkoxides (dashed lines). Apparently, inorganic carbonates are the predominant residues for higher homolgues. 27
Fig. 13: SAXS patterns of lithium alkyl carbonates. Tags annotate the scattering vector of each peak and the corresponding interlayer distances. 28
Fig. 14: PXRD patterns (2Θ CuK_α) of lithium alkyl carbonates. LEC strongly resembles Li_2CO_3. 29
Fig. 15: SAXS patterns of sodium alkyl carbonates. Interlayer distances are higher than for the lithium analogues. 29
Fig. 16: PXRD patterns (2Θ CuK_α) of sodium alkyl carbonates. 29
Fig. 17 SAXS patterns of sodium alkyl dicarbonates. NHDC and NDDC exhibit likely an intergrowth of two different lattices with different spacing. 30
Fig. 18: XRD patterns of sodium (left) and lithium alkyl dicarbonate (right). LEC is added to the right figure for comparison. 31
Fig. 19: Exemplary EIS data for LMC. The colors represent temperatures ranging from -100 °C (purple) to 100 °C (red). LMC displays direct current plateaus at elevated temperatures. 33
Fig. 20: AC Conductivities for lithium alkyl monocarbonates at 20 and 100 °C drop with increasing chain length. LMC, LEC and LBC exhibit constant current plateaus at 100 °C. 34

Fig. 21: Arrhenius plots of LMC (left) and LEC (right). The values obtained in the heating process differ from the cooling process for LMC, but not for LEC. 35
Fig. 22: AC conductivities for sodium alkyl carbonates with increasing chain lengths. Neither chain length nor structure correlate with conductivities. 35
Fig. 23: Direct current conductivities for sodium alkyl dicarbonates at 20 °C (left, filled) and 100 °C (right, striped)..... 36
Fig. 24: Arrhenius plots of NBDC (left) and NHDC (right). Both samples show increased conductivity and lower activation energies during cooling. 37
Fig. 25: AC conductivities of lithium alkyl dicarbonates at 20 and 100 °C drop with increasing chain lengths, although differences between LHDC and LDDC are small..... 37
Fig. 26: Arrhenius plot for the first measurement of LDDC, showing a sharp bend at roughly 50 °C. The inset shows DSC and TG curves, with a significant endothermic peak at 48.7 °C indicating a phase change or a chemical reaction not related to decomposition. 38
Fig. 27: Overview of the synthesized electrolytes and the respective abbreviations. 39
Fig. 28: Linear sweeps in oxidative and reductive direction at 1 mV/s for BC, HC, DC, DHC and DOC (from top left to bottom right). Darker colors show higher $LiPF_6$ concentrations, while commercial LP30 is shown as a comparison in blue. 40
Fig. 29: Cyclic voltammogramms of the cyclic electrolytes BC (red), HC (orange) and DC (green). Anodic current densities decrease strongly for HC and DC, cathodic current densities only for HC.... 42
Fig. 30: Cyclic voltammogramms for the linear electrolytes DHC (blue) and DOC (purple). Both electrolytes are highly efficient in forming a stable SEI during reduction and oxidation. 42
Fig. 31: First and tenth oxidative and reductive cycle for DHC (left axis) and LP30 (right axis). 43
Fig. 32: GCPL at 0.1 C rates of cells containing graphite electrodes and electrolytes with a 1 mol/L concentration of $LiPF_6$. Crosses mark cathodic capacities, circles anodic capacities. The horizontal line marks the theoretical capacity for graphite. 45
Fig. 33: GCPL at 0.24 C rates of cells containing Sn-C electrodes and varying electrolyte mixtures with 1 mol/L $LiPF_6$. Crosses mark cathodic capacities, rings anodic capacities. The horizontal line marks the theoretical capacity for the Sn/C composite. 45
Fig. 34: Temperature program for the DSC/TGA-MS measurements with plateau temperatures. The ramping rate is 10 °C/min. 56
Fig. 35: Temperature programs for EIS measurements. Program 1 was used for the first measurements and later replaced with program 2 to generate more data at high temperatures. 57

6.3 List of Tables

Table 1: Summary of all assigned vibrations for Li_2CO_3, lithium and sodium carbonates. 23
Table 2: Detected masses and relative abundance in Methyl-, Ethyl-, Propyl- and Butylcarbonates and presumed formula of the ions. Ions marked with a minus were not detected, wave, plus and two pluses mark increasing relative abundance. 25
Table 3: Crystallite sizes, calculated and measured bilayer diameters. 32
Table 4: Comparison of oxidative and reductive stabilities at the highest salt concentration investigated. 41
Table 5: Irreversible capacities in the first cycle for Sn/C electrodes and EC/DMC 1/1 (v/v) and HC/PC 4/1 (v/v) electrolytes with 1 mol/L $LiPF_6$, respectively. 46
Table 6: Equivalents employed and yields achieved for the synthesis of lithium and sodium alkyl carbonates. 49

6.4 Abbreviations

BuLi	*n*-Buthyllithium
CAM	cerium ammonium molybdate
$CDCl_3$	deuterated chloroform
CH	cyclohexane
CV	cyclic voltammetry
D_2O	deuterated water
DCM	dichloromethane
DEC	diethyl carbonate
dH_2O	distilled water
DFT	density functional theory
DMC	dimethyl carbonate
DSC	differential scanning calorimetry
EA	ethyl acetate
EC	ethylene carbonate
EIS	electrochemical impedance spectroscopy
EMC	ethyl methyl carbonate
FEC	fluorethylene carbonate
FTIR	Fourier transform infrared spectroscopy
FWHM	full width at half maximum
GCPL	galvanostatic cycling with potential limitation
HOMO	highest occupied molecular orbital
LEDC	lithium ethylene dicarbonate
LCO	lithium cobalt oxide
LCP	lithium cobalt phosphate
LFP	lithium iron phosphate
LMNO	lithium manganese nickel oxide
LMO	lithium manganese oxide
LUMO	lowest unoccupied molecular orbital
MeCN	acetonitrile
NMC	lithium nickel manganese cobalt oxide
NMP	*N*-methylpyrollidone
NMR	nuclear magnetic resonance
OCV	open current voltage
PC	propylene carbonate
PXRD	powder X-ray diffraction
RBF	round bottomed flask
RT	room temperature
SAXS	small angle X-ray scattering
SEI	solid electrolyte interface
TGA-MS	thermogravimetric analysis with mass spectrometry
TLC	thin layer chromatography
VC	vinylene carbonate